

University of Windsor

Scholarship at UWindor

Electronic Theses and Dissertations

Theses, Dissertations, and Major Papers

1-1-2019

A Miniaturized Chemical Vapor Detector Using MEMS Flexible Platform

Haleh Nazemi
University of Windsor

Follow this and additional works at: <https://scholar.uwindsor.ca/etd>

Recommended Citation

Nazemi, Haleh, "A Miniaturized Chemical Vapor Detector Using MEMS Flexible Platform" (2019).
Electronic Theses and Dissertations. 8174.
<https://scholar.uwindsor.ca/etd/8174>

This online database contains the full-text of PhD dissertations and Masters' theses of University of Windsor students from 1954 forward. These documents are made available for personal study and research purposes only, in accordance with the Canadian Copyright Act and the Creative Commons license—CC BY-NC-ND (Attribution, Non-Commercial, No Derivative Works). Under this license, works must always be attributed to the copyright holder (original author), cannot be used for any commercial purposes, and may not be altered. Any other use would require the permission of the copyright holder. Students may inquire about withdrawing their dissertation and/or thesis from this database. For additional inquiries, please contact the repository administrator via email (scholarship@uwindsor.ca) or by telephone at 519-253-3000ext. 3208.

A Miniaturized Chemical Vapor Detector Using MEMS Flexible Platform

by

Haleh Nazemi

A Thesis

Submitted to the Faculty of Graduate Studies
through the Department of Electrical and Computer Engineering
in Partial Fulfillment of the Requirements for
the Degree of Master of Applied Science
at the University of Windsor

Windsor, Ontario, Canada

2019

© 2019 **Haleh Nazemi**

A Miniaturized Chemical Vapor Detector Using MEMS Flexible Platform

by

Haleh Nazemi

APPROVED BY:

R. Riahi

Department of Mechanical, Automotive and Materials Engineering

M. Azzouz

Department of Electrical and Computer Engineering

A. Emadi, Advisor

Department of Electrical and Computer Engineering

November 28, 2019

Declaration of Co-Authorship / Previous Publication

I hereby declare that this thesis incorporates material that is result of joint research, as follows:

This thesis includes outcome of publications which also have co-authors who are/were students or post-doctoral fellows supervised by Dr. Arezoo Emadi. The co-authors are Dr. Jaewoo Park, Aashish Joseph, Jay Nagarajan, Jenitha Antony Balasingam, Siddharth Swaminathan and Tara Ahmadi. In all cases, only primary contributions of the author towards these publications are included in this thesis.

Chapter 2 of this thesis includes a paper published in Journal of Sensors. The paper was co-authored with Aashish Joseph, Dr.Jaewoo Park and Dr.Arezoo Emadi.

Chapter 3 of this thesis includes a paper submitted to Journal of Sensors for publication. The paper was co-authored with Jay Nagarajan, Jenitha Antony Balasingam, Siddharth Swaminathan, Tara Ahmadi and Dr.Arezoo Emadi.

Chapters 4 and 5 of this thesis include a paper presented in IEEE Sensors 2019 Conference. The paper was co-authored with Dr.Arezoo Emadi.

I am aware of the University of Windsor Senate Policy on Authorship and I certify that I have properly acknowledged the contribution of other researchers to my thesis, and have obtained written permission from each of the co-authors to include the above materials in my thesis.

I certify that, with the above qualification, this thesis, and the research to which it refers, is the product of my own work.

This thesis includes 3 original papers that have been previously published/submitted for publication in peer reviewed journals, as follows:

Thesis Chapter	Publication Title	Publication Status
Chapter 2	H. Nazemi , A. Joseph, J. Park and A. Emadi, "Advanced Micro-and Nano-Gas Sensor Technology:A review" <i>Sensors, 2019</i>	Published
Chapter 3	J. Nagarajan, H. Nazemi , J. Antony Balasingam, S.Swaminathan, T. Ahmadi and A. Emadi, "Mass Sensors Based on Capacitive and Piezoelectric Micromachined Ultrasonic Transducers-CMUT and PMUT" <i>Sensors, 2019</i>	Submitted
Chapter 4 & 5	H. Nazemi and A. Emadi, "A New Advanced Analytical Model for Bi-Layer Circular CMUT-Based Gas Sensor" <i>IEEE Sensors, 2019</i>	Published

I certify that I have obtained a written permission from the copyright owners to include the above published materials in my thesis. I certify that the above materials describe work completed during my registration as a graduate student at the University of Windsor.

I declare that, to the best of my knowledge, my thesis does not infringe upon anyone's copyright nor violate any proprietary rights and that any ideas, techniques, quotations, or any other material from the work of other people included in my thesis, published or otherwise, are fully acknowledged in accordance with the standard referencing practices. Furthermore, to the extent that I have included copyrighted material that surpasses the bounds of fair dealing within the meaning of the Canada Copyright Act, I certify that I have obtained a written permission from the copyright owners to include such materials in my thesis.

I declare that this is a true copy of my thesis, including any final revisions, as approved by my thesis committee and the Graduate Studies office, and that this thesis has not been submitted for a higher degree to any other University or Institution.

Abstract

According to the Canadian Cancer Society, lung cancer is the one of the leading causes of cancer death. It has been shown that cancer survival chance depends on factors including the availability of early detection and diagnostic tools such as miniaturized and sensitive gas sensor. This can detect the released volatiles in addition to be implementable in portable electronics, which decisively improves the patient's survival rate. Therefore, in this thesis and in an effort to develop high-sensitive and miniaturized gas sensor, a microelectromechanical systems (MEMS) platform is utilized. In this work, a sensitive gas sensor is proposed by employing capacitive micromachined ultrasonic transducer (CMUT) configuration due to its high sensitivity, low LOD and reversibility. The comprehensive analytical model is proposed for this circular bilayer CMUT-based gas sensor for the first time, which includes all the known critical design parameters of the sensor. The model also includes effects of membrane softening and residual stress of the top membrane and the sensing component. The model is further followed by conducting FEA simulations, to investigate effect of critical parameters on center resonant frequency of the device. The achieved results for FEA simulations are compared with the proposed model, which shows less than 5% average variation. Both model and simulations verify that maximum sensitivity occurs at smaller radius, thinner membrane and structural material with lower density. The simulations results are utilized to maximize the sensitivity of the gas sensor in a sample frequency range of 5MHz and 25MHz. The proposed device has a 500nm functionalized polysilicon membrane with 300nm polyisobutylene (PIB) while the cavity height is 500nm and 30V DC bias voltage is applied. The proposed and designed CMUT-based gas sensor offers a 222Hz/zg sensitivity ($\Delta f/\Delta m$) in the aforementioned frequency range.

Acknowledgments

First, I would like to express my sincere appreciation to my adviser, Dr. Arezoo Emadi, for her continuous support and motivation during my research and study. I am thankful to Dr. Emadi for her encouragement of my research also in motivating and mentoring me to take on leadership roles.

Furthermore, I wish to thank my committee members, Dr. Riahi and Dr. Azzouz for taking the time to review my thesis and provide me with constructive feedback.

In addition, I would like to express my deepest appreciation to my spouse and my best friend, for his support, understanding and encouragement over the past few years. I am thankful to him for each of those moments when he kindly and patiently sat and listened.

Last but not least, I also would like to express my deep gratitude to my parents for their unconditional love and support from thousands of miles away.

Table of Contents

Declaration of Co-Authorship / Previous Publication	iii
Abstract.	v
Acknowledgments	vi
List of Tables.	xi
List of Figures	xix
List of Acronyms	xx
List of Symbols.	xxii
Chapter 1 Introduction.	1
1.1 Contributions	3
1.2 Thesis Outline.	4
Chapter 2 Micromachined Gas and Volatile Sensors	6
2.1 Introduction.	6
2.2 Surface Acoustic Wave (SAW) Gas Sensor	7
2.2.1 SAW Structure and Mechanism of Operation	7
2.2.2 Structural Materials and Fabrication Process	8
2.2.3 Conventional Sensing Materials and SAW Applications	9
2.3 Metal Oxide Semiconductor (MOS) Gas Sensors	9
2.3.1 MOS Structure and Mechanism of Operation	9
2.3.2 Structural Materials and Fabrication Process	11
2.3.3 Conventional Sensing Materials and MOS Applications	11
2.4 Quartz Crystal Microbalance (QCM) Gas Sensors.	12
2.4.1 QCM Structure and Mechanism of Operation	12

2.4.2	Structural Materials and Fabrication Process	13
2.4.3	Conventional Sensing Materials and QCM Applications.	13
2.5	Electrochemical Gas Sensors	14
2.5.1	Electrochemical Sensor Structure and Mechanism of Operation. . .	14
2.5.2	Structural Materials and Fabrication Process	15
2.5.3	Conventional Sensing Materials and Electrochemical Applications .	15
2.6	Piezoelectric Micromachined Ultrasonic Transducer(PMUT)-Based Gas Sensors	16
2.6.1	PMUT Structure and Mechanism of Operation	16
2.6.2	Structural Materials and Fabrication Process	17
2.6.3	Conventional Sensing Materials and PMUT-Based Gas Sensors Application	18
2.7	Capacitive Micromachined Ultrasonic Transducer(CMUT)-Based Gas Sensors	18
2.7.1	CMUT Structure and Mechanism of Operation	18
2.7.2	Structural Materials and Fabrication Process	20
2.7.3	Conventional Sensing Materials and CMUT-Based Gas Sensors Applications	21
2.8	Conclusions.	21
 Chapter 3 Capacitive Micromachined Ultrasonic Transducer (CMUT)-Based Gas Sensors		
3.1	Introduction.	24
3.2	CMUT and M ³ CMUT-Based Gas Sensor Principle of Operation	25
3.3	Conventional CMUT Sensor Microfabrication Techniques	29
3.3.1	Sacrificial Technique	29

3.3.2	Wafer Bonding Techniques	30
3.3.2.1	Wafer Fusion Bonding	30
3.3.2.2	Local Oxidation of Silicon (LOCOS).	32
3.3.2.3	Anodic Wafer Bonding	33
3.3.3	Flexible CMUT Structures	34
3.4	Conclusions.	35
Chapter 4	Developed Bilayer CMUT-Based Gas Sensor Model with Circular Membrane.	36
4.1	Introduction.	36
4.2	Proposed Analytical Model for Conventional CMUT Structure	37
4.3	Proposed Analytical Models for CMUT-Based Gas Sensor	42
4.4	Equivalent Circuit Model of a Conventional CMUT	48
4.5	Proposed Equivalent Circuit Model of a Bilayer CMUT-Based Gas Sensor	49
4.6	Conclusions.	51
Chapter 5	Proposed Micromachined CMUT-Based Gas Sensors - Design, Simulations, and Evaluations	52
5.1	Introduction.	52
5.2	COMSOL Multiphysics and System Setup	53
5.2.1	Domain Meshing	53
5.2.2	Boundary Conditions for FEA Simulations	55
5.2.3	Proposed Structural Materials in FEA Simulations	58
5.3	Sensor Performance Evaluations and Simulation Results of Bilayer Circular CMUT-Based Sensors	59
5.3.1	Effect of the Radius	59
5.3.2	Effect of the Membrane Thickness	63

5.3.3	Effect of the Cavity Height	67
5.3.4	Effect of the Structural Material	70
5.3.5	Influence of the Sensing Material Properties	75
5.3.5.1	Investigation on Sensing Material Mass Change	75
5.3.5.2	Investigation on Sensing Material Thickness Change	79
5.4	Comparison Between the Proposed Analytical Model and Conducted FEA Simulations	83
5.5	Sensitivity Evaluation	88
5.6	Conclusions.	92
Chapter 6 Proposed Fabrication Steps for the CMUT-Based Gas Sensor		
with Enhanced Sensitivity 94		
6.1	Introduction.	94
6.2	Wafer Fusion Bonding Fabrication Steps for CMUT-Based Gas Sensor	96
6.3	Conclusions.	101
Chapter 7 Conclusions and Future Work 102		
7.1	Conclusions	103
7.2	Future Works	104
References. 119		
Appendices 120		
Vita Auctoris. 121		

List of Tables

4.1	Design parameters in the developed and proposed models.	44
5.1	Number of elements for a bilayer circular CMUT-based gas sensor with $9\mu m$ radius and $500nm$ silicon membrane which is functionalized by $100nm$ PIB while the cavity is $140nm$	54
5.2	Material properties of Silicon, Polysilicon, Silicon Nitride and PIB.	58
5.3	Structural properties of the simulated devices to evaluate the effect of radius.	60
5.4	Structural properties of the simulated devices to evaluate effect of membrane thickness.	64
5.5	Structural properties of the simulated devices to evaluate the effect of cavity height.. . . .	67
5.6	Structural properties of the simulated devices to evaluate the effect of material properties.	71
5.7	Structural properties of the simulated devices to evaluate the sensing material mass change.	76
5.8	Structural properties of the simulated devices to evaluate sensing material thickness change.	80
6.1	Physical properties of the proposed CMUT for fabrication. Radius of the structure is $9\mu m$	96

List of Figures

2.1	Schematic view of a SAW gas sensor.	7
2.2	Schematic view of an MOS sensor and the microheater.	10
2.3	Schematic view of a QCM gas sensor.	12
2.4	Schematic view of an electrochemical sensor.	14
2.5	Schematic view of a PMUT-based gas sensor.	16
2.6	Schematic view of a CMUT-based gas sensor with deflected top membrane.	18
3.1	Schematic view of a CMUT cell configuration.	25
3.2	Schematic view of a CMUT with deflected top membrane.	27
3.3	Schematic view of an <i>M3</i> -CMUT.	27
3.4	Schematic view of a CMUT-based gas sensor.	28
3.5	Schematic view of CMUT fabrication steps using sacrificial release process.	30
3.6	Schematic view of CMUT fabrication steps using wafer fusion bonding technique.	31
3.7	Schematic view of LOCOS fabrication steps.	32
3.8	Schematic view of anodic bonding fabrication steps.	33
3.9	Schematic view of a flexible CMUT.	34
3.10	Schematic view of a flexible silicon substrate.	34
4.1	Schematic view of a CMUT mass-spring-damper model.	38
4.2	Schematic view of a mass-spring-damper for a bilayer CMUT-based gas sensor.	42
4.3	Schematic view of the CMUT structure and the target point at y	45
4.4	Basic view of the Mason's equivalent circuit.	48

4.5	Equivalent circuit model of a conventional CMUT cell.	49
4.6	The developed equivalent circuit model for a CMUT-based gas sensor.	50
5.1	Portion of the meshed CMUT-based gas sensor.	54
5.2	Frequency dependency associated with number of elements.	55
5.3	Schematic view of the designed device in COMSOL Multiphysics.	56
5.4	(a) Fixed constraints includes bottom membrane and perimeter of the top membrane and sensing layer, (b) free boundaries, which consists of the top and bottom surfaces of the top membrane and the sensing layer.. . . .	56
5.5	Vacuum cavity (the highlighted domain in blue) is defined as the deforming domain.	56
5.6	(a)The top surface (highlighted in blue) of the top membrane is defined as the terminal to apply DC bias voltage. (b) the bottom electrode is grounded.	57
5.7	Schematic view of a CMUT-based gas sensor when damping is considered. . .	58
5.8	Conducted FEA simulations for (a) first, (b) second, (c) third, (d) forth, (e) fifth and (f) six modes of the resonant frequency of bilayer circular CMUT-based gas sensor with $5\mu m$ radius and $500nm$ polysilicon membrane, which is functionalized by $300nm$ PIB while biased with $30V$ DC and the cavity is defined $500nm$	61
5.9	(a) Resonant frequency (MHz) vs radius (μm), and (b) frequency shift(MHz) vs. radius (μm) based on the resonant frequency of the device with radius $5\mu m$, for a $500nm$ polysilicon membrane, which is functionalized by $300nm$ PIB, while biased by $30V$ DC and the cavity is defined $500nm$	61
5.10	Membrane displacement (nm) vs. membrane radius (μm) for a $500nm$ polysilicon membrane, which is functionalized by $300nm$ PIB, while biased by $30V$ DC and the cavity is defined $500nm$	62

5.11	Membrane displacement profile for the radius $5\mu m$, $500nm$ polysilicon membrane, which is functionalized by $300nm$ PIB, while biased by $30V$ DC and the cavity is defined $500nm$	62
5.12	Total displacement of the membrane for a $5\mu m$ radius, $500nm$ polysilicon membrane, which is functionalized by $300nm$ PIB, while biased by $30V$ DC and the cavity is defined $500nm$	63
5.13	FEA simulations for the first six modes of frequency of a circular bilayer CMUT-based gas sensor, with $300nm$ polysilicon membrane functionalized by $200nm$ PIB, radius $9\mu m$, cavity $150nm$ while biased with 46 DC voltage.	64
5.14	(a) Resonant frequency (MHz) vs. membrane thickness (nm) and (b) frequency shift (MHz) vs. membrane thickness (nm) where the reference resonant frequency belongs to a device with $300nm$ membrane thickness. Simulations are conducted for polysilicon membranes with $9\mu m$ radius, which are functionalized by $200nm$ PIB, while biased by 46 DC voltage and the cavity is defined $150nm$	65
5.15	Displacement (nm) vs. membrane thickness (nm) for a polysilicon membrane with $9\mu m$ radius, which is functionalized by $200nm$ PIB, while biased by 46 DC voltage and the cavity is defined $150nm$	66
5.16	profile of the deflected polysilicon membrane for a structure with $9\mu m$ radius, which is functionalized by $200nm$ PIB, while biased by 46 DC voltage and the cavity is defined $150nm$	66
5.17	Total displacement of the bilayer circular CMUT-based gas sensor with $9\mu m$ radius, which is functionalized by $200nm$ PIB, while biased by 46 DC voltage and the cavity is defined $150nm$	66
5.18	The first six frequency modes of conducted FEA simulations for a circular CMUT-based gas sensor, with $500nm$ polysilicon membrane functionalized by $100nm$ PIB, cavity height $130nm$ and radius $9\mu m$, while biased with $30V$ DC.	68

5.19	(a) Resonant frequency (<i>MHz</i>) vs. cavity height (<i>nm</i>) and (b) frequency shift (<i>MHz</i>) vs. cavity height (<i>nm</i>) when the reference resonant frequency belongs to the device with 130 <i>nm</i> cavity height. FEA simulations are conducted for 500 <i>nm</i> polysilicon membranes with 9 <i>μm</i> radius, which are functionalized by 100 <i>nm</i> PIB, while biased by 30 DC voltage.	68
5.20	Displacement(<i>nm</i>) vs. cavity height(<i>nm</i>) for a 500 <i>nm</i> polysilicon membrane with 9 <i>μm</i> radius, which is functionalized by 100 <i>nm</i> PIB, while biased by 30 DC voltage.	69
5.21	Membrane displacement profile for a 500 <i>nm</i> polysilicon membrane with 9 <i>μm</i> radius, which is functionalized by 100 <i>nm</i> PIB, while biased by 30V DC and the cavity height is defined 130 <i>nm</i>	70
5.22	Total displacement of the device with 500 <i>nm</i> polysilicon membrane with 9 <i>μm</i> radius, which is functionalized by 100 <i>nm</i> PIB, while biased by 30V DC and the cavity height is defined 130 <i>nm</i>	70
5.23	FEA simulations for (a) first, (b) second, (c) third, (d) forth, (e) fifth and (f) sixth modes for a circular CMUT-based gas sensor, with 500 <i>nm</i> silicon membrane functionalized by 200 <i>nm</i> PIB, radius 9 <i>μm</i> and 140 <i>nm</i> cavity height while biased with 46 DC voltage.	72
5.24	(a) Resonant frequency (<i>MHz</i>) vs. material and (b) frequency shift (<i>MHz</i>) vs. material where polysilicon is considered as the reference material for the frequency shift. FEA simulations are conducted for 500 <i>nm</i> membranes, functionalized by 200 <i>nm</i> PIB, 9 <i>μm</i> radius and 140 <i>nm</i> cavity height, while biased with 46V DC.	73
5.25	Displacement (<i>nm</i>) vs. material for a 500 <i>nm</i> silicon membrane with 9 <i>μm</i> radius, which is functionalized by 200 <i>nm</i> PIB and 140 <i>nm</i> cavity height while biased by 46V DC.	73

5.26 Displacement (<i>nm</i>) vs. material for a 500 <i>nm</i> silicon membrane with 9 <i>μm</i> radius, which is functionalized by 200 <i>nm</i> PIB and 140 <i>nm</i> cavity height while biased by 46V DC.	74
5.27 Total displacement for a bilayer circular CMUT-based gas sensor with 500 <i>nm</i> functionalized silicon membrane with 200 <i>nm</i> PIB, when the cavity is 140 <i>nm</i> and 46V is applied as the bias voltage.. . . .	74
5.28 (a) First, (b) second, (c) third, (d) fourth, (e) fifth and (f) sixth modes of frequency for a bilayer circular CMUT-based gas sensor with 9 <i>μm</i> radius, 500 <i>nm</i> silicon membrane, which is functionalized by 50 <i>nm</i> PIB, while cavity height is 140 <i>nm</i> and biased with 46V DC.	76
5.29 Frequency (<i>MHz</i>) vs. sensing material density(<i>Kg/m³</i>) (a) and frequency shift (<i>MHz</i>) (b) vs. sensing material density(<i>Kg/m³</i>) when the reference frequency belongs to sensing material with original density (920 <i>Kg/m³</i>). FEA simulations are conducted for bilayer circular CMUT-based gas sensors with 9 <i>μm</i> radius, 500 <i>nm</i> thickness of the silicon and polysilicon membranes, coated by 50 <i>nm</i> and 100 <i>nm</i> PIB, 140 <i>nm</i> cavity height while biased with 46V DC.	77
5.30 Displacement of the 500 <i>nm</i> silicon and polysilicon membranes, which are functionalized by 50 <i>nm</i> and 100 <i>nm</i> while the cavity height id 140 <i>nm</i> and the membrane is biased with 46V DC.	78
5.31 The displacement profile of 500 <i>nm</i> silicon membrane for a simulated circular CMUT-based gas sensor with 9 <i>μm</i> radius, 140 <i>nm</i> cavity height while biased with 46V DC.. . . .	79
5.32 Total displacement of 500 <i>nm</i> silicon membrane for a simulated circular CMUT-based gas sensor with 9 <i>μm</i> radius, 140 <i>nm</i> cavity height, biased with 46V DC. . . .	79

5.33	(a) first, (b) second, (c) third, (d) forth, (e) fifth and (f) sixth modes of frequency, simulated in COMSOL for a 500nm silicon membrane with radius 9μm and cavity height 140nm. The membrane is functionalized by 100nm PIB while 46V DC is applied.	80
5.34	Frequency (MHz) vs. sensing material thickness(nm), (a) and frequency shift (MHz) (b) vs. sensing material thickness(nm) where the structure with 120nm is considered for the reference frequency. FEA simulations are conducted in COMSOL for 500nm silicon and polysilicon membranes with radius 9μm and cavity height 140nm. The membrane is functionalized by 100nm PIB while 46V DC is applied.. . . .	81
5.35	Displacement (nm) vs. sensing material thickness, simulated in COMSOL for a 500nm silicon and polysilicon membranes with radius 9μm and cavity height 140nm. The membrane is functionalized by 100nm PIB while 46V DC is applied.. . . .	82
5.36	The displacement profile of a 500nm silicon membrane with radius 9μm and cavity height 140nm. The membrane is functionalized by 100nm PIB while 46V DC is applied.	82
5.37	Total displacement of a 500nm silicon membrane with radius 9μm and cavity height 140nm. The membrane is functionalized by 100nm PIB while 46V DC is applied.	83
5.38	Resonant frequency vs. membrane radius for a structure with 500nm polysilicon top membrane and cavity height, which is functionalized by 300nm PIB while 30V DC is applied.. . . .	84
5.39	Resonant frequency vs. membrane thickness for a structure with 9μm radius, polysilicon membrane and 200nm PIB thickness as well as 150nm cavity height, which is excited by 46V as the applied DC bias voltage.	85
5.40	Resonant frequency vs. cavity height for a structure with 9μm radius, 500nm thickness polysilicon membrane and 30V applied DC voltage.	86

5.41	Resonant frequency vs. material for a structure with $9\mu m$ radius, $500nm$ top membrane thickness and $200nm$ PIB thickness as well as $140nm$ cavity height, which is excited by $30V$ as the applied DC bias voltage..	86
5.42	Resonant frequency prediction vs. sensing material mass for a structure with $9\mu m$ radius, $500nm$ polysilicon membrane, $140nm$ cavity height, which is functionalized by $100nm$ PIB and $30V$ as the applied DC bias voltage..	87
5.43	Resonant frequency prediction vs. sensing material thickness for a structure with $9\mu m$ radius, $500nm$ silicon membrane, $140nm$ cavity height, which is functionalized by PIB and biased with $46V$ DC.	87
5.44	Sensitivity (Hz/zg) vs. membrane radius(μm) for a $500nm$ polysilicon membrane, which is functionalized by $300nm$ PIB while biased by $30V$ DC and the cavity is defined $500nm$	89
5.45	Sensitivity (Hz/zg) vs. membrane thickness (nm) for a polysilicon membrane with $9\mu m$ radius, which is functionalized by $200nm$ PIB, while biased by 46 DC voltage and the cavity is defined $150nm$	89
5.46	Sensitivity (Hz/zg) vs. material for a $500nm$ membrane, functionalized by $200nm$ PIB, $9\mu m$ radius and $140nm$ cavity height, while biased with $46V$ DC.	90
5.47	Sensitivity(Hz/zg) vs. sensing material density(Kg/m^3) for a bilayer circular CMUT-based gas sensor with $9\mu m$ radius, $500nm$ thickness of the silicon and polysilicon membranes, which are functionalized by $50nm$ and $100nm$ PIB, with $140nm$ cavity height while biased with $46V$ DC.	91
5.48	Sensitivity (MHz/zg) vs. sensing material thickness, simulated in COMSOL for a $500nm$ silicon and polysilicon membranes with radius $9\mu m$ and cavity height $140nm$. The membrane is functionalized by $100nm$ PIB while $46V$ DC is applied.. . . .	91

6.1 SEM image for a fabricated CMUT using sacrificial technique (POLYMUMPs), chip IMUWR001.	95
6.2 Schematic view of CMUT-based gas sensor fabrication steps using wafer fusion bonding and inkjet dispensing.	101

List of Acronyms

Notation	Description
MEMS	Microelectromechanical systems
CMUT	Capacitive Micromachined Ultrasonic Transducer
SAW	Surface Acoustic Wave
PMUT	Piezoelectric Micromachined Ultrasonic Transducer
VOC	Volatile Organic Compound
PANI-ES	Polyaniline Emeraldine
NDSA	Naphtalene Disulfonic Acids
DBSA	Dodecylbenzene Sulfonic Acid
HCL	Hydrochloric Acid
IDE	Inter Digitated Electrode
MOS	Metal Oxide Semiconductor
PEDOT	Poly Ethylene-Dioxythiophene
PANI	Polyaniline
PPy	Polypyrrole
GO	Graphene Oxide
PIB	Polyisobuyelene
TNT	Trinitrotoluene
SOI	Silicon on Insulator
DMMP	Dimethyl Methylphosphonate
CO_2	Carbon Dioxide
LOD	Limit of Detection

Notation	Description
ZnO_2	Zinc Peroxide
PZT	Lead Zirconate Titanate
$Pb(Zr_3Ti)O_3$	Lead Zirconate Titanate
SnO_2	Stannic Oxide
ZnO	Zinc Oxide
WO_3	Tungsten Trioxide
NiO	Nickel Oxide
TiO_2	Titanium Dioxide
Cr_2O_3	Chromium Oxide
Mn_3O_4	Manganese Oxide
AlN	Aluminum Nitride
DKAP	Polydimethylsiloxane
LOCOS	Local Oxidation of Silicon
BOE	Buffered Oxide Etch
BOX	Buffer Oxide
PolySOI	Polysilicon on Insulator
RIE	Reactive Ion Etching
PECVD	Plasma Enhanced Chemical Vapor Deposition
TMAH	TetraMethyl Ammonium Hydroxide
PET	Polyethylene Terephthalate
DRIE	Deep Reactive ion Etching
PDMS	Polydimethylsiloxane

List of Symbols

Notation	Description
R_{Source}	Source Resistance
C_{Paras}	Parasitic Capacitance
R_{Bm}	Electrical Equivalent for Damping
$-C_{Spring}$	Spring Softening Effect Due to the Applied DC Bias Voltage
C_m	Membrane Capacitor
L_{Medium}	Medium Loaded Mass Electrical Equivalent
V_{AP}	Action Potential
σ_{Stress}	Stress
Δm	Mass Change
Δf	Frequency Shift
C	Material Constant
f_0	Reference Frequency
ρ_s	Surface Mass Density
ρ_q	Quartz Density
μ_q	Shear Stiffness
m	Mass
t_m	Membrane Thickness
r_m	Membrane Radius
ν_m	Membrane Poisson's Ratio
ρ_m	Membrane Density

Notation	Description
E_m	Membrane Young's Modulus
A_m	Membrane Area
h_{eff}	Effective Cavity Height
k	Membrane Stiffness
$V_{Collapse}$	Collapse Voltage
h_0	Initial Cavity Height
x	Displacement
F	Total Force
F_{Spring}	Spring Force
$F_{Capacitor}$	Capacitor Force
C	Capacitance
σ_{totm}	Membrane Total Residual Stress
σ_{thm}	Membrane Thermal Residual Stress
σ_0	Membrane Initial Residual Stress
k_{Bi}	Bilayer Membrane Stiffness
B_m	Damping
D	Flexural Rigidity
D_{eff}	Effective Flexural Rigidity
σ_{0t}	Membrane Initial Residual stress
σ_{ths}	Sensing Layer Thermal Residual stress
m_s	Sensing Layer Mass
t_s	Sensing Layer Thickness
y	Sensing Layer Given Point
T_f	Sensing Layer Solidification Temperature
T_s	Sensing Layer Final Temperature

Notation	Description
α	Thermal Expansion Coefficient
ν_s	Sensing Layer Poisson's Ratio
L_m	Membrane Mass Electrical Equivalent
$C_{Paras-s}$	Parasitic Capacitance between Sensing Layer and Bottom Electrode
$C_{Param-m}$	Parasitic Capacitance between Membrane and Bottom Electrode
N	Number of Elements
ε	Strain
ν	Poisson's Ratio
ε_{trans}	Transverse Strain
ε_{long}	Longitudinal Strains
C_0	Clamped Parallel Plate Capacitance
Si_3N_4	Silicon Nitride
N_2	Nitrogen
E_0	Electric Field
R_m	Membrane Resistance
C_m	Membrane Capacitance
C_s	Sensing Layer Capacitance

Chapter 1: Introduction

Based on Canadian Cancer Statistics, 2017, “Each hour, an estimated nine people are expected to die of cancer in Canada.” Cancer strikes males and females of all ages. Although it has a higher probability to affect Canadians above the age of 50, it is particularly devastating in children as it remains one of the leading causes of disease-related death in children under the age of 15 [1]. According to the Canadian Cancer Society, lung and bronchial cancer are one of the most common types of cancer along with breast, colorectal and prostate cancer. Lung cancer is by far the leading cause of cancer death among both men and women, more than the other three major cancer types combined. In addition, lung cancer mortality is decidedly uneven in different regions in Canada as well as across the globe. The cancer survival chance variations are due to several factors, which noticeably includes the availability of effective early detection and diagnostic tools. Therefore, early detection of lung cancer’s associated biomarkers is critical for patients’ survival. These biomarkers including 2,4-decadien, 1-propanol, benzaldehyde, hexanal and 2-ethylhexonal exist in patient’s breath, which can be detected using robust diagnostic tools [2, 3]. Considering these facts, employing advanced engineering knowledge in gas sensing technology coupling with biomedical science can effectively decrease mortality rate. In addition, equipping with miniaturized sensitive gas sensor to be implemented in portable devices is an advantage in situations with no immediate access to the healthcare providers. This is feasible by employing microelectromechanical systems (MEMS) platform.

MEMS-based gas sensors are gaining attraction in various applications including biomedical field [4], environmental science [5], indoor and outdoor air quality monitoring [6] and automotive industry [7]. These gas sensors can operate based on several detection tech-

niques to sense the target gases and measure their concentration levels. These include resistivity and acoustic measurements, optical properties detection as well as mass detection [8]. Amongst various gas detection technologies, mass sensors are shown as emerging candidates for high sensitivity applications with low concentration levels of the target gas molecules [8]. Furthermore, mass resonant sensors can be employed in detection of a wide range of gases. These sensors provide high sensitivity, low limit of detection (LOD) and selectivity while they have low cost [8–10]. The mass resonant sensors can be fabricated using advanced micro and nano fabrication technologies. Employing the advanced micro-machining techniques enables sensor miniaturization, which is part of the core objective of this research. This in return leads to possibility for sensor integration in portable devices and wearable electronics. Amongst various mass resonant detectors, micromachined sensors utilizing thin flexible plates such as cantilever and membrane structures are shown as potential candidates for high sensitivity gas detection. Therefore, in this research and in an unconventional approach, capacitive micromachined ultrasonic transducer (CMUT) that combines the benefits offered by its flexible thin membrane as well as its sealed cavity configuration has been employed for gas detection applications. Therefore, in this work, capacitive micromachined ultrasonic transducer (CMUT)-based mass sensor is designed and developed as a potential candidate for detection of low concentration levels of volatile organic compounds in a complex environment. The proposed and modeled CMUT-based sensor benefits from advanced micro and nano fabrication technology, enabling device integration in a compact and portable electronic. In a new approach and unlike CMUT conventional application as a transducer that was introduced in 1994 [11], the study proposed in this thesis employs the mass sensitivity properties of such micromachined structure. The proposed mass detector benefits from low limit of detection (LOD), high sensitivity, reversibility, relatively low cost and simple structure [8]. In addition, the proposed and modeled CMUT-based gas sensor can be functionalized by employing various designed

polymers as sensing materials. Therefore, the CMUT structure can be optimized for a designed sensing material for a known target gas by employing the developed and evaluated model in this work to enhance the device sensitivity. This in return, can broaden the application fields of such miniaturized detector system.

1.1 Contributions

In this thesis and in an unconventional approach, CMUT structure is employed as a mass-based gas sensor. The objective of this thesis is to, for the first time, develop a comprehensive analytical model of the CMUT-based gas sensor. The proposed model includes and correlates all the critical design parameters of a bilayer CMUT-based gas sensor with circular geometry. These parameters consist of radius and thickness of the membrane, device material properties, effective cavity height as well as the sensing material thickness and its material properties. In the developed analytical model in this thesis, all the critical design parameters of a circular bilayer CMUT-based gas sensor are considered, in addition to effects of membrane softening parameters and structural material residual stresses. In order to model the sensor, mass-spring-damper model is employed along with the theory of thin plates. The proposed model considers sensing material properties by replacing flexural rigidity of the conventional CMUT transducer structure with effective flexural rigidity in CMUT sensor. In addition, residual stress of the sensing material is included in the model. The proposed comprehensive analytical model provides a platform for future research in this field.

The analytical model in this thesis is further utilized to design a circular bilayer CMUT-based gas sensor. This step is followed by conducting FEA simulations using COMSOL Multiphysics to enhance sensitivity of the device for low gas concentration detection. In this work, effects of geometrical parameters including radius, membrane thickness and cav-

ity height on resonant frequency and frequency shift of the device are investigated to improve sensor's sensitivity. Since mass and thickness of the sensing component can change while it is exposed to the target gas, influences of these two factors on the frequency and frequency shift of the sensor are also evaluated.

Comparison between the achieved results of the conducted FEA multiphysics simulations and the proposed analytical model indicates a good agreement between the obtained results.

Finally, employing the proposed analytical model along with FEA simulations results led this research to propose a device with sufficient sensitivity for low gas concentration detection using MEMS platform. In addition, the candidate fabrication technique for the proposed device is introduced and designed in this thesis.

1.2 Thesis Outline

In Chapter 2, various candidate gas sensors including metal oxide semiconductors (MOS), electrochemical sensors, quartz crystal micro-balance (QCM), surface acoustic waves (SAW), piezoelectric micromachined ultrasonic transducer (PMUT) as well as CMUT sensors are reviewed. Their principles of operation and fabrication techniques are discussed in addition to advantages and disadvantages of each sensor.

Chapter 3 includes a review of CMUT-based gas sensors along with their principles of operation and details of different fabrication techniques. In Chapter 4, the proposed comprehensive analytical model and its development are presented. Employment of mass-spring-damper model as well as the plate theory in modeling a CMUT-based gas sensor are presented. A new equivalent circuit model of a bilayer CMUT-based gas sensor is also provided in this chapter.

Chapter 5 consists of investigation on critical design parameters of a circular bilayer

CMUT-based gas sensor by employing FEA multiphysics simulations. In this Chapter, radius, membrane thickness, cavity height and structural material of the sensor are investigated as well as mass and thickness of sensing component. Their effects on resonant frequency, frequency shift and consequently sensor's sensitivity are analyzed. Furthermore, a sensitive device for low gas concentration detection is proposed. This chapter also includes a comparison between the achieved results employing the proposed analytical model and the conducted FEA simulations. Finally, conclusion and the summary of the conducted research in this thesis are provided in Chapter 6 in addition to the possible future works.

Chapter 2: Micromachined Gas and Volatile Sensors

2.1 Introduction

Gas sensors are employed in a wide range of applications including environmental science, automotive industry, indoor and outdoor air quality monitoring and medical field [12–14].

They operate based on measuring changes in electrical properties such as resistance, voltage or current. In addition, gas sensors can operate as mass resonant sensors where the shift in center resonant frequency of device is measured. In gas sensing technology, there are different parameters that define performance of sensor including selectivity, reversibility, sensitivity and limit of detection (LOD). In addition, benefiting from advanced micro and nano fabrication technology and microelectromechanical systems (MEMS) platform, leads in low power consumption devices. These techniques provide integrability in wearable and wireless electronics.

This chapter introduces and studies common micro-fabricated gas sensors including surface acoustic wave (SAW), metal oxide semiconductor (MOS), quartz crystal microbalance (QCM), electrochemicals, piezoelectric and capacitive micromachined ultrasonic transducer (PMUT and CMUT)-based gas sensors. In this investigation, structures and mechanisms of operation, fabrication techniques and their applications are discussed along with advantages and disadvantages of each sensor.

2.2 Surface Acoustic Wave (SAW) Gas Sensor

2.2.1 SAW Structure and Mechanism of Operation

The first generation of SAW gas sensors was introduced decades ago with an ultra-high resonant frequency of 400MHz [15]. SAW sensors include two SAW reflector arrays on the crystal substrate separated by a cavity where a pair of electrodes is located, as shown in Figure 2.1. The reflector arrays consist of metal strips with a half-wavelength width. A part of the wave's energy reflects on the spacing between the strips where it gives an almost a full reflection. The reported operating frequencies for the SAW sensors with GaAs substrate are as high as 100–500MHz, which results in complexities in the sensor design and fabrication [16].

SAW sensors can be electrically excited and detected in a piezoelectric substrate using a transducer. In this configuration, and unlike bulk quartz resonators, the frequency of SAW sensors does not depend on the wafer thickness. The operating frequency in such resonators is calculated based on the transducer periodicity, $f = n/l$, where n and l are the propagation velocity and acoustic wavelength, respectively at the transducer center frequency. By changing the surface mass when exposed to the analytes, the propagation speed changes, which causes a frequency shift from the operating frequency. The frequency is

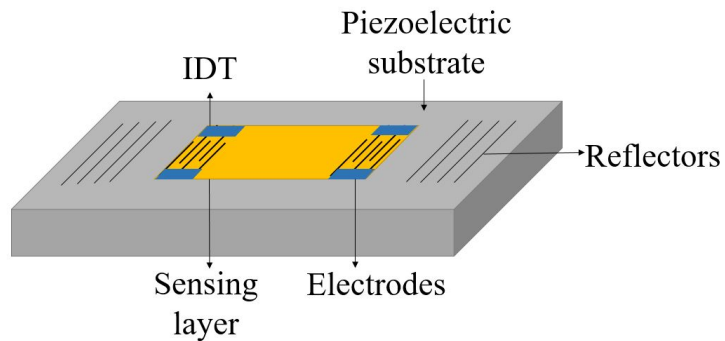


Figure 2.1: Schematic view of a SAW gas sensor.

closely related to the sensor response which can be affected by other factors such as change in viscoelasticity and electrical conductivity due to the absorbed analytes [16].

These sensors detect environmental changes based on the change in the physical properties of the surface waves and amplitude. The measured concentration of detected analytes has been reported to be in picogram scale. In general, high sensitivity, short response time and reversibility are reported as advantages of SAW gas sensors beside being applicable in wireless technologies.

2.2.2 Structural Materials and Fabrication Process

In order to fabricate SAW gas sensors, micromachining techniques are employed [17]. E-beam lithography and lift-off processes are commonly used techniques to fabricate SAW gas sensor on gallium orthophosphate ($GaPO_4$) substrate. $GaPO_4$ is one of the preferred piezoelectric materials for substrates due to its high thermal stability and since the device operates at temperatures up to $930^\circ C$. In this high temperature sensor, platinum is used as electrodes because of the high melting temperature. To have a good adhesion, a zirconium or titanium layer are used between the substrate and electrodes [18]. In general, choice of SAW sensing materials, electrodes as well as substrates depends on the target wave propagation properties. The most common materials used as substrate in SAW sensors are $LiNbO_3$, $GaPO_4$, $LiTaO_3$, silicon and quartz which are functionalized by a sensing material such as piezoelectric zinc oxide (ZnO) and aluminum nitride (AlN) [15, 16]. $GaAs$ substrates have also been used without the need for a piezoelectric film while aluminum electrodes and reflectors are widely used due to their acoustic impedance similarity to the common SAW substrates.

2.2.3 Conventional Sensing Materials and SAW Applications

SAW gas sensors can employ various polymers as their sensing elements that can react to different analytes such as biomarkers associated with lung cancer. However, many of these polymers respond to the presence of more than one analyte. The number of chosen sensing materials and their properties are designed according to the type of biomarkers that need to be identified. Pattern recognition and neural network techniques are employed to discriminate various chemical analytes by analyzing signal obtained from these sensors with different sensing material [15]. In addition, palladium has been used as the sensing material on a SAW sensor to detect hydrogen. Absorbing and desorbing hydrogen molecules result in a change in density and electrical conductivity of the sensing material. Copper phthalocyanine (*CuPc*) has also been used in SAW system for hydrogen detection. It has been shown that *CuPc* layer alone is not sensitive enough to hydrogen, which required high operation temperature of more than 70°C. This operating temperature can be lowered by using *CuPc* or *Pd* thin film as sensing layer down to room temperature. In this design, the change in the sensor's output is mainly due to the change in the electrical conductivity rather than the mass change of the sensing layer [19].

2.3 Metal Oxide Semiconductor (MOS) Gas Sensors

2.3.1 MOS Structure and Mechanism of Operation

Technology of MOS sensors emerged when resistance of Cu_2O changed due to water vapor exposure [12]. These sensors consist of functionalized electrodes and a microheater, which are electrically separated, as shown in Figure 2.2. The structure is fabricated on a membrane fabricated employing advanced micro and nano fabrication techniques.

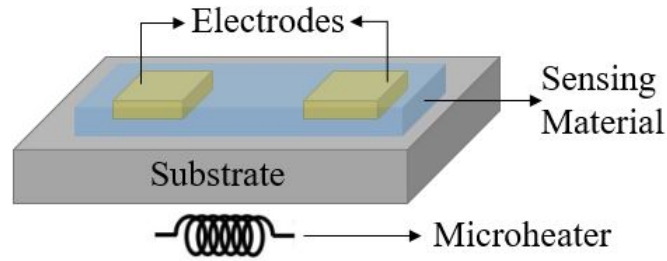


Figure 2.2: Schematic view of an MOS sensor and the microheater.

In these sensors, the substrate is heated up by the microheater to start and expedite oxygen adsorption and sensing procedure [20]. During the sensing process, oxygen is adsorbed, which results in a change in charge carrier density that alters the conductivity of sensing material. This change is measured when change in depletion layer at the grains occurs, which is correlated to the concentration of the target gas [21].

In general, MOS sensors are divided into two categories based on p-type and n-type materials. These groups differently contribute in sensing due to the various interactions with the target gas. In a p-type MOS, positive holes carry the charge and conductivity increases when the number of positive holes is grown due to an oxidizing gas exposure. Whereas, in an n-type MOS sensor, electron carries the charge. Therefore, conductivity decreases when the sensing material is in contact with the target gas and charge depletion happens [22].

These sensors gained attenuation due to their low cost, simple structure and durability. MOS sensors are offered as good candidates for low gas concentration, specially VOCs in less than ppm level [17]. However, they operate using high power due to the high operating temperature ranging between 150°C to 400°C .

2.3.2 Structural Materials and Fabrication Process

In these sensors, SnO_2 , ZnO , WO_3 and TiO_2 are used as the sensing material in n-type MOS sensors while NiO , Cr_2O_3 and Mn_3O_4 -based sensors are used as p-type MOS devices on a silicon substrate [21–24]. In addition, porous materials are employed as the sensing material to enhance sensitivity, selectivity and performance of the device due to existence of pore channels [25].

In order to fabricate an MOS sensor, commonly, the substrate is insulated by a few microns thermally grown SiO_2 . This step is followed by depositing the microheater on the bottom of the device using DC magnetron sputtering. Next, the electrodes are patterned on the SiO_2 layer employing sputtering and lift off techniques, which is further followed by depositing sensing material using magnetron sputtering. The microheater is electrically insulated from the electrodes and the sensing layer by depositing SiO_2 using e-beam evaporation [17, 26]. Nano-casting and self-templating methods are the employed techniques for functionalizing the MOS sensor with porous materials [27].

2.3.3 Conventional Sensing Materials and MOS Applications

These sensors are used to detect benzene, formaldehyde and naphthalene in volatile organic compound (VOC) detection [28]. They are also used in a complex environment with lower sensitivity than laboratories when pattern recognition techniques are employed [28].

In VOC detection, MOS sensors have provided sensitivity in ppb level when high temperature cycle is used. In the temperature cycle, micro heater periodically provides different temperatures to increase reaction between the target VOC and sensing material, which results in an increased sensitivity of device [28, 29].

2.4 Quartz Crystal Microbalance (QCM) Gas Sensors

2.4.1 QCM Structure and Mechanism of Operation

QCM gas sensors consist of two electrodes, which are separated by a piezoelectric material or quartz, as shown in Figure 2.3.

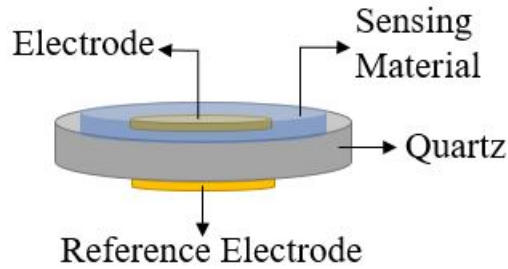


Figure 2.3: Schematic view of a QCM gas sensor.

In the QCM gas sensors, the bottom electrode is known as the reference electrode and top electrode is functionalized by a specific sensing material based on the target gas. When the voltage is applied to the electrode, created electric field across the piezoelectric material causes a deformation in it, which is used to create standing waves by applying AC at the resonant frequency of device [30]. When the sensing material exposes to the target gas, sensor resonant frequency shifts, which is associated with target gas adsorption, as shown in Equation 2.1 [30],

$$\Delta m = -C \cdot \Delta f \quad (2.1)$$

where Δm is surface mass change and C is material dependent constant. Frequency shift of the device is shown in Equation 2.2,

$$\Delta f = \frac{-2f_0 \cdot 2\rho_s}{\sqrt{\mu_q \cdot \rho_q}} \quad (2.2)$$

where f_0 , ρ_s , μ_q and ρ_q are reference frequency, density of surface mass, shear stiffness and quartz's density, respectively. Equation 2.2 is applicable when there is no energy dissipation in the material. Therefore, where damping exists such as a bio-molecular system Equation 2.2 is not valid [31].

Based on Equation 2.2, lower shear stiffness results in higher frequency shift and consequently higher sensitivity in QCM gas sensors. Therefore, thinner quartz crystal, which has lower shear stiffness provides a more sensitive device.

These sensors have sensitivity in ppm level while poor selectivity is reported as their disadvantage [32].

2.4.2 Structural Materials and Fabrication Process

In a typical QCM sensor, a few hundred microns of a piezoelectric material or quartz crystal is used between two electrodes, which are made of gold or platinum by lift-off technique. The quartz crystal is usually etched using anisotropic inductively coupled plasma reactive ion etching (ICP RIE). Arrays of QCM sensors can be fabricated by micromachining techniques and the device is applicable as hybrid sensors when it is combined with oscillator circuit on a silicon substrate [33]. These sensors are commonly functionalized by polymers as sensing material due to their flexibility when deformation occurs in the quartz crystal [31].

2.4.3 Conventional Sensing Materials and QCM Applications

Calixarene or its derivatives are used to functionalize QCM sensors for VOC detections including alcohol, ether, ester and toxic gases. Calixarene is employed to detect methylene chloride emissions in ppm level with robust bonding properties [34]. Ability of calixarene in making hydrogen bonds is made it popular while reacting with target gas. Whereas calixarene can affect sensitivity of QCM due to its random arrangement of molecules in the

crystal [34].

In addition, QCM is used in humidity detection by dip coating polyaniline emeraldine (PANI-ES) thin film. In these sensors, three acids including 1,5-naphtalene disulfonic acids (1,5-NDSA), hydrochloric acid (*HCl*) and dodecylbenzene sulfonic acid (DBSA) are doped on QCM electrode, which operates in 10MHz frequency. These structures provide a sensitivity in ppm level to water vapor by a linear frequency shift, which is correlated to the vapor absorption [34].

Moreover, these sensors are employed in detection of small amount of nitro-explosive gases. In these application, the gold electrode is functionalized by nano-rods or nano-spheres of PPy-BPB with improved sensitivity due to the non-covalent bonds between the halogen and nitro gases [35].

2.5 Electrochemical Gas Sensors

2.5.1 Electrochemical Sensor Structure and Mechanism of Operation

Electrochemical gas sensor's configuration consists of a polymer as a sensing material, which connects two interdigitated electrodes (IDEs) on a silicon substrate, as shown in Figure 2.4.

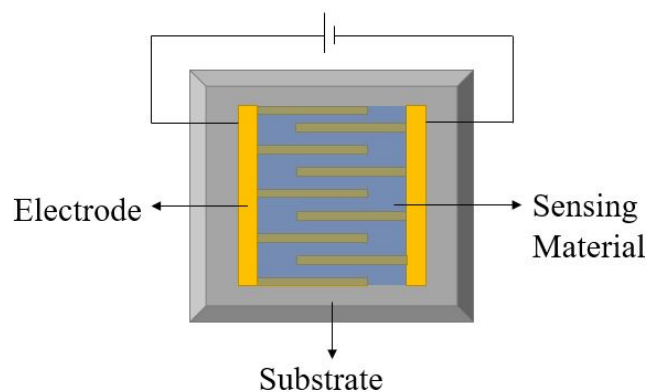


Figure 2.4: Schematic view of an electrochemical sensor.

This structure improves contact between the sensing material and the electrodes while they are connected to an external data analyze unit [36]. These sensors operate based on measuring properties of the sensing material such as electrical resistance or thickness. Change in the properties of the sensing component is due to chemical reaction with the analyte, which can be correlated to the target gas concentration [37]. Unlike MOS sensors, polymer-based electrochemical sensors can operate in the room temperature while they still can measure concentration of VOCs such as benzene and toluene [38]. Moreover, an array of functionalized electrochemical gas sensors with different polymers can be fabricated to increase selectivity.

In general, these sensors benefit from low cost and high sensitivity while baseline drift and poor selectivity are reported as their disadvantages [39,40].

2.5.2 Structural Materials and Fabrication Process

Electrochemical gas sensors consist of an insulated silicon substrate with SiO_2 and two deposited electrodes. The insulator layer is thermally grown or deposited using e-beam evaporation process, which is followed by depositing and patterning the electrodes. Insulating or conductive polymers including poly (3,4-ethylene-dioxythiophene) (PEDOT), polyaniline (PANI) and polypyrrole (PPy) are typically used as the sensing materials [36]. To functionalize the sensor, either spin coating, dip coating, drop casting or spray coating are employed based on the polymer properties [41].

2.5.3 Conventional Sensing Materials and Electrochemical Applications

These sensors are employed in VOC detection using capped nano particles as the sensing material. In addition, breath biomarkers are measured by arrays of functionalized sensors

with gold nano particles. These sensors are employed in lung cancer detection, in ppb level of concentration, when cross-linked gold nano particles are used. Stability, sensitivity and selectivity of these sensors immensely depends on size and composition of the nano particles [42]. In addition, electrochemical sensors with sulfonated doped PPy, is used for 2,4,6-trinitrotoluene (TNT) detection as one of the most explosive materials. These sensors consist of gold IDEs and PPy polymer when there is a sulfonated dye. They have provided the sensitivity in ppb level [41].

2.6 Piezoelectric Micromachined Ultrasonic Transducer (PMUT)-Based Gas Sensors

2.6.1 PMUT Structure and Mechanism of Operation

PMUT structure consists of a clamped edges piezoelectric material which is sandwiched between two electrodes on a silicon substrate. PMUT configuration works based on piezoelectricity effect of materials, which it deforms in response to an applied electrostatic force. This effect can be reversible, which the piezoelectric material creates an electrostatic force when a mechanical force is applied [43]. PMUT configuration recently is employed in gas sensing technology when the device is functionalized by a sensing material depending on a target gas, as shown in Figure 2.5 [44].

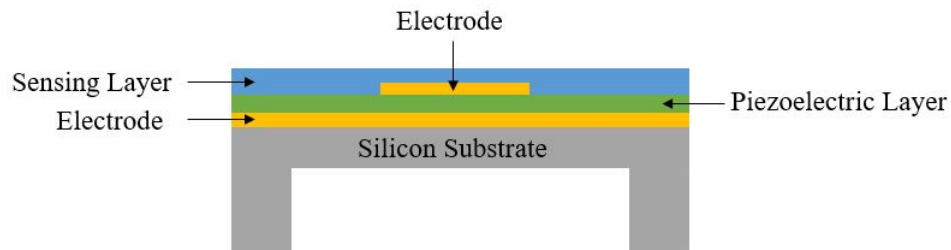


Figure 2.5: Schematic view of a PMUT-based gas sensor.

When the sensing layer adsorbs the target gas molecules, mass of the vibrating piezoelectric material changes, which results in a frequency shift as illustrated in Equation 2.3,

$$\Delta f = -\frac{1}{2}f_0 \cdot \frac{\Delta m}{m} \quad (2.3)$$

where f_0 , m and Δm are the original resonant frequency, mass of the vibrating membrane and mass change due to the gas adsorption, respectively. Frequency shift in a PMUT-based gas sensor can be correlated to the target gas concentration.

Low power consumption, easy integration and selectivity while they are fabricated in arrays are reported as PMUT-based gas sensor advantages [44, 45].

2.6.2 Structural Materials and Fabrication Process

In general, PMUT-based gas sensors are divided into thin and thick films piezoelectric materials. Aluminum nitride (AlN), lead zirconate titanate ($Pb(Zr_3Ti)O_3$), which is named PZT and zinc peroxide (ZnO_2) are commonly used materials for thin film PMUTs [46]. However, a thick piezoelectric material is used when the sensor needs to have a high physical tolerance during exposure. This structure can be fabricated in arrays while functionalized by polymers as sensing materials.

In order to fabricate a PMUT-based gas sensor, sacrificial technique is the conventional employed process. In this technique usually doped silicon is used as the substrate using LPCVD process, while the electrode is e-beam evaporated on it. The channels are wet etched and patterned on the electrode, which is followed by piezoelectric material deposition by sputtering technique and creating the top electrode by e-beam evaporation. Recently, back side or front side etching techniques are used to create a thin piezoelectric layer through the silicon substrate [47–50].

2.6.3 Conventional Sensing Materials and PMUT-Based Gas Sensors Applications

Since PMUT structure is employed in gas sensing technology since 2018, it is only investigated in humidity detection in ppm level, when an array of them is functionalized by graphene oxide (*GO*) using drop casting [44].

2.7 Capacitive Micromachined Ultrasonic Transducer (CMUT)-Based Gas Sensors

2.7.1 CMUT Structure and Mechanism of Operation

CMUTs have been introduced as an alternative to the conventional piezoelectric transducers with improved properties [51]. However, CMUT configuration can also be employed as a mass resonant sensor in the gas sensing field. The structure is functionalized by a sensing material to detect VOCs and various gases, which provide a wide range of application.

CMUT gas sensor consists of a thin flexible membrane coated with a sensing material suspended over a fixed bottom electrode to form a cavity. In this design, the top membrane and the bottom electrode act as a capacitor where changes in the sensing material can influence the device capacitance [8]. A schematic view of a coated CMUT sensor with polyisobutylene (PIB) is shown in Figure 2.6.

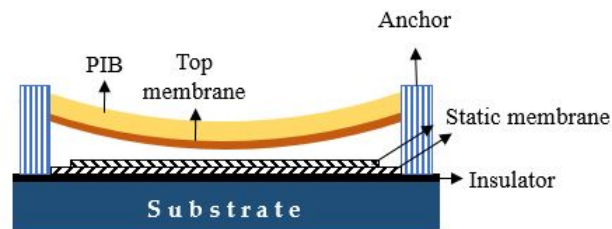


Figure 2.6: Schematic view of a CMUT-based gas sensor with deflected top membrane.

By exposing the polymer to the gas, analytes are adsorbed by the sensing material, which results in a change in the mass of the flexible membrane. This mass change results in a center resonant frequency shift, which is correlated with the analyte concentration. The relation between the center resonant frequency, material properties and structural dimensions are determined by Equation 2.4,

$$f_0 = 0.47 \frac{t_m}{r_m^2} \sqrt{\frac{E_m}{\rho_m(1 - \nu_m^2)}} \quad (2.4)$$

where t_m , r_m , E_m , ρ and ν are the thickness, radius, Young's module, density, and Poisson's ratio of the membrane, respectively [52]. CMUT sensors require a relatively high DC bias voltage known as pull-down voltage to create an electrostatic force across the cavity and bring the top membrane to an optimal point defined by the cavity height and membrane physical properties [51]. In this configuration, several parameters affect the sensitivity of the sensor such as the structural and material properties, radius, membrane thickness, sensing material initial thickness, cavity height, and pull-down voltage. In addition, since the top membrane of a CMUT sensor is backed with vacuum this structure provides a lower energy consumption and higher quality factor [52]. Compared to conventional capacitive gas sensors such as micro-machined cantilever-based sensors, the analytes cannot reach the cavity underneath the vibrating membrane and therefore the sensor resolution is enhanced [53]. Good sensitivity, low LOD, reversibility, and high-quality factor are reported as the advantages of these sensors [52]. CMUT gas sensors has similar disadvantages as electrochemical sensors including poor selectivity and baseline drift associated with the common employed sensing materials. These drawbacks, however, can be addressed through fabricating sensor arrays using different sensing materials.

2.7.2 Structural Materials and Fabrication Process

This device employs stack of polysilicon, silicon or silicon nitride as the membrane and gold electrode, which are fabricated on an insulated silicon substrate with silicon nitride. Polymers are commonly used as sensing materials on the top membrane.

The two common micro-machining methods for CMUT fabrication are sacrificial and wafer bonding techniques [54–56], where the main difference between these two techniques is the method to create the cavity between the two membranes. In sacrificial method, a sacrificial oxide layer is deposited on the fixed bottom electrode which later forms the cavity followed by the deposition of the top membrane material. The sacrificial layer is then etched using wet etching process and through several release holes on the top membrane or designated channels [57].

A more advanced technique to fabricate a CMUT is a wafer bonding method. In this technique, cavities are patterned and created on a handling wafer that bonds to a second wafer with the deposited top membrane material in vacuum and at high temperatures. Second wafer substrate is then etched or polished to leave a thin membrane suspended over the cavity. SOI wafer can also be used as the second wafer, where the top silicon layer acts as the membrane material and oxide as the etching stop when removing the bulk silicon substrate. Wafer bonding method provides several advantages such as elimination of releasing holes that improved device efficiency as well as ability to precisely control and optimize cavity and membrane thicknesses. Moreover, the bonding technique provides capability to fabricate large membranes due to the stress-free processes; however, the quality of bonding is largely affected by the smoothness of the contact surface [58].

2.7.3 Conventional Sensing Materials and CMUT-Based Gas Sensors Applications

These sensors are used in dimethyl methylphosphonate (DMMP) detection by employing a very thin layer of DKAP polymer. DMMP is a simulant for sarin gas, which is detected by these sensors with a good selectivity and a sensitivity of $48.8 \text{ zg/Hz}/\mu\text{m}^2$ [59]. In addition, polyisobutylene (PIB) coated CMUT sensor is also reported to detect DMMP with a sensitivity of $130 \text{ zg/Hz}/\mu\text{m}^2$ [52] with a minimum LOD for DMMP of 16.8 pptv [53].

In addition, CMUT sensors employing different materials such as polyimide, amine-bearing functional groups and quinidine can be fabricated as a highly sensitive CO_2 detector. A CO_2 sensitivity of 1.06 ppm/Hz at 50 MHz and a resolution of 4.9 ppm in the ambient temperature is reported with consideration of other influencing parameters such cross sensitivity with water vapor, sensor repeatability and regeneration [58].

2.8 Conclusions

In this chapter, different micromachined gas sensors have been introduced including SAW, MOS, QCM, electrochemical as well as PMUT and CMUT-based gas sensors. Their structures and mechanisms of operation, standard fabrication techniques employing advanced micro and nanofabrication technology, applications along with their advantages and disadvantages are discussed. SAW gas sensors includes two IDEs and reflector arrays on a piezoelectric substrate, which is coated with sensing material. When target analyte is adsorbed, propagation speed in the sensor changes, which results in a shift in resonant frequency of the device. Short response time, high sensitivity and reversibility are main advantages of SAW sensors while poor selectivity is reported as disadvantage. The sensor's performance can be affected by the environment's temperature.

Electrochemical sensors consist of two electrodes, which are connected by a sensing material. They operate based on change in resistance of the sensing material, which is due to the target gas adsorption. Electrochemical sensors typically benefit from simple structures, low cost, high sensitivity in addition to their capability to be functionalized with different sensing materials while operate in room temperature. However, their performances are influenced by environmental factors including temperature and humidity. MOS sensors, which can be categorized in electrochemical sensors also benefit from long life-time and short response time while they have high energy consumption due to existence of micro heaters.

QCM sensors comprises of two electrodes, which are separated by a quartz component. The electrodes are functionalized by the sensing material depending on target gas. These sensors operate based on measuring frequency shift of the quartz when the sensing material reacted with target analyte. High sensitivity and fast response time are reported as advantages of these sensors while they have poor selectivity and their performances are affected by environment temperature.

PMUT-based gas sensors include a sandwiched piezoelectric material by two electrodes, which is functionalized by a sensing material depending on a target gas. When the target gas is adsorbed, mass of the vibrating membrane changes, which result in a frequency shift. This sensor benefits from Low power consumption, easy integration and selectivity while they are fabricated in arrays.

CMUT-based gas sensors consist of two parallel membranes, which are separated by a vacuum cavity to form a capacitance. The top membrane is functionalized with the sensing material and when the electrostatic force is applied, the membrane deflects towards the bottom electrode and capacitance changes. By exposing the sensing material to the target gas, frequency of the device shifts in response to the target gas adsorption. Based on the conducted review of MEMS-based gas sensors in this chapter and amongst different

detection techniques, CMUT mass resonant sensors configuration are shown as emerging candidate for high sensitive devices. These sensors benefit from relatively simple structure and low cost, high sensitivity and quality factor as well as reversibility and low limit of detection. In order to improve selectivity of a CMUT-based gas sensor, an array of the individual cells can be fabricated and functionalized by a variety of sensing materials. Due to the aforementioned advantages of CMUT-based gas sensors, this structure is reviewed in Chapter 3, in order to propose a comprehensive analytical model and a sensitive device for low gas concentration detections.

Chapter 3: Capacitive Micromachined Ultrasonic Transducer (CMUT)-Based Gas Sensors

3.1 Introduction

Microelectromechanical systems-based sensors (MEMS), are introduced as high-performance detectors due to their sensing capabilities at micro and nanoscale levels and potential for integration with wearable electronics [11]. One of these devices is capacitive micromachined ultrasonic transducers (CMUTs), which were introduced in 1994 [11]. In an unconventional approach, a CMUT structure can also act as a mass resonant sensor, hence allowing it to be used for volatile organic compounds (VOCs) detection applications. These sensors are also used in carbon dioxide [58] and dimethyl methylphosphonate (DMMP) detections [60].

A CMUT-based sensor benefits from a simple parallel plate structure that can be functionalized by a polymer sensing layer that senses the change in the mass when exposed to the target gas molecules. In addition, high quality factor and sensitivity as well as low limit of detection (LOD) are reported as their advantages. CMUT-based gas sensors can be selective in a complex environment when an array of individual devices is functionalized by various sensing materials.

In this chapter, structure and mechanism of operation as well as different fabrication techniques for CMUT-based gas sensors are reviewed.

3.2 CMUT and M³CMUT-Based Gas Sensor Principle of Operation

The structure of a CMUT consists of a deflectable top membrane that is suspended over a fixed bottom electrode to form a cavity between them. The top membrane is clamped at the edges and suspended on top of the bottom electrode. The device top membrane is commonly metalized or is fabricated using a highly conductive material. When a DC bias voltage is applied to the top membrane, it creates an electrostatic force between the bottom electrode and the top membrane that as a result, creates a downward deflection in the top membrane. A schematic view of a conventional CMUT is illustrated in Figure 3.1.

Utilizing advanced microfabrication technology, individual CMUT cells can be fabricated to form an array of sensors with various arrangements including circular, square, O-ring, as well as hexagonal shapes [60–62]. This ability to form an array of sensors on the same chip is beneficial when a CMUT is designed to detect a target gas in a complex environment. Employing an array configuration can address the disadvantages associated with the lack of selectivity for the commonly used polymer as the sensing layers [63]. CMUT structure operates based on electrostatic transduction between the device fixed electrode and the suspended membrane on top of it. The electrostatic force is generated by applying a DC bias voltage to the top membrane, which causes the membrane to deflect toward the

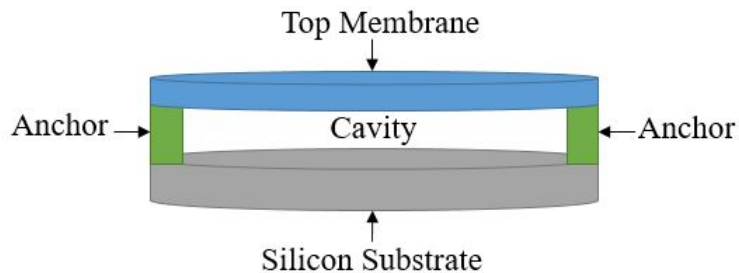


Figure 3.1: Schematic view of a CMUT cell configuration.

bottom electrode. When the electrostatic force creates deflection in the top membrane, a mechanical restoring force resists this deflection due to the membrane stiffness, k , shown in Equation 3.1. If the applied voltage exceeds a limit known as the collapse voltage, presented in Equation 3.2 [64], the mechanical restoring force overcomes the electrostatic force and the device becomes unstable. Therefore, conventional CMUTs are operating close to the collapse voltage of the structure to avoid device breakdown but to enhance the sensor sensitivity [65].

$$k = \frac{16\pi E_m t_m^3}{3(1 - \nu_m^2)r_m^2} - \frac{\epsilon_0 A_m V_{DC}^2}{h_{eff}^3} + 4\pi\sigma_m t_m \quad (3.1)$$

In Equation 3.1, E_m , t_m , r_m , ν_m , A_m , σ_m , V and h_{eff} are Young's modulus, thickness, radius, Poisson's ratio, area, residual stress of the membrane, applied DC voltage and effective cavity of the device, respectively. In Equation 3.1, first term is defined by membrane geometry and its material properties while second and third terms are known as the spring softening effect due to the applied DC bias voltage and residual stress of the membrane, respectively.

$$V_{Collapse} = \sqrt{\frac{8kh_0^3}{27\epsilon_0 A_m}} \quad (3.2)$$

In Equation 3.2, h_0 , ϵ_0 and A_m are cavity height, permittivity of vacuum and membrane area, respectively. By employing the spring softening constant in Equation 3.3, the center resonant frequency of the device is approximated [66],

$$\omega_r = 2\pi f_r = \sqrt{k/m_m} \quad (3.3)$$

where m_m is the effective mass of the membrane. In a CMUT configuration, a DC bias voltage is applied to the top membrane, which creates an electrostatic force across the cavity. The applied force forms a deflection in the membrane towards bottom electrode as

shown in Figure 3.2 [67]. The cavity also acts as a dynamic capacitance in response to changes in the surrounding environment properties of the device including pressure, mass and acoustic signals [62, 68, 69]. The changes alter the membrane deflection, capacitance and consequently the resonant frequency of the device [70]. In order to measure the resonant frequency, device is connected to an impedance analyzer as shown in Figure 3.2.

CMUT can also be developed with a multiple moving membrane capacitive micromachined ultrasonic transducer (M^3 -CMUT) configuration [66] with a potential in gas sensing technology. This new configuration benefits from two or more deflectable membranes that contributes to the device performance as shown in Figure 3.3.

In this design, when a DC bias voltage is applied to top or middle membranes, they are attracted towards each other, therefore, a smaller cavity height can be achieved at a lower DC bias voltage. This results in the enhanced operational properties, acoustic output and sensitivity of the transducer [71]. In general, CMUT sensor is modeled using a mass-spring-damper in one dimension, which is explained in Chapter 4. In order to model a CMUT configuration, two different approaches exist for small and large deflections of the device membrane. Small deflection approach is proposed when the membrane dis-

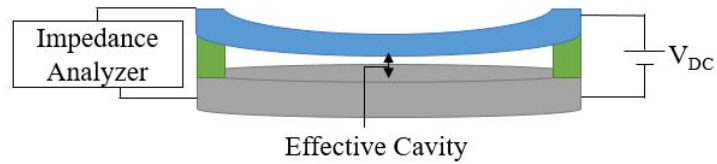


Figure 3.2: Schematic view of a CMUT with deflected top membrane.

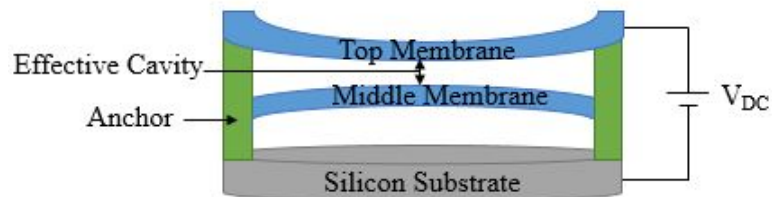


Figure 3.3: Schematic view of an M^3 -CMUT.

placement is small in comparison with membrane thickness while there is a linear relation between applied force and membrane displacement [72]. Whereas, in large membrane deflections, there is nonlinearity between membrane displacement and applied force [73].

In the unconventional application of CMUT in gas sensing technology, the top membrane is functionalized by a sensing material as shown in Figure 3.4. Various polymers can be used as sensing materials in gas sensing applications including polyisobutylene (PIB) [71] and polydimethylsiloxane (DKAP) [74]. When a CMUT gas sensor is exposed to a target gas, the sensing material adsorbs the target gas molecules which in return causes a change in effective mass of the sensing material that prompts changes in the top membrane's effective mass. This change in device's effective mass creates a shift in center resonant frequency of the sensor, which can be correlated to concentration level of the target gas molecules as shown in Equation 3.3.

Based on the review conducted, mass sensitivity per unit area is defined by Equation 3.4. The recent reported mass sensitivity per unit area is $130 \text{ zg/Hz}/\mu\text{m}^2$ [67], which is improved to $48.8 \text{ zg/Hz}/\mu\text{m}^2$ [74].

$$S_m = -2 \frac{m}{f_0 A_m} = -2 \frac{\rho t}{f_0} \quad (3.4)$$

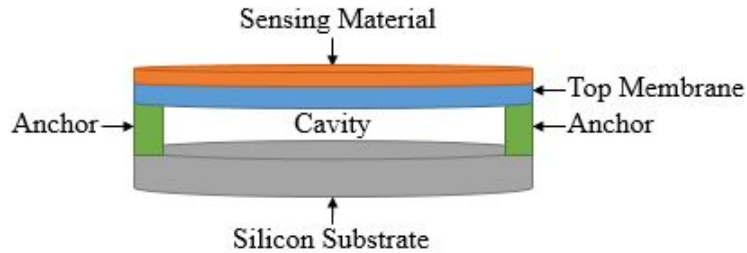


Figure 3.4: Schematic view of a CMUT-based gas sensor.

3.3 Conventional CMUT Sensor Microfabrication Techniques

Advanced micromachining techniques are used to fabricate CMUT-base gas sensors. Employing these technologies provide ease of circuit integration due to the material properties of silicon as the substrate. The two common CMUT fabrication techniques are sacrificial release process [75] as well as the wafer bonding process [69] that are investigated and discussed in this chapter.

3.3.1 Sacrificial Technique

Sacrificial fabrication process is a commonly used fabrication technique in CMUT technology. In this technique, a highly doped silicon substrate is covered by a layer of silicon nitride, which acts as an insulator as well as the etch-stop-layer for next fabrication step as presented in Figure 3.5 (a). The thickness of silicon nitride layer is important as it protects the silicon substrate during etching in next fabrication step [8]. In the next step a layer of metal is deposited as the bottom electrode, which is followed by depositing and patterning silicon dioxide (SiO_2) as the sacrificial layer illustrated in Figure 3.5 (b). To create top membrane, a layer of polysilicon is deposited on the sacrificial layer shown in Figure 3.5 (c). In traditional CMUT, a second silicon nitride layer is used as top membrane and is deposited on a patterned polysilicon layer. In order to release the top membrane and form the gap, etching holes are created on the silicon nitride to reach the underneath layer. After removing the sacrificial layer through a wet etching process in Figure 3.5 (d, e), a cavity is formed between silicon substrate and silicon nitride membrane. The device is then vacuumed and sealed by depositing another silicon nitride layer on top of the structure [61, 76, 77]. In the next step, metal layer is deposited on the top membrane to create

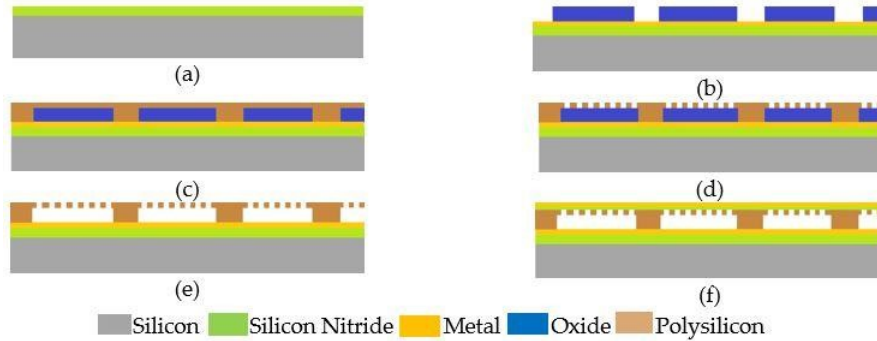


Figure 3.5: Schematic view of CMUT fabrication steps using sacrificial release process.

the top electrode as shown in Figure 3.5 (f). To functionalize the device as a gas sensor, a sensing material is deposited on the top membrane. In order to deposit the sensing material, different techniques are used including inkjet printing, spray coating, drop casting and polymer evaporation [78].

3.3.2 Wafer Bonding Techniques

Sacrificial release process has been widely used for CMUT fabrication due to its low cost and ease of fabrication. However, wafer bonding technique provides better control on the membrane thickness and cavity height in addition to a lower residual stress during fabrication. The drawbacks of wafer bonding process is surface roughness and cleanliness before bonding [79]. In this section, different wafer bonding techniques including wafer fusion bonding, LOCOS and anodic bonding are discussed.

3.3.2.1 Wafer Fusion Bonding

In the wafer bonding fabrication process two separate substrates are used. One silicon substrate is used for micromachining to create bottom electrode and cavity, while the second one is used for top membrane that will be bonded to the first substrate. A highly doped silicon wafer is used for first substrate while second substrate is traditionally a silicon on

insulator (SOI) wafer. A layer of silicon dioxide is thermally grown on the first silicon substrate based on desired cavity height and the cavity is patterned photolithographically as illustrated in Figure 3.6 (a). In order to create a thin insulating layer at the bottom of the cavities, another layer of silicon dioxide is thermally grown as shown in Figure 3.6 (b). A critical point in direct wafer bonding is having smooth surfaces to create Van der Waals bonds. Therefore, RCA cleaning is done on the SOI wafer in addition to buffering the oxide anchors on the first substrate before starting the bonding process. During the next step, both SOI wafer and oxide surface on the first substrate are brought together to build Van der Waals bonds in a hydrogen chamber, which is followed by annealing at 1100°C, as presented in Figure 3.6 (c). In order to release the top membrane, initially, the SOI handle wafer is removed followed by removal of buried oxide layer (BOX). To remove the SOI handle, BOX layer acts as the etch stop layer while the silicon membrane plays the same role during removing BOX layer. The main portion of SOI handle wafer is removed by mechanical grinding, which is further followed by wet etching using Potassium Hydroxide (KOH) to remove the rest of it as shown in Figure 3.6 (d). The BOX layer is then removed by wet etching using buffered oxide etchant (BOE) as seen in Figure 3.6 (e). After releasing the structure, a metal layer is deposited using sputtering technique and patterned on the top electrode as illustrated in Figure 3.6 (f) [55, 70, 80].

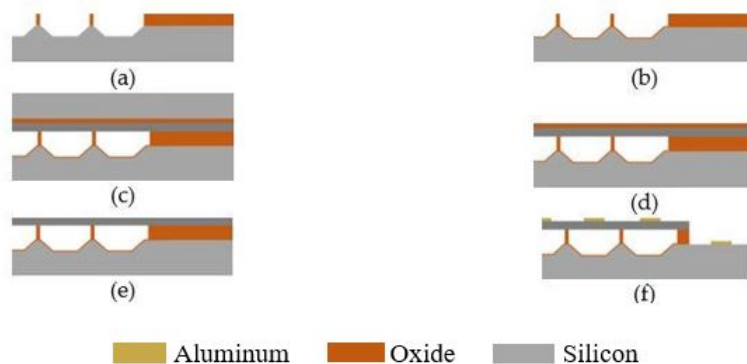


Figure 3.6: Schematic view of CMUT fabrication steps using wafer fusion bonding technique.

3.3.2.2 Local Oxidation of Silicon (LOCOS)

In this technique, silicon dioxide layer is locally grown to form a thinner cavity height by raising the bottom membrane and creating thick anchors while isolating each single device. This results in addressing existing drawbacks of wafer bonding process including parasitic capacitance and low breakdown voltage. In this technique, a highly doped silicon wafer is used as substrate which is followed by thermal wet oxidation as shown in Figure 3.7 (a). Another layer of silicon dioxide is thermally grown by wet oxidation and patterned to raise the bottom electrode as illustrated in Figure 3.7 (b). In the next step, a silicon dioxide layer is grown and patterned on a raised bottom membrane, which acts as the etch stop layer for patterning silicon nitride in the next step, shown in Figure 3.7 (c). A silicon dioxide layer is then grown and patterned for the anchors as illustrated in Figure 3.7 (d). The second substrate is a silicon on insulator (SOI) wafer, as shown in Figure 3.7 (e), which will be bonded to the substrate with the raised membrane. Next steps are similar to fusion bonding technique described in Section 3.3.2.1, which are bonding the SOI wafer, annealing the device in high temperature (around 1100°C), using Tetra Methyl Ammonium Hydroxide (TMAH) and buffered oxide etch (BOE) to remove the wafer handle and buffered oxide (BOX), respectively, to release the top membrane as illustrated in Figure 3.7 (f) [76,81,82].

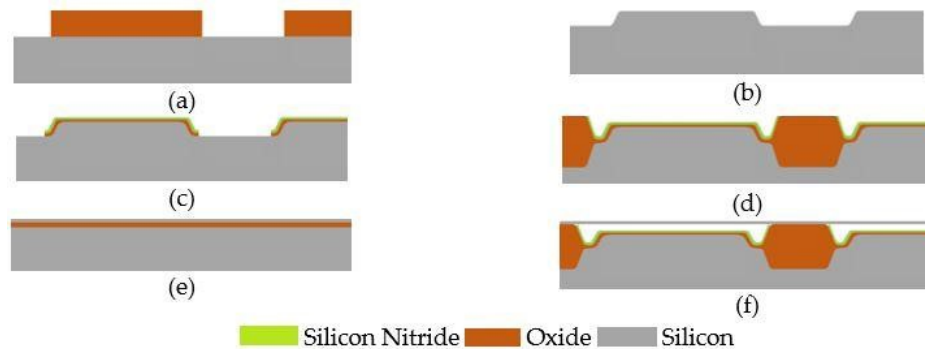


Figure 3.7: Schematic view of LOCOS fabrication steps.

3.3.2.3 Anodic Wafer Bonding

In anodic wafer bonding a borosilicate glass substrate is used as bottom substrate and silicon on insulator (SOI) wafer as top membrane [83, 84]. The substrate is cleaned by the piranha solution and then the cavity is patterned in borosilicate substrate by wet chemical etching or reactive ion etching (RIE), as illustrated in Figure 3.8 (a). In the next step, a metal layer is deposited using evaporation technique to form bottom electrode, wherein titanium is used as adhesion layer as shown in Figure 3.8 (b). Next, a silicon nitride layer is deposited on the membrane side of the SOI wafer using plasma enhanced chemical vapor deposition (PECVD) technique as seen in Figure 3.8 (c). This insulates the top membrane from electrically shorting in collapse modes. Then, the first substrate and SOI wafer are bonded, which is followed by etching the second wafer handle and BOX layer using TMAH and BOE etching, respectively, as illustrated in Figure 3.8 (d) [83]. In anodic wafer bonding, roughness of the bonding surfaces is not as critical as in the fusion bonding process. In addition, lower temperature processes provide ease of depositing metal electrode during the fabrication steps, which results in a low residual stress and fabrication of transparent CMUT structures. Moreover, employing glass substrate decreases the parasitic capacitance and provides higher reliability [85].

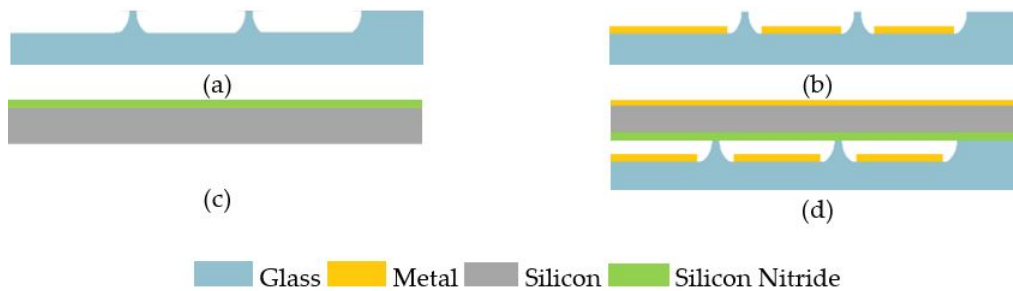


Figure 3.8: Schematic view of anodic bonding fabrication steps.

3.3.3 Flexible CMUT Structures

Flexible CMUTs are fabricated using polymers. In order to fabricate a flexible CMUT, the sacrificial release process can be used on a coated silicon substrate with polyethylene terephthalate (PET). SU8 is employed as structural material and copper as sacrificial layer. Platinum and gold are then deposited to form the electrode and silicon wafer is removed, as shown in Figure 3.9 [68].

CMUT can also be fabricated on a flexible silicon wafer, as illustrated in Figure 3.10 [86]. In order to make the silicon substrate flexible, trenches are created inside the silicon substrate by using deep reactive ion etching (DRIE). In the next step, the trenches are refilled by polydimethylsiloxane (PDMS) using dispensing system and spinning. Extra PDMS is later removed by lift off process and backside of the silicon substrate is etched by employing DRIE [86]. In the next step, regular processes for fabricating CMUT on the silicon substrate can be used as briefed in the Sections 3.3.1 and 3.3.2.

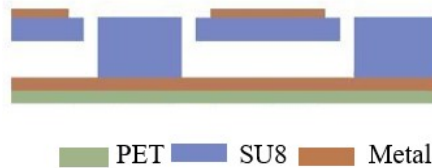


Figure 3.9: Schematic view of a flexible CMUT.

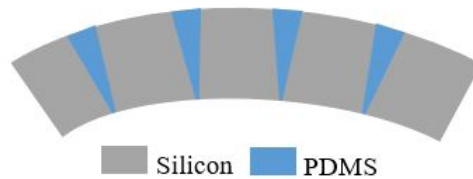


Figure 3.10: Schematic view of a flexible silicon substrate.

3.4 Conclusions

In this chapter, CMUT-based gas sensors are reviewed. Structure and mechanism of operation of these devices are discussed as well as their fabrication techniques. The presented advanced microfabrication techniques in this chapter include sacrificial process, different wafer bonding procedures including fusion bonding, anodic bonding and local oxidation of silicon (LOCOS) in addition to flexible CMUT structures.

Although the sacrificial technique is the standard method to fabricate a CMUT, based on the review in this chapter the wafer fusion bonding is proposed as a candidate technology to fabricate a CMUT-based gas sensor. Since in the wafer fusion bonding cavity height and anchors are created independently, it allows us to have a uniform structure while providing precision in the device dimensions as well as enhancing sensitivity of the sensor. In addition, this technique results in a better device performance since it does not require to release the top membrane by creating sacrificial channels.

Chapter 4: Developed Bilayer CMUT-Based Gas Sensor Model with Circular Membrane

4.1 Introduction

Capacitive micromachined ultrasonic transducer (CMUT) was introduced in 1994 [87]. Since then, CMUTs have been used as an alternative for conventional piezoelectric transducers in ultrasonic and underwater imaging applications [87]. In this work and unlike conventional transducer application, this device is configured as a mass resonant sensor, where the CMUT technology is implemented to detect and measure the concentration of various target gases. Therefore, this new CMUT structure needs to be fully studied and developed for gas sensing applications. The objective of this thesis is to propose, for the first time, an advanced analytical model that provides a method to design an optimize a highly sensitive CMUT gas sensor for complex environment with low concentration levels of target gases. In this thesis, critical design parameters including radius, membrane thickness, cavity height as well as structural material are extensively studied. Using the aforementioned design parameters, a comprehensive CMUT analytical model is developed. Furthermore, the proposed advanced analytical model is employed to design a sensitive CMUT gas sensor, followed by conducting FEA simulations for low gas concentration levels described in Chapter 5.

4.2 Proposed Analytical Model for Conventional CMUT Structure

Plate or membrane theory can be employed to model a CMUT structure [88]. In this thesis, a comprehensive analytical model is developed to predict resonant frequency of the device, which is fully matched with the very well-known plate theory.

The proposed analytical model employs mass-spring-damper theory [89] to model the behavior of a single cell CMUT-based gas sensor with circular plate, which is shown in Figure 4.1. In this model, it is assumed that a uniform pressure is applied to an isotropic and homogeneous membrane with clamped edges and linear elastic deformation. Furthermore, it is assumed that the device operates under small deflection condition [90] in response to the absorption of the target gas.

The structure is modeled using mass-spring damper, as shown in Figure 4.1. The mass-spring damper treats CMUT as a dynamic capacitance with movable mass. As shown in Figure 4.1, in the modeled CMUT, bottom electrode is fixed while the top membrane with stiffness k suspended on top of it and acts as a movable and connected mass to the spring. When the DC bias voltage is applied to the top membrane, an electrostatic force is created across the CMUT cavity. A downward deflection in the device top membrane is created towards the bottom electrode. The membrane mechanical restoring force resists this deformation due to the k , stiffness of the membrane. The damping by the sensor's surrounding media represented below as B [91].

When DC bias voltage is applied, at an equilibrium point, the electrostatic force and the mechanical force become equal in magnitude as shown in Equation 4.1,

$$kx = \frac{-\epsilon_0 A_m}{2} \left(\frac{V_{DC}}{x} \right)^2 \quad (4.1)$$

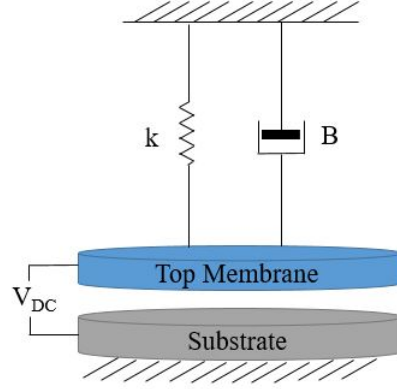


Figure 4.1: Schematic view of a CMUT mass-spring-damper model

where ε_0 , A_m , V_{DC} and x are the permittivity of vacuum, effective membrane area, applied DC bias voltage and membrane displacement, respectively. Based on Equation 4.1, if the electrostatic force due to V_{DC} , dominates the mechanical force related to k , the top membrane collapses. Therefore, the stable state for the membrane deflection is when Equation 4.2 is valid,

$$\frac{dF}{dx} < 0 \Rightarrow \frac{\varepsilon_0 A_m V_{DC}^2}{(h_0 - x)^3} - k < 0 \quad (4.2)$$

where F is the total applied force. Equation 4.2 stays valid, when membrane displacement is smaller than one third of the initial cavity height, h_0 , as shown in Equation 4.3.

$$x < \frac{h_0}{3} \quad (4.3)$$

Based on Equations 4.2 and 4.3, critical DC bias voltage known as collapse voltage, defines the maximum tolerable applied voltage to the device. The collapse voltage is calculated by Equation 4.4 [92].

$$V_{Collapse} = \sqrt{\frac{8kh_0^3}{27\varepsilon_0 A_m}} \quad (4.4)$$

Based on the diaphragm theory [89], deformation of a point located at radial distance b in a circular membrane with clamped edges, which is exposed to a uniform pressure P is calculated from Equation 4.5,

$$y = \frac{(3(1 - \nu_m^2)Pr^2)}{16E_mt_m^3}(r_m^2 - b)^2 \quad (4.5)$$

where r_m is the radius of the membrane. Since the membrane is circular with clamped edges, the maximum displacement occurs at the center of the membrane, which is driven as Equation 4.6.

$$y = \frac{3(1 - \nu_m^2)Pr^4}{16E_mt_m^3} \quad (4.6)$$

By substituting the spring force, $-kx$, in the membrane displacement, Equation 4.6, and calculating k , Equation 4.7 is achieved, which defines the geometrical effect of the membrane on the spring constant.

$$k = \frac{-F_{spring}}{x} = \frac{16\pi E_mt_m^3}{3(1 - \nu_m^2)r_m^2} \quad (4.7)$$

In a CMUT structure, when the DC bias voltage is applied to the top membrane, it deflects towards the bottom electrode. The applied voltage makes the membrane softer to deform by decreasing the spring constant. Therefore, this makes the membrane to operate close to the optimum point. This phenomenon is known as the spring softening effect and is caused by the applied DC bias voltage [93].

Since CMUT membranes act as dynamic capacitors, the applied force generated by this capacitive element is calculated by Equation 4.8,

$$F_{Capacitor} = -\frac{d}{dx}\left(\frac{1}{2}CV_{DC}^2\right) = -\frac{1}{2}V_{DC}^2\left(\frac{d}{dx}\left(\frac{\epsilon_0 A_m}{h_{eff} - x}\right)\right) = \frac{\epsilon_0 A_m V_{DC}^2}{2(h_{eff} - x)^2} \quad (4.8)$$

where h_{eff} is effective cavity height and calculated from Equation 4.9,

$$h_{eff} = h_0 + \frac{t_m}{\varepsilon_m} \quad (4.9)$$

where ε_m is the relative permittivity of the top membrane. By substituting Equation 4.8 in Equation 4.10 and the Newton's second law of motion, Equation 4.11 is achieved.

$$F = F_{Spring} + F_{Capacitor} \quad (4.10)$$

$$m \frac{d^2 x}{dt^2} - \frac{\varepsilon_0 A_m V_{DC}^2}{2(h_{eff} - x)^2} + kx = 0 \quad (4.11)$$

By employing the first order Taylor expansion in Equation 4.11, Equation 4.12 is obtained, which is spring softening effect due to the applied DC bias voltage [89].

$$m \frac{d^2 x}{dt^2} + \left(k - \frac{\varepsilon_0 A_m V_{DC}^2}{h_{eff}^3} \right) x = \frac{\varepsilon_0 A_m V_{DC}^2}{2h_{eff}^2} \quad (4.12)$$

In addition to the effect of geometrical parameter on the spring constant, Equation 4.7, as well the spring softening effect due to the applied DC bias voltage, Equation 4.8, residual stress also influences the spring constant since thin films prone more to have stress depends on the material. Residual stress is defined as the stress in the structure when the external forces are removed. The assumed stress in this model contains intrinsic as well as thermal stresses of the device structural materials. Intrinsic stress can be created due to the different deposition temperature processes including spraying, coating, sputtering, and vapor deposition techniques. Thermal stress is created due to the different coefficients of thermal expansion (CTE) in different layers of the CMUT structural materials [94]. The total residual stress σ_{totm} is defined in 4.13,

$$\sigma_{totm} = \sigma_{thm} + \sigma_{0m} \quad (4.13)$$

where σ_{thm} and σ_{0m} represent the thermal stress and intrinsic stress of the membrane, respectively. By combining 4.7, 4.12 as well as 4.13, Equation 4.14 is obtained, which represents the total stiffness of the top membrane in a conventional circular CMUT.

$$k = \frac{16\pi E_m t_m^3}{3(1 - \nu_m^2) r_m^2} - \frac{\epsilon_0 A_m V_{DC}^2}{h_{eff}^3} + 4\pi \sigma_m t_m \quad (4.14)$$

Equation 4.14 is substituted in Equation 4.15 to calculate center resonant frequency of the deigned CMUT,

$$\omega_r = 2\pi f_r = \sqrt{\frac{k}{m_m}} \quad (4.15)$$

where m_m is the effective mass of the top membrane.

In this work and in an unconventional approach, the traditional CMUT configuration is employed as a mass resonant sensor in gas sensing technology. In a CMUT-based gas sensor the top membrane is functionalized by a sensing layer, which forms a bilayer structure. Therefore, effect of critical parameters of the added sensing layer on the resonant frequency of the device need to be considered in the analytical model. These parameters do not exist in the analytical model for a conventional CMUT as discussed in this section. Therefore, in this work and in the absence of the comprehensive model, a novel analytical model is proposed and developed in section 4.3, which includes critical design parameters of a bilayer circular CMUT-based gas sensor including radius, membrane thickness, cavity height and material properties of the CMUT. The proposed model also includes thickness, mass and material properties of the sensing layer in addition to the residual stress for the top membrane and the sensing material.

4.3 Proposed Analytical Models for CMUT-Based Gas Sensor

Gas Sensor

In order to develop a CMUT sensor capable of detecting a target gas as discussed in the previous chapters, a sensing material needs to be employed in the traditional CMUT design. Once the target gas molecules are absorbed by the device sensing material, the overall mass of the top membrane will increase. Therefore, the resonant frequency of the CMUT device will shift in response to the changed mass as shown in 4.15, which can be correlated to the presence of the target gas in the sensor environment. As a result, and in order to design and optimize a CMUT sensor, the change in the center resonant frequency of the device due to the bi-layer construction along with varying mass of the CMUT sensor need to be considered in developing the proposed analytical model. By employing the mass-spring-damper model for a conventional CMUT, which is shown in Figure 4.1, a bi-layer CMUT is modeled and illustrated in Figure 4.2. In this model, K_{bi} , B_m and B_s represent stiffness for a bilayer circular CMUT-based gas sensor, damping due to the membrane and damping due to the sensing material, respectively.

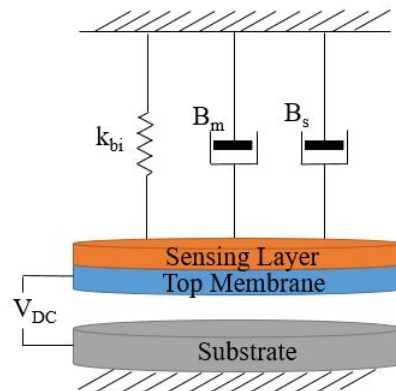


Figure 4.2: Schematic view of a mass-spring-damper for a bilayer CMUT-based gas sensor.

In this chapter, a new comprehensive analytical model is proposed taking the physical parameters of the structure into consideration. In order to propose the comprehensive analytical model for CMUT-based gas sensor, three models are developed to find effects of critical parameters on center resonant frequency of the device, as presented in Table 4.1. These parameters include radius, membrane thickness and cavity height in addition to the material properties of the top membrane and the sensing layer. Material properties of a conventional CMUT are considered in flexural rigidity, D , as shown in Equation 4.16 [90].

$$D = \frac{E_m t_m^3}{12(1 - \nu_m^2)} \quad (4.16)$$

where ν_m , E_m and t_m are the Poisson's ratio, Young's modulus and membrane thickness, respectively. Membrane and sensing layer residual stresses along with the membrane stiffness and the softening effect due to the applied DC bias voltage are all investigated and considered. 3D electromechanical FEA simulations and optimizations are further conducted for low gas concentration levels, which will be discussed in Chapter 5. During this study, three initial models are developed as shown in Table 4.1, including one-layer, two-layer as well as multi-layer model without thermal residual stress are developed. In Table 4.1, D , D_{eff} , σ_{tot} , σ_{ths} and σ_{0t} are flexural rigidity, effective flexural rigidity, total residual stress, sensing material thermal stress and intrinsic stress of top membrane, respectively. These models then provide the platform for the accurate comprehensive bi-layer analytical model proposed for the developed circular CMUT-based gas sensor.

In the one-layer model, effect of the sensing layer including material properties, mass and thickness as well as the residual stress are ignored and the structure is considered as the conventional one layer CMUT by considering the flexural rigidity. Equation 4.14 is used to calculate the stiffness of the top membrane in the one-layer model while residual stress is ignored to evaluate only the effects of top membrane's geometrical parameters and spring softening. However, in a bilayer CMUT-based gas sensor, existing sensing layer

Table 4.1: Design parameters in the developed and proposed models.

	Flexural Rigidity D/D_{eff}	Top Membrane Residual Stress	Sensing Layer Residual Stress
One-Layer Method	D	-	-
Two-Layer Method	D	σ_{tot}	σ_{ths}
Multilayer Model without Thermal Residual Stress	D_{eff}	σ_{0t}	-
The Proposed Bilayer Model	D_{eff}	σ_{tot}	σ_{ths}

which can also change due to target gas adsorption, affects center resonant frequency of device. In addition, fabrication of a thin layer of the sensing material, intend to have high residual stress, which none of these effects are included in the One-Layer analytical model of a traditional CMUT.

The one-layer model optimized to the two-layer model by adding total residual stress of the top membrane, σ_{tot} , as well as the thermal stress, σ_{ths} , mass, m_s , and thickness, t_s , of the sensing material. In two-layer model, Equation 4.15, is developed to Equation 4.17, which includes mass of the top membrane, m_m , and the sensing material, m_s , in addition to the membrane stiffness, k . In two-layer model, contribution of mass of the top membrane and sensing layer in center resonant frequency are considered, equally as shown in Equation 4.17. By developing Equation 4.14 while including aforementioned parameters, membrane stiffness in Two-Layer model is derived in Equation 4.18. Two-Layer model is developed to investigate effect of thermal stress of the sensing material when its geometrical parameters are neglected. In this model, flexural rigidity is considered the same as the One-Layer model while material properties of the sensing layer including Poisson's ratio, ν_s , Young's modulus, E_s and density of sensing material, ρ_s are ignored. In the developed Two-Layer model, total residual stress of the top membrane, σ_{totm} , is considered while only thermal stress in the sensing layer is included.

$$f_r = \sqrt{\frac{k}{m_m + m_s}} \quad (4.17)$$

$$k = \frac{16\pi E_m t_m^3}{3(1 - \nu_m^2)r_m^2} - \frac{\epsilon_0 A_m V_{DC}^2}{h_{eff}^3} + 4\pi(\sigma_{totm}t_m + \sigma_{ths}t_s) \quad (4.18)$$

σ_{ths} is the thermal stress of the sensing layer, as shown in Equation 4.19,

$$\sigma_{ths}(y) = -\frac{2}{3}\alpha E_s(T_s - T_f)\left(\frac{6y^2}{t_s^2} - \frac{1}{2}\right) \quad (4.19)$$

where α , T_s , T_f and t_s are the thermal expansion coefficient, solidification temperature, final temperature and thickness of the sensing material, respectively at any given point of sensing material, y , as shown in Figure 4.3 [95].

The Two-Layer model, however, ignores the geometrical parameters of the sensing layer even though the thermal stress of it is included. Therefore, by adding the sensing material to the structure, the first parameter which needs to be considered is the effective flexural rigidity of the device, which as a results adds the critical parameters of the sensing component to the model. In this thesis, it is assumed that the membrane deflection is smaller than the membrane thickness, based on the small deflection theory [96]. Hence, effective flexural rigidity can be employed in the model. This theory is applicable when the maximum displacement of the membrane is smaller than 20% of its thickness, which is valid for this study [97]. Therefore, Kirchoff theory [98] can be employed for multilayer membranes with different material properties as shown in 4.21. Consequently, in order to investigate effect of sensing material properties, flexural rigidity is replaced by the effective flexural rigidity, D_{eff} , as shown in Equation 4.20, in the Multilayer model without Thermal Residual Stress. In this model, residual stress of the sensing layer is ignored. The

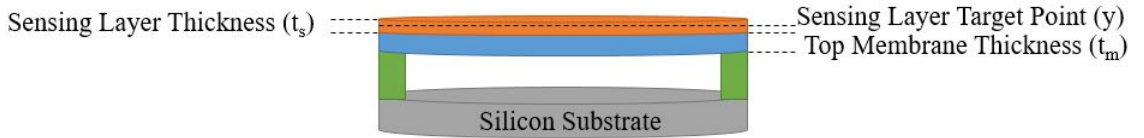


Figure 4.3: Schematic view of the CMUT structure and the target point at y .

effective flexural rigidity can be calculated through Equations 4.21 to 4.24. This assumption considers effect of material and geometrical parameters of the sensing layer, which are not included in the developed One-Layer and Two-Layer Models. These parameters are thickness, Young's modulus and Poisson's ratio of the sensing material in addition to the properties of the top membrane. Moreover, only the intrinsic residual stress of the top membrane is included while the residual stress of the sensing layer is ignored. These assumptions show that all critical parameters of the sensing material and its residual stress are effectively involved in center resonant frequency and cannot be neglected.

$$k = \frac{64\pi D_{eff}}{r_m^2} - \frac{\varepsilon_0 A_m V_{DC}^2}{h_{eff}^3} + 4\pi\sigma_{0m}t_m \quad (4.20)$$

$$D_{eff} = \frac{AC - N^2}{A} \quad (4.21)$$

A, N and C are parameters, which can be calculated through Equations 4.22 to 4.24,

$$A = \frac{E_m}{1 - \nu_m^2}t_m + \frac{E_s}{1 - \nu_s^2}t_s \quad (4.22)$$

$$N = \frac{E_m}{2(1 - \nu_m^2)}t_m^2 + \frac{E_s}{2(1 - \nu_s^2)}((t_s + t_m)^2 - t_m^2) \quad (4.23)$$

$$C = \frac{E_m}{3(1 - \nu_m^2)}t_m^3 + \frac{E_s}{3(1 - \nu_s^2)}((t_s + t_m)^3 - t_m^3) \quad (4.24)$$

where E_s , ν_s , t_s are Young's modulus, Poisson's ratio and the thickness of the sensing material, respectively.

Finally, the Proposed Bilayer model includes the effective flexural rigidity illustrated in Equations 4.21 through 4.24, as well as the total residual stress of the top membrane and thermal stress of the sensing layer, as shown in Equations 4.13 and 4.19, respectively. These

parameters are included in the proposed analytical model for a bilayer circular CMUT-based gas sensor. This comprehensive model is based on the previously developed models, geometrical and material properties of the sensing layer as well as the residual stress that are effectively involved in the device performance and cannot be ignored. This proposed analytical model and the effective spring constant, k_{bi} , of the sensor flexible membrane is shown in Equation 4.25, which considers all the known critical parameters of the top membrane and the sensing component.

$$k_{bi} = \frac{64\pi D_{eff}}{r_m^2} - \frac{\epsilon_0 A_m V_{DC}^2}{h_{eff}^3} + 4\pi(\sigma_{totm}t_m + \sigma_{thst_s}) \quad (4.25)$$

In this proposed model, polymers are considered as intrinsic stress-free materials, which is the case for commonly used polymers. In addition, the total residual stress is typically obtained through experimentation. In this thesis, the commonly obtained values for these materials, $130MPa$, $143MPa$ and $170MPa$ are used for residual stress of the silicon, polysilicon and silicon nitride top membranes, respectively [99]. However, the model can be simply modified if the membrane material differs from the above assumed commonly used materials. As a result, by developing three different models, One-Layer, Two-Layer and Multilayer without Thermal Residual Stress, it is shown that properties of sensing layer are effectively involved in resonant frequency of device. These sensing material parameters are not negligible and includes thickness, residual stress, Young's modulus, Poisson's ratio, density and residual stress. Therefore, a comprehensive analytical model is proposed in this work. This proposed model referred to as the Bilayer Model hereafter for a CMUT-based gas sensor with circular geometry. This model incorporates all the critical parameters of the top membrane as well as the sensing layer, as shown in Equation 4.25. In addition, the proposed comprehensive model incorporates membrane softening effect due to the applied DC bias voltage and residual stresses.

4.4 Equivalent Circuit Model of a Conventional CMUT

As discussed in the previous chapters, a CMUT device acts as an electromechanical system, which combines mechanical and electrical operational properties. A CMUT cell can be modeled and analyzed by replacing mechanical parameters such as velocity and force by electrical components including current and voltage. The differential equation shown in Equation 4.12, is described by the Mason's equivalent circuit model of a CMUT structure [100,101]. The model consists of mechanical and electrical ports in addition to a transformer for a linearized parallel plate as shown in Figure 4.4. The electrical port models a CMUT as a capacitor as well as a resistor while the mechanical port models the mechanical impedances of the proposed analytical model [100,101].

By replacing the mechanical parameters including velocity and force, in addition to the capacitors and resistors of the existing components in the device an equivalent electrical theoretical model is derived as shown in Figure 4.5.

In this model, R_{Source} , C_0 and C_{Paras} , are the source resistance, the clamped parallel plate capacitance for the DC bias voltage and the parasitic capacitance, respectively. R_{Bm} , $-C_{Spring}$, C_m , L_{Medium} and L_m are the electrical equivalent substitutions for damping, spring softening effect due to the applied DC bias voltage, top membrane capacitor and loaded

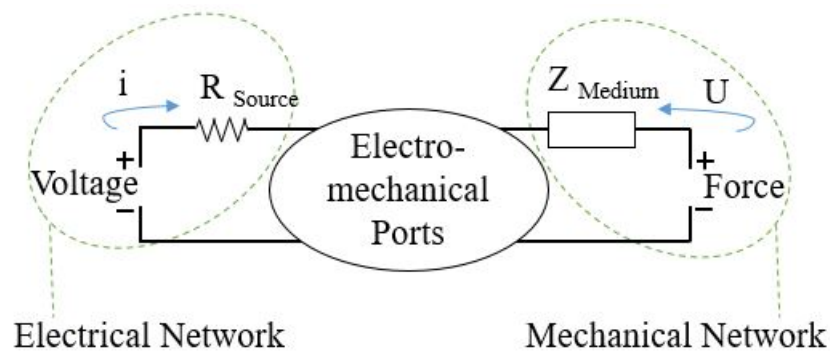


Figure 4.4: Basic view of the Mason's equivalent circuit.

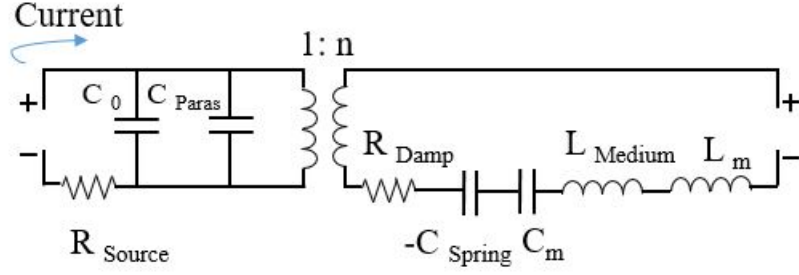


Figure 4.5: Equivalent circuit model of a conventional CMUT cell.

mass due to the medium and mass of the top membrane, respectively. The clamped parallel plate capacitance, C_0 , can be calculated from Equation 4.26.

$$C_0 = \frac{\epsilon_0 A_m}{h_{eff}} \quad (4.26)$$

In this model, n is the transformer ratio, which is a function of the applied DC bias voltage and consequently the electrostatic force. The transformer ratio can be described as in Equation 4.27,

$$n = E_0 C_m = \frac{\epsilon_0 A_m V_{DC}}{h_{eff}^2} \quad (4.27)$$

where, the electric field is driven in Equation 4.28.

$$E_0 = \frac{V_{DC}}{h_{eff}} \quad (4.28)$$

4.5 Proposed Equivalent Circuit Model of a Bilayer CMUT-Based Gas Sensor

In a CMUT-based gas sensor, the conventional CMUT transducer is functionalized by a sensing material. When the device is exposed to a target gas, the target gas molecules are

absorbed into the sensing layer, which results in a change in the properties of the sensing layer including its mass and resistivity. Therefore, in order to accurately develop the equivalent electric circuit model of a CMUT-based gas sensor, the sensing layer is modeled as a capacitor as well as a variable inductor and resistor to accommodate the target gas absorption. The equivalent circuit model for a CMUT-based gas sensor is shown in Figure 4.6.

In this work, R_m and C_m are representing the top membrane's resistance and capacitance respectively. They are added to the circuit in order to develop a comprehensive analytical model of the electrical properties of the top membrane. In this developed model, $R_s + \Delta R$ represents the sensing layer resistivity in addition to the resistance change due to the target gas absorption. In this model presented in Figure 4.6, C_s , $C_{Paras-s}$ and $C_{Param-m}$ are the sensing layer capacitor, parasitic capacitance between the sensing layer and the bottom electrode and the generated parasitic capacitance between the top membrane and the bottom electrode, respectively. R_{Bs} and $L_s + \Delta m$ represent damping and the mass equivalent of the sensing layer, which changes due to the target gas absorption. If the top membrane and the sensing layer are fabricated from conductive materials, the parasitic capacitors, $C_{Paras-s}$ and $C_{Paras-m}$ are very low and negligible. However, if nonconductive materials like silicon nitride or nonconductive polymers are used as the top membrane and the sensing layer, the parasitic capacitances play an important role in the circuit model and cannot be ignored.

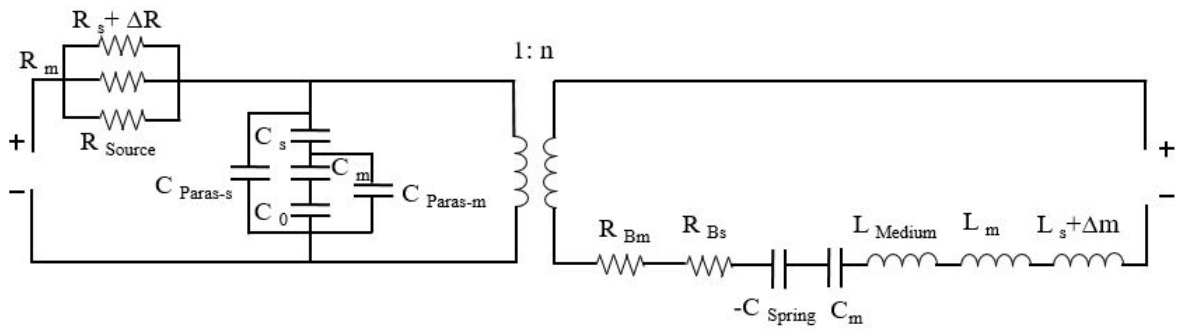


Figure 4.6: The developed equivalent circuit model for a CMUT-based gas sensor.

4.6 Conclusions

In order to effectively design, develop and incorporate CMUT-based gas sensor for low concentration level gas detection, in this chapter, a novel comprehensive analytical model is proposed. This model predicts the varying center resonant frequency of a bilayer circular CMUT-based gas sensor in response to a target gas exposure. In order to develop the proposed analytical model, mass-spring-damper phenomena is employed for a linear elastic deformation of the membrane and for small deflections. In this proposed model, critical parameters of the top membrane and the sensing layer are considered including the radius, thickness, material properties and the residual stresses as well as the effective cavity height. Furthermore, the proposed model includes the spring softening effect due to the applied DC bias voltage in addition to the membrane stiffness effect. Moreover, the equivalent electric circuit model is developed that employs the Mason's equivalent model. The critical parameters are further extensively investigated in Chapter 5 by conducting FEA simulations. In addition, the proposed analytical model is employed to enhance the sensitivity of a CMUT-based gas sensor for the frequency range of 5MHz and 25MHz as a sample application frequency. The investigation of the critical parameters is followed by comparing the proposed analytical model to the FEA simulation results.

Chapter 5: Proposed Micromachined CMUT-Based Gas Sensors - Design, Simulations, and Evaluations

5.1 Introduction

Conventional CMUT transducers as introduced and studied in Chapter 3, consist of a top and a bottom membranes that are separated via an air or a vacuum cavity. However, when a CMUT is employed as a gas sensor, the top membrane is functionalized by utilizing a sensing material designed and optimized to be responsive to a target gas. When the sensor is exposed to an environment containing the target gas, the gas molecules are absorbed by the sensing material, which causes a shift in the center resonant frequency of the device. Therefore, both geometrical and material properties of the top membrane and sensing layer effectively contribute in changes in the center resonant frequency, and consequently the sensitivity of the CMUT-based gas sensor. As the application of CMUT structures in the gas sensing technology is new, this thesis presents, for the first time, a comprehensive analytical model proposed for use in MUT-based sensor platforms. The proposed analytical model effectively includes and combines the physical and material properties of the device as well as the residual stresses of the structural and sensing materials, as presented in Chapter 4. The proposed analytical model is further employed to design an optimized circular bilayer CMUT-based gas sensor. In this chapter, FEA simulations are conducted using COMSOL Multiphysics to enhance the sensitivity of the proposed device. The criti-

cal design parameters of a bilayer circular CMUT-based gas sensor are investigated while considering the feasibility of micro and nano fabrication technology. In addition, conducted FEA simulations are used to evaluate the effect of each parameter on the center resonant frequency of the device while compared with the proposed analytical model. Critical parameters include radius size, membrane thickness, cavity height, structural material as well as the mass and thickness of the sensing material. Additional information about the accuracy of COMSOL Multiphysics simulations, as well as the details on system setup and the computer specifications are also provided in this chapter.

5.2 COMSOL Multiphysics and System Setup

In this thesis, COMSOL Multiphysics software, version 5.4, is used to conduct FEA simulations in order to investigate the effect of critical parameters of a bilayer circular CMUT-based gas sensor on the device performance. COMSOL Multiphysics features various advanced physics solvers and allows for coupled examination of multidisciplinary problems that is required in the study presented in this work. In this thesis, Eigenfrequency Prestressed analyses are conducted using the Solid Mechanics and Electrostatics modules, which allow for detailed analysis of electromechanical forces. This software is run on a Windows machine consisting of sixteen $2GHz$ Intel Xenon cores with a total of $384GB$ of RAM.

5.2.1 Domain Meshing

In order to conduct FEA simulations, meshing is applied through a physics-controlled process. Simulated devices in this chapter have a dimension range from tens of nanometers to hundred microns in the same design. Therefore, accurately meshing the device should be considered, specifically when different thicknesses of the membrane and the sensing

Table 5.1: Number of elements for a bilayer circular CMUT-based gas sensor with $9\mu\text{m}$ radius and 500nm silicon membrane which is functionalized by 100nm PIB while the cavity is 140nm .

Mesh	Tetrahedron Elements	Triangle Elements	Total Number of Elements
Normal	98,905	30,402	129,307
Fine	310,853	73,494	384,347
Finer	501,770	111,194	612,964

layer exist. Consequently, Normal, fine as well as finer meshes were employed on a bilayer circular CMUT-based gas sensor with $9\mu\text{m}$ radius, 140nm cavity height and 500nm silicon membrane, functionalized by a 100nm PIB sensing material in order to evaluate the impact of meshing on simulations. The number of elements for different investigated meshes are provided in Table 5.1 and the portions of the meshed structure with normal, fine and finer grids are shown in Figure 5.1.

In these COMSOL simulations, since by applying the DC bias voltage the top membrane deflects toward the bottom electrode, therefore, the vacuum cavity between the membranes is considered as the deforming domain. The chosen deforming domain consists of a moving mesh to allow for dynamically conducting the simulations when mechanical movement occurs. By increasing the number of elements, the change in the frequency associated with the simulations decreases. Therefore, by defining the parameter $1/N$, where N represents the number of elements, an examination of how higher N contributes to lowering the error of simulations can be performed. The result shown in Figure 5.2 includes a plot

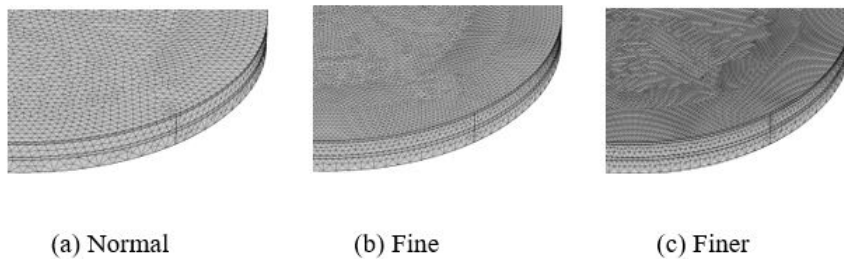


Figure 5.1: Portion of the meshed CMUT-based gas sensor.

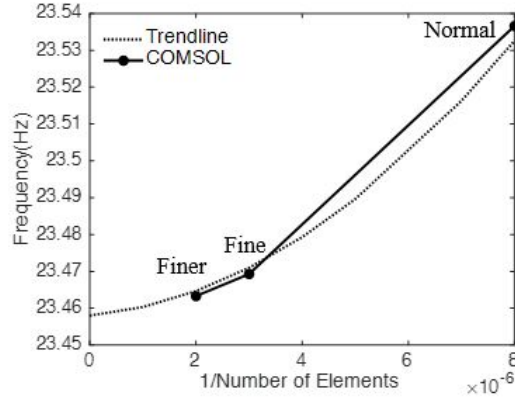


Figure 5.2: Frequency dependency associated with number of elements.

of simulated frequencies versus $1/N$. A curve is fitted for the frequency associated with normal, fine and finer meshes, which is shown as a trendline in Figure 5.2. The interception between the trendline and frequency axis represents the point, in which, N tends to infinity that means the simulations error due to the number of elements is minimized. The uncertainty quantification for the finer grid is less than 1%.

Based on the above results, all remaining bilayer circular CMUT-based gas sensors in this thesis simulations were meshed with finer grids in order to eliminate any potential deviation.

5.2.2 Boundary Conditions for FEA Simulations

In this thesis, a bilayer circular CMUT-based gas sensor configuration is designed in COMSOL Multiphysics as shown in Figure 5.3. Due to the nature of the design, not all parts of the structure are involved in vibration, therefore, effective areas of the device were designed in COMSOL in such a way that anchors are ignored. Boundary conditions are applied on the designed geometry in order to enhance the accuracy of the simulations.

As illustrated in Figure 5.4 (a), highlighted parts in blue show that the silicon substrate is fixed along with the perimeter of the top membrane and sensing layer. This creates a clamped edges device. The top membrane is free to move as highlighted in blue and

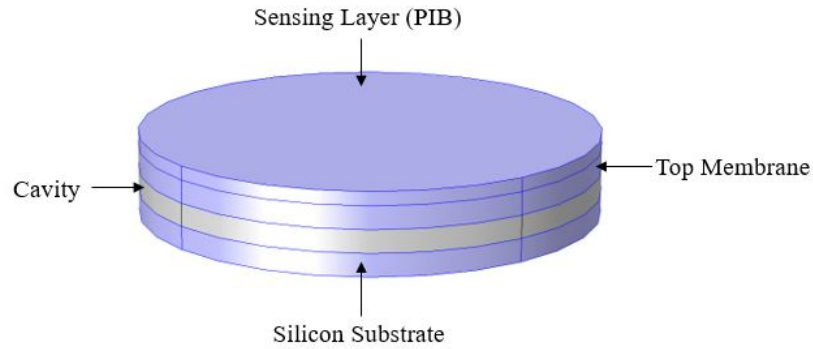


Figure 5.3: Schematic view of the designed device in COMSOL Multiphysics.

shown in Figure 5.4 (b), that in return allows for the membrane deflection towards the bottom electrode when activated by an applied DC bias voltage between the top and bottom membranes.

In the COMSOL simulation, the vacuum cavity between the top and the bottom membranes is defined as a deforming domain as highlighted in blue and shown in Figure 5.5, to allow for the created electrostatic force across the cavity to cause a deflection in the top membrane.

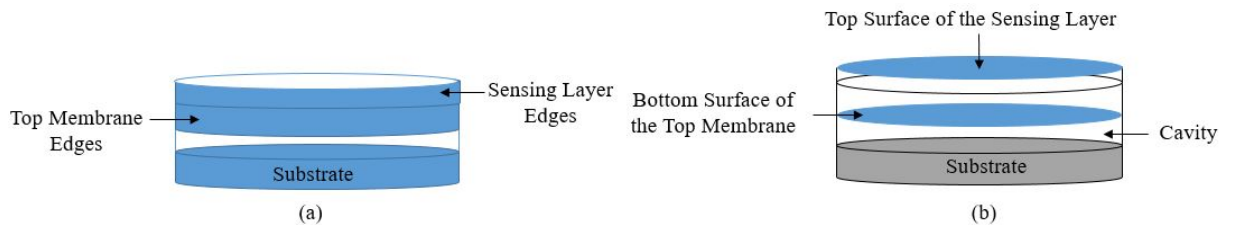


Figure 5.4: (a) Fixed constraints includes bottom membrane and perimeter of the top membrane and sensing layer, (b) free boundaries, which consists of the top and bottom surfaces of the top membrane and the sensing layer.

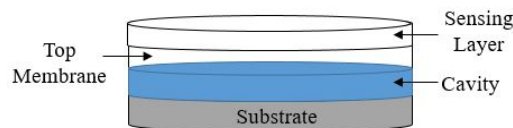


Figure 5.5: Vacuum cavity (the highlighted domain in blue) is defined as the deforming domain.

The DC bias voltage is applied to the top surface of the top membrane as highlighted in blue and illustrated in Figure 5.6 (a), whereas the bottom electrode is grounded as shown in Figure.5.6 (b). Depending on the type of fabrication technique including wafer bonding or sacrificial technique such as PolyMUMPs, and the structural material properties, the top membrane can be conductive or nonconductive. Therefore, if the top membrane is conductive, location of the applied DC bias voltage on it, does not affect the center resonant frequency. However, if the top membrane is nonconductive, center resonant frequency of the sensor can be affected by the capacitance due to the sensing material resistivity. Therefore, in the conducted FEA simulations, top surface of the top membrane is considered as the terminal, in order to consider the capacitance of the top membrane. In addition, the capacitance due to the top membrane is included in the analytical model as discussed in Chapter 4.

In order to evaluate effect of fringing fields outside the air cavity on the sensor’s performance, an air cylinder considered in the area surrounding of the bilayer circular CMUT-based gas sensor, as shown in Figure 5.8. Conducted electrostatic FEA simulations on the device in Figure 5.7, shows that the fringing field has less than 1% effect on the resonant frequency. Due to this small difference, the effect of air around the structure is ignored in all simulations.

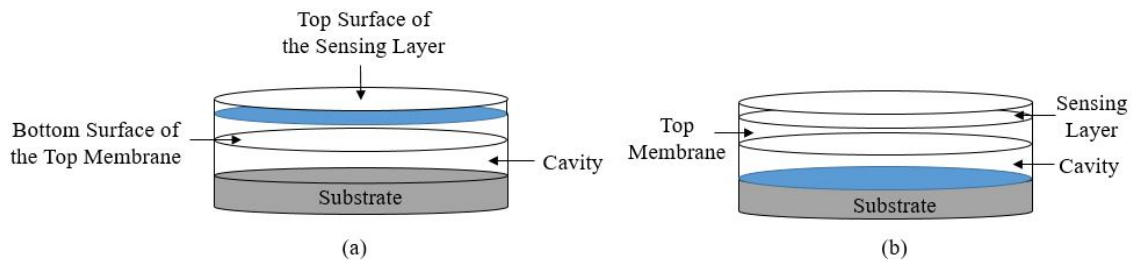


Figure 5.6: (a)The top surface (highlighted in blue) of the top membrane is defined as the terminal to apply DC bias voltage. (b) the bottom electrode is grounded.

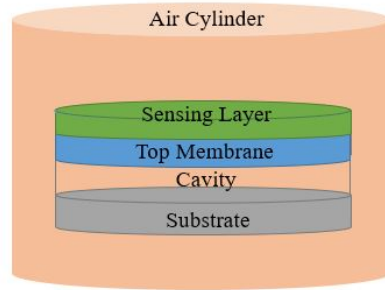


Figure 5.7: Schematic view of a CMUT-based gas sensor when damping is considered.

5.2.3 Proposed Structural Materials in FEA Simulations

The conducted FEA simulations in this chapter are done for structural materials with different properties such as silicon, polysilicon as well as silicon nitride. These materials are used to cover a range of lower and higher material properties including density and Young's modulus, than silicon as the original material in microfabrication. In addition, in a CMUT-based gas sensor polymers are used as sensing materials to functionalize the device. Therefore, in this thesis, polyisobutylene (PIB) is employed as an example of the sensing material. However, the developed model remains valid for any other designed sensing polymer. PIB is used in gas sensing technology due to its sensitivity to a wide range of gases including dimethyl methyl phosphonate (DMMP) [102], tetrachloroethane (PCE) [103] and dichloromethane (DCM) [104]. Material properties of the employed structural materials and PIB are shown in Table 5.2.

In addition, in micro and nanofabrication technology the top membrane can be vacuum backed to effectively enhance the performance of the CMUT-based gas sensor [60].

Table 5.2: Material properties of Silicon, Polysilicon, Silicon Nitride and PIB.

Description	Silicon	Polysilicon	Silicon Nitride	PIB
Young's Module (E)(Gpa)	170	160	250	10
Density (ρ)(Kg/m^3)	2329	2320	3100	920
Relative Permittivity (ϵ)	11.7	4.5	9.7	2.2
Poisson's Ratio (ν)	0.28	0.22	0.23	0.48

The cavity between the top and the bottom membranes is, therefore, considered as vacuum in all of the FEA simulations.

5.3 Sensor Performance Evaluations and Simulation

Results of Bilayer Circular CMUT-Based Sensors

The proposed analytical model, presented in Chapter 4, is employed to design a circular bilayer CMUT-based gas sensor. This is followed by conducting FEA simulations using COMSOL Multiphysics, to further enhance the sensitivity of the device to low gas concentration. In this section, critical parameters of the device are investigated including radius, membrane thickness and cavity height in addition to the structural material properties. The simulations are conducted using COMSOL Multiphysics. Effects of the aforementioned critical parameters on the center resonant frequency are optimized for the frequency range between $5MHz$ to $25MHz$, as a sample of frequency range. However, the proposed analytical model in Chapter 4 remains valid for all other frequency ranges.

In this chapter, the analytical model analysis is also compared with the FEA simulations to evaluate the accuracy of the proposed analytical model.

5.3.1 Effect of the Radius

The CMUT radius is one of the critical parameters, which affects the center resonant frequency of the device. Radius effectively contributes to resonant frequency by influencing spring constant as can be deduced from Equation 4.25. In this equation, term 1, physical properties, and term 2, spring softening effect due to the applied DC bias voltage, are influenced by radius in the spring constant. Increasing the radius of the bilayer circular CMUT-based gas sensor results in a decrease in the term 1 of the stiffness, which is inversely proportional to the radius squared of the membrane. Moreover, increasing the

radius, affects term 2 by changing the area of the membrane. Therefore, the stiffness and consequently the center resonant frequency of the device decreases for larger radii. In this section, the effect of radius on the first six modes of the resonant frequency and frequency shift of the device is investigated by conducting FEA simulations using COMSOL Multiphysics. Eigenfrequency Prestressed analyses are performed for the radii ranging between $5\mu m$ and $30\mu m$ due to the sample target frequency range between $5MHz$ and $25MHz$. Properties for this device are presented in Table 5.3, however, the model remains valid for other device properties as well as the structural materials. In addition, displacement of the top membrane is also investigated using Stationary study in COMSOL Multiphysics for the device properties shown in Table 5.3.

Obtained simulation results indicate that adding sensing material to the conventional CMUT and transforming it to the bilayer circular CMUT-based gas sensor does not affect the mode shapes of center resonant frequency of the device, as shown in Figure 5.8. Therefore, the proposed analytical model in Chapter 4 as well as conducted FEA simulations remain valid while the radius is changed.

From the simulation results, it can be seen that by increasing the radius of the vibrating membrane, the center resonant frequency of the bilayer circular CMUT based gas sensor decreases as presented in Figure 5.9 (a). Larger radii make the vibrating membrane softer in response to the applied DC bias voltage than the smaller devices as can be seen from Equation 4.25. In addition, as shown in Figure 5.9 (b), smaller radii provide higher frequency shift, which can enhance the sensitivity of the bilayer circular CMUT-based gas

Table 5.3: Structural properties of the simulated devices to evaluate the effect of radius.

Radius (μm)	Top Membrane Thickness (nm)	PIB Thickness (nm)	Cavity (nm)	Structural Material	DC Bias Voltage (V)	PIB Density (Kg/m^3)
5, 7, 9, 15 20, 25, 30	500	300	500	Polysilicon	30	920

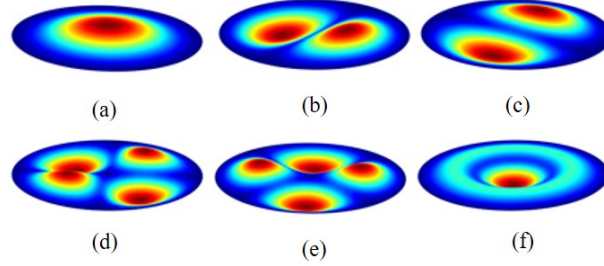


Figure 5.8: Conducted FEA simulations for (a) first, (b) second, (c) third, (d) forth, (e) fifth and (f) six modes of the resonant frequency of bilayer circular CMUT-based gas sensor with $5\mu\text{m}$ radius and 500nm polysilicon membrane, which is functionalized by 300nm PIB while biased with 30V DC and the cavity is defined 500nm .

sensor in response to the target gas absorption, as shown in Equation 5.1. Sensitivity is defined as frequency shift per unit mass change,

$$S = \frac{\Delta f}{\Delta m} \quad (5.1)$$

where Δf is frequency shift and Δm is mass change of the device.

By conducting COMSOL simulations in this thesis, the displacement of the membrane is also investigated using Stationary study in COMSOL Multiphysics, to stay below one

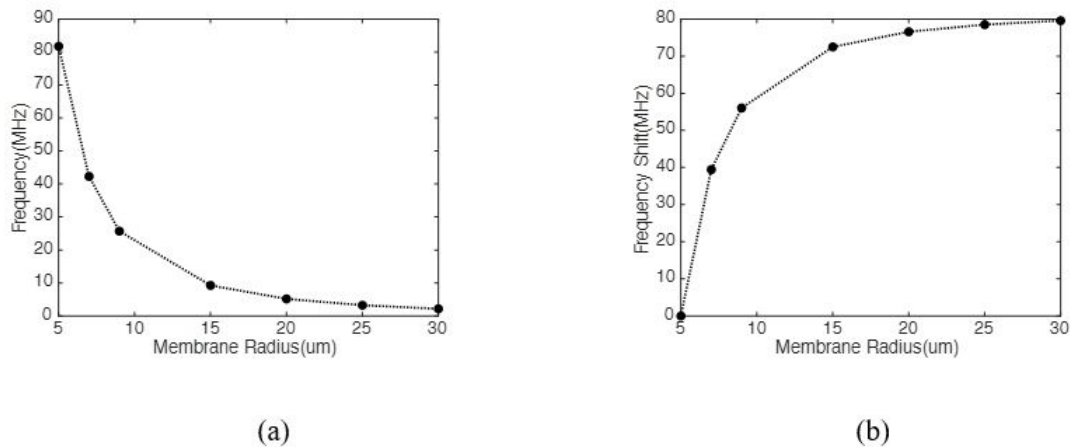


Figure 5.9: (a) Resonant frequency (MHz) vs radius (μm), and (b) frequency shift(MHz) vs. radius (μm) based on the resonant frequency of the device with radius $5\mu\text{m}$, for a 500nm polysilicon membrane, which is functionalized by 300nm PIB, while biased by 30V DC and the cavity is defined 500nm .

third of the cavity height, as shown in Equation 4.3, in order to avoid device collapse. Displacement increases for higher radii, as it is illustrated in Figure 5.10. Based on Equation 4.6 regarding membrane displacement, the maximum deflections occur at the center of the membrane and higher radii tend to deflect the membrane easier than the lower radii.

From the simulations, a displacement profile for the deflected membrane towards the bottom electrode is shown in Figure 5.11, which is simulated using COMSOL Multiphysics for a device with a $5\mu\text{m}$ radius, a 500nm polysilicon membrane, functionalized by 300nm PIB and biased by 30V DC, and a cavity defined at 500nm . Conducted simulations for total displacement of the membrane with the aforementioned properties is also shown in the Figure 5.12.

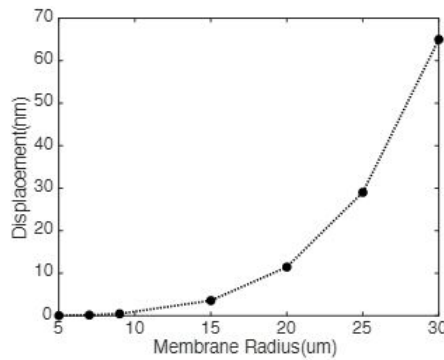


Figure 5.10: Membrane displacement (nm) vs. membrane radius (μm) for a 500nm polysilicon membrane, which is functionalized by 300nm PIB, while biased by 30V DC and the cavity is defined 500nm .

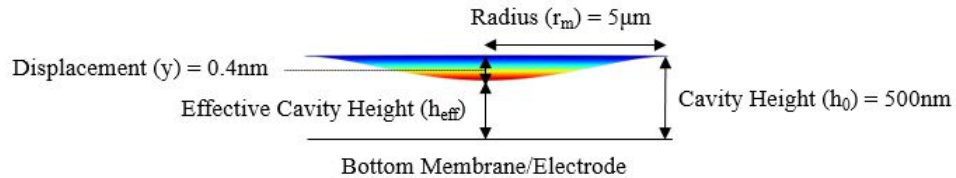


Figure 5.11: Membrane displacement profile for the radius $5\mu\text{m}$, 500nm polysilicon membrane, which is functionalized by 300nm PIB, while biased by 30V DC and the cavity is defined 500nm .

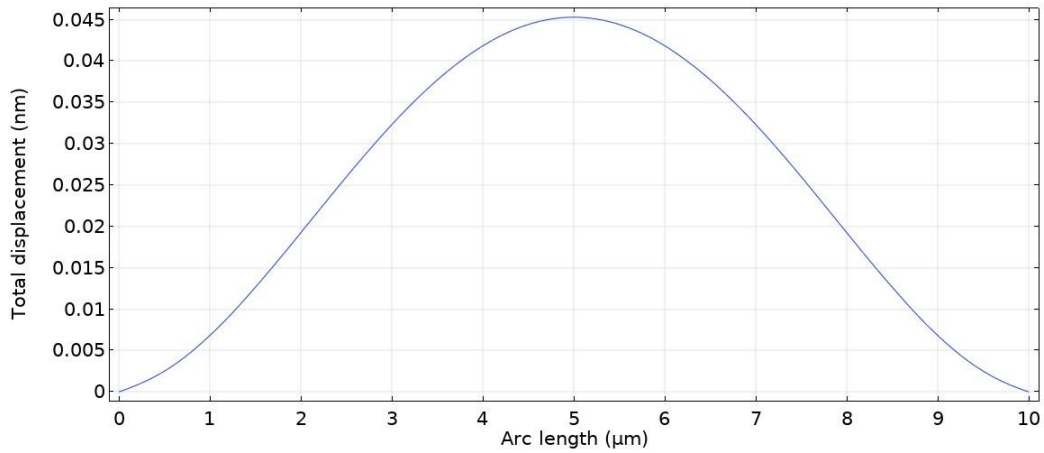


Figure 5.12: Total displacement of the membrane for a $5\mu\text{m}$ radius, 500nm polysilicon membrane, which is functionalized by 300nm PIB, while biased by 30V DC and the cavity is defined 500nm .

Based on the conducted FEA simulations in this thesis and the proposed analytical model in Chapter 4, the frequency shift of a bilayer circular CMUT-based gas sensor is immensely dependent on the radius.

5.3.2 Effect of the Membrane Thickness

The membrane thickness is one of the geometrical parameters which is further affecting the center resonant frequency of the bilayer circular CMUT-based gas sensor. Membrane thickness affects the parameters A , C as well as N , in the effective flexural rigidity remarkably, as shown in Equations 4.21 through 4.24. Effective flexural rigidity affects the term 1 of the stiffness, which is related to the membrane geometrical properties. Additionally, by increasing the thickness of a membrane residual stress increases as well. Therefore, thicker membranes provide higher membrane stiffness and consequently higher center resonant frequency of the device, as it is shown in Equation 4.25. In this section, effect of the membrane thickness is studied as a critical design parameter by employing COMSOL Multiphysics. In order to investigate it, FEA simulations are conducted for a polysilicon

membrane with properties shown in Table 5.4. Thickness ranging from $300nm$ to $1000nm$ is considered to stay in the target frequency range, $5MHz$ to $25MHz$, as a sample of the frequency.

In this section, the center resonant frequency, the frequency shift as well as the displacement of the membrane are investigated. Eigenfrequency Prestressed analyses are performed for the first six modes of the center resonant frequency of the devices with the aforementioned properties in Table 5.4. The circular bilayer CMUT-based gas sensor includes PIB as an example of the sensing material in the conducted FEA simulations. As illustrated in Figure 5.13, an added sensing material to the device does not affect shapes of frequency modes.

From the conducted simulations in this thesis illustrated in Figure 5.14 (a), it can be seen that by incrementing the thickness, the frequency of the circular bilayer CMUT-based gas sensor increases for the membrane thicknesses ranging between $300nm$ and $1000nm$.

Table 5.4: Structural properties of the simulated devices to evaluate effect of membrane thickness.

Radius (μm)	Top Membrane Thickness (nm)	PIB Thickness (nm)	Cavity (nm)	Structural Material	DC Bias Voltage (V)	PIB Density (Kg/m^3)
9	300, 500 800, 1000	200	150	Polysilicon	46	920

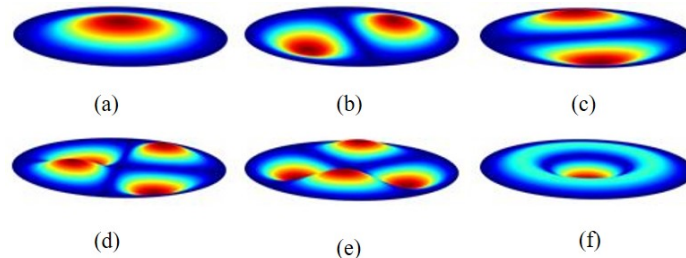


Figure 5.13: FEA simulations for the first six modes of frequency of a circular bilayer CMUT-based gas sensor, with $300nm$ polysilicon membrane functionalized by $200nm$ PIB, radius $9\mu m$, cavity $150nm$ while biased with 46 DC voltage.

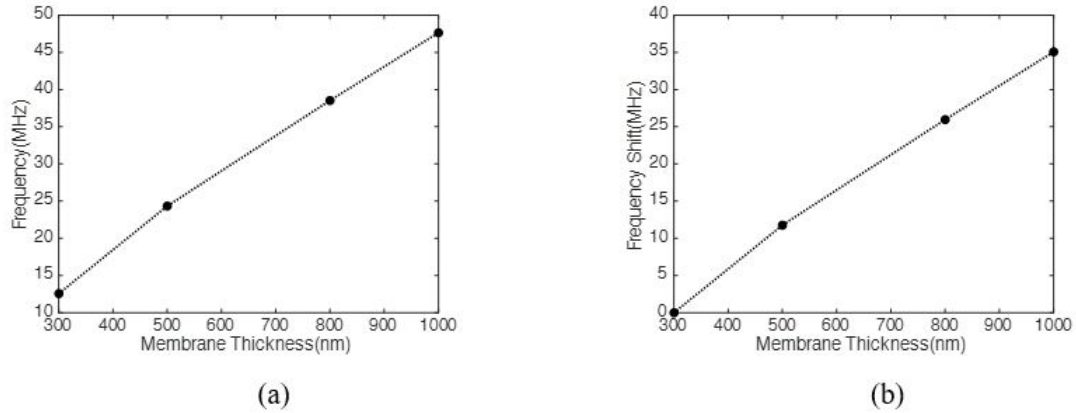


Figure 5.14: (a) Resonant frequency (MHz) vs. membrane thickness (nm) and (b) frequency shift (MHz) vs. membrane thickness (nm) where the reference resonant frequency belongs to a device with $300nm$ membrane thickness. Simulations are conducted for polysilicon membranes with $9\mu m$ radius, which are functionalized by $200nm$ PIB, while biased by 46 DC voltage and the cavity is defined $150nm$.

The raising in the resonant frequency is due to the higher stiffness of the thicker membranes, as shown by the stiffness equation, 4.25. From FEA simulations, the frequency shift for the circular bilayer CMUT-based gas sensor with the aforementioned properties in Table 5.4 increases, as illustrated in Figure 5.14 (b). In addition, the frequency has slightly a higher shift for the smaller thicknesses, which can improve the sensitivity of the circular bilayer CMUT-based gas sensor.

Furthermore, the displacement of the top membrane versus the membrane thickness for simulated bilayer circular CMUT-based gas sensors are shown in Figure 5.15.

Higher membrane thicknesses increase the effective flexural rigidity and consequently the term 1 of the stiffness in addition to the residual stress of the device. Therefore, thicker membranes have higher stiffness, which results in lower displacement when the same electrostatic force is applied.

Based on the conducted FEA simulations in this work, a deformation profile of a $9\mu m$ radius CMUT membrane is shown in Figure 5.16, which is simulated using COMSOL Multiphysics. The polysilicon membrane has $300nm$ thickness, which is functionalized

by 200nm PIB and biased with 46V DC when the cavity height is defined 150nm. Total displacement of the device is also shown in Figure 5.17.

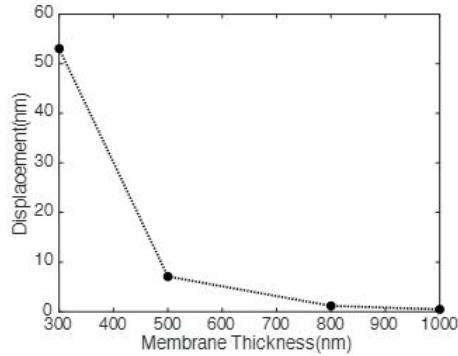


Figure 5.15: Displacement (nm) vs. membrane thickness (nm) for a polysilicon membrane with $9\mu\text{m}$ radius, which is functionalized by 200nm PIB, while biased by 46 DC voltage and the cavity is defined 150nm.

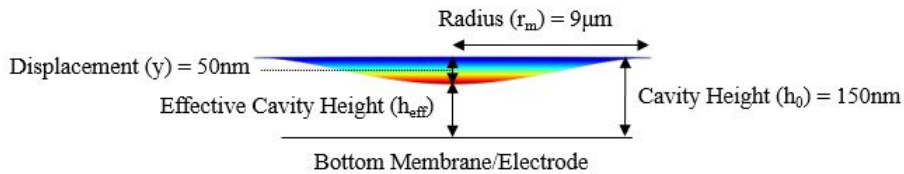


Figure 5.16: profile of the deflected polysilicon membrane for a structure with $9\mu\text{m}$ radius, which is functionalized by 200nm PIB, while biased by 46 DC voltage and the cavity is defined 150nm.

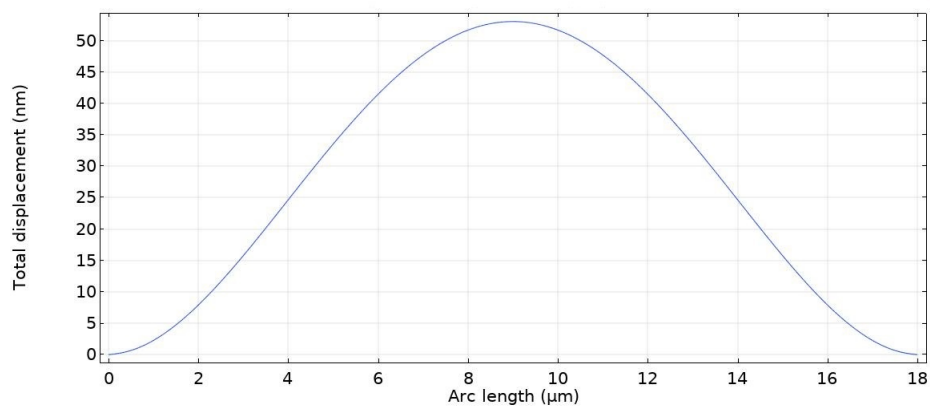


Figure 5.17: Total displacement of the bilayer circular CMUT-based gas sensor with $9\mu\text{m}$ radius, which is functionalized by 200nm PIB, while biased by 46 DC voltage and the cavity is defined 150nm.

As a result, evaluating bilayer circular CMUT-based gas sensors with the thicknesses ranging between 300nm and 1000nm illustrates that a smaller thickness contributes to higher frequencies.

5.3.3 Effect of the Cavity Height

The cavity height has a significant role in the static operation of the bilayer circular CMUT-based gas sensor at the equilibrium point. Based on Equation 4.8, the electrostatic force created across the larger cavities is smaller than the devices with lower gap between the electrode and membrane. Therefore, based on Equation 4.4, collapse voltage increases for larger cavities. Additionally, by increasing the cavity height, the term 2 of the membrane stiffness, which is softening effect due to the applied DC bias voltage, decreases. Therefore, a lower DC bias voltage makes the membrane stiffer, which results in higher frequencies. In this section, the effect of cavity height is evaluated for the first six modes of the resonant frequency of the circular bilayer CMUT-based gas sensors. In addition to the behavior of the frequency, frequency shift versus cavity height and the membrane displacement are investigated. FEA simulations are conducted using COMSOL Multiphysics for cavity heights ranging between 130nm and 500nm for a bilayer circular CMUT-based gas sensor with structural parameters as shown in Table 5.5.

The first six modes of the resonant frequency are shown in Figure 5.18 for a simulated device with 500nm polysilicon membrane and $9\mu\text{m}$ radius, which is functionalized by

Table 5.5: Structural properties of the simulated devices to evaluate the effect of cavity height.

Radius (μm)	Top Membrane Thickness (nm)	PIB Thickness (nm)	Cavity (nm)	Structural Material	DC Bias Voltage (V)	PIB Density (Kg/m^3)
9	500	100	130, 140, 150 250, 500	Polysilicon	30	920

100nm PIB when biased with 30V DC, and the cavity is defined at 130nm. Based on the conducted FEA simulations it can be seen that, in Figure 5.18, adding PIB as an example of the sensing material does not affect the mode shapes of the frequency.

From the simulations the frequency increases for larger cavities, as illustrated in Figure 5.19 (a). The slope of the plotted frequency versus cavity height in Figure 5.19 (a) shows that when the cavity height is smaller, the frequency increases faster in comparison to when the cavity heights are larger. As shown in Figure 5.19 (b), the frequency shift for the smaller cavity heights ranging between 130nm to 150nm shows higher increment, which can be involved in improving the sensitivity of the circular bilayer CMUT-based gas sensor.

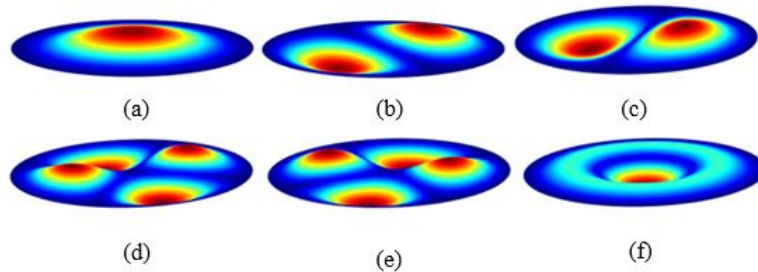


Figure 5.18: The first six frequency modes of conducted FEA simulations for a circular CMUT-based gas sensor, with 500nm polysilicon membrane functionalized by 100nm PIB, cavity height 130nm and radius 9μm, while biased with 30V DC.

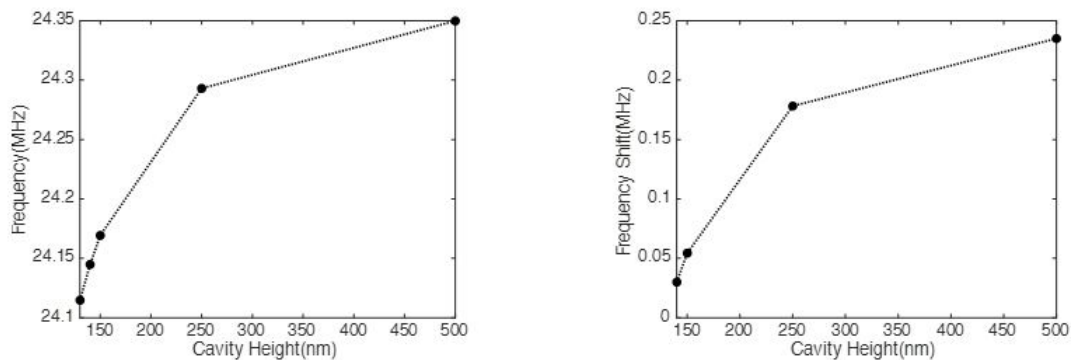


Figure 5.19: (a) Resonant frequency (MHz) vs. cavity height (nm) and (b) frequency shift (MHz) vs. cavity height (nm) when the reference resonant frequency belongs to the device with 130nm cavity height. FEA simulations are conducted for 500nm polysilicon membranes with 9μm radius, which are functionalized by 100nm PIB, while biased by 30 DC voltage.

In this section, the displacement of the membrane for different cavity heights is also investigated for the structure with aforementioned properties in Table 5.5. The achieved FEA simulation results are shown as illustrated in Figure 5.20, wherein, they confirm that the membrane displacement does not exceed one third of the cavity height, therefore, the device does not collapse, as shown in Equation 4.4. Additionally, Figure.5.20 explains that displacement of the membrane decreases rapidly by increasing the cavity height due to the smaller electrostatic force.

Based on the conducted FEA simulations in this thesis, a profile of the deformed 500nm polysilicon membrane is shown in Figure 5.21, which is functionalized by 100nm PIB, with a radius of $9\mu\text{m}$ and a cavity height of 130nm while a 30V DC is applied to the membrane. The simulated total displacement of the top membrane for the same device is also shown in Figure 5.22.

Since applying DC bias voltage forces the device to operate closer to the optimum point, therefore, the cavity height is an effective parameter which should be considered to avoid device collapse, as shown in Equation 4.4. Maximum membrane displacement should not exceed one third of the cavity height to avoid the device collapse, as illustrated in Equation 4.3.

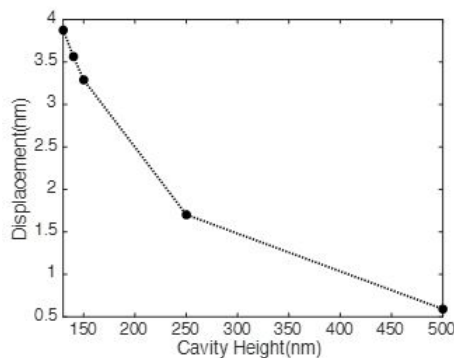


Figure 5.20: Displacement(*nm*) vs. cavity height(*nm*) for a 500*nm* polysilicon membrane with $9\mu\text{m}$ radius, which is functionalized by 100*nm* PIB, while biased by 30 DC voltage.

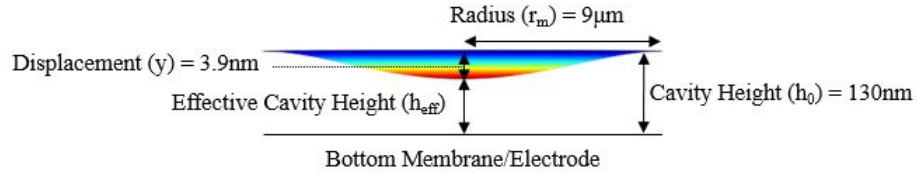


Figure 5.21: Membrane displacement profile for a 500nm polysilicon membrane with 9 μm radius, which is functionalized by 100nm PIB, while biased by 30V DC and the cavity height is defined 130nm.

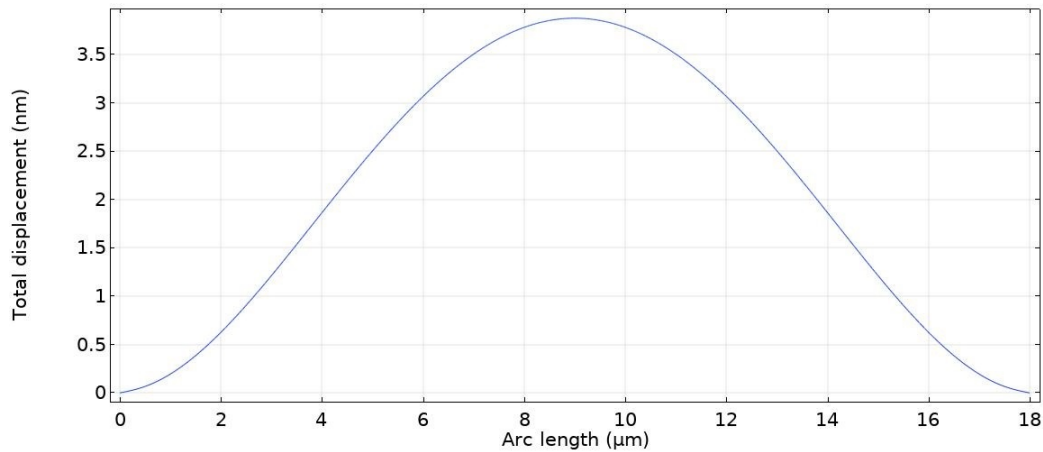


Figure 5.22: Total displacement of the device with 500nm polysilicon membrane with 9 μm radius, which is functionalized by 100nm PIB, while biased by 30V DC and the cavity height is defined 130nm.

5.3.4 Effect of the Structural Material

In order to design a bilayer circular CMUT-based gas sensor, the material properties of the top membrane play an important role in the center resonant frequency of the device. Elasticity, which is represented by the Young's modulus (E), the Poisson's ratio (ν) and the density (ρ) are effective material properties in the resonant frequency of the device. In this thesis, it is assumed that the material behaves as a linear elastic material, therefore, the simulations and the proposed comprehensive analytical model in Chapter 4 are valid when Equation 5.2 remains valid [105],

$$E = \frac{\sigma}{\varepsilon} \quad (5.2)$$

where ε is defined as strain of the structural material. The Young's modulus, E , represents the rigidity, which contributes to the effective flexural rigidity and consequently the resonant frequency and the displacement of the membrane as shown in Equations 4.22 through 4.24 as well as Equation 4.5. Poisson's ratio is the ratio of the transverse strain to the longitudinal strain of the material [106], which is defined as Equation 5.3,

$$\nu = \frac{\varepsilon_{trans}}{\varepsilon_{long}} \quad (5.3)$$

where ε_{trans} and ε_{long} represent the transverse and the longitudinal strains respectively. In this section, three common materials including silicon as reference in the micro and nanofabrication technology, polysilicon and silicon nitride, are investigated as the structural materials of the top membrane. The first six modes of the resonant frequency are simulated for the devices with the properties, as shown in Table 5.6 and the simulated profiles are shown in Figure 5.23.

As illustrated in Figure 5.23, conducted FEA simulations show that adding a sensing material to CMUT structure does not affect the shape of the first six frequency modes.

From the simulation results as presented in Figure 5.24, the frequency (a) and the frequency shift (b) are shown versus structural materials, silicon, polysilicon and silicon ni-

Table 5.6: Structural properties of the simulated devices to evaluate the effect of material properties.

Radius (μm)	Top Membrane Thickness (nm)	PIB Thickness (nm)	Cavity (nm)	Structural Material	DC Bias Voltage (V)	PIB Density (Kg/m^3)
9	500	100	140	Silicon, Polysilicon, Silicon Nitride	30	920

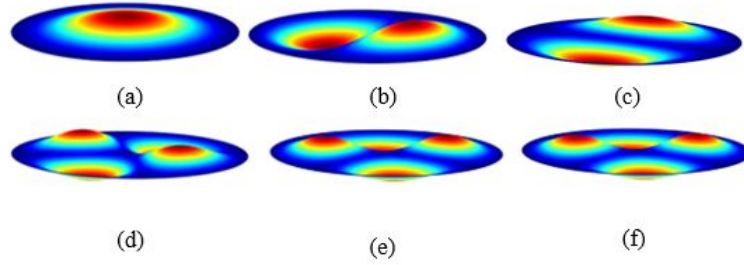


Figure 5.23: FEA simulations for (a) first, (b) second, (c) third, (d) fourth, (e) fifth and (f) sixth modes for a circular CMUT-based gas sensor, with 500nm silicon membrane functionalized by 200nm PIB, radius 9 μ m and 140nm cavity height while biased with 46 DC voltage.

tride, for a circular bilayer CMUT-based gas sensor. Simulations are conducted for a 500nm thickness of membrane, which is functionalized by 200nm PIB while radius and cavity are defined at 9 μ m and 140nm respectively and the applied DC bias voltage is 46V. Based on the material properties shown in Table 5.2 and Equations 4.21 through 4.24, a higher Young's modulus, E_m contributes to a higher flexural rigidity, De_{ff} , and consequently a higher resonant frequency of device. Therefore, more elastic materials provide higher resonant frequencies for a circular bilayer CMUT-based gas sensor. As shown in Figure 5.24 (b), the frequency shift increases for stiffer materials, which needs to be considered for sensitivity optimization based on target frequency range and sensor applications.

In order to investigate the effect of structural material on the device operation, the membrane's displacement is also studied for a bilayer circular CMUT-based gas sensor with a 500nm membrane thickness, which is functionalized with a 200nm PIB when the cavity is defined at 140nm and the membrane is biased with 46V DC. From the simulation results, it can be seen that silicon and silicon nitride membranes have higher displacement in comparison to polysilicon as presented in Figure 5.25. Based on the conducted studies in this section, the displacement of top membrane with different structural materials does not exceed one third of the initial gap, h_0 , as shown in Equation 4.4. Therefore, the device does not collapse.

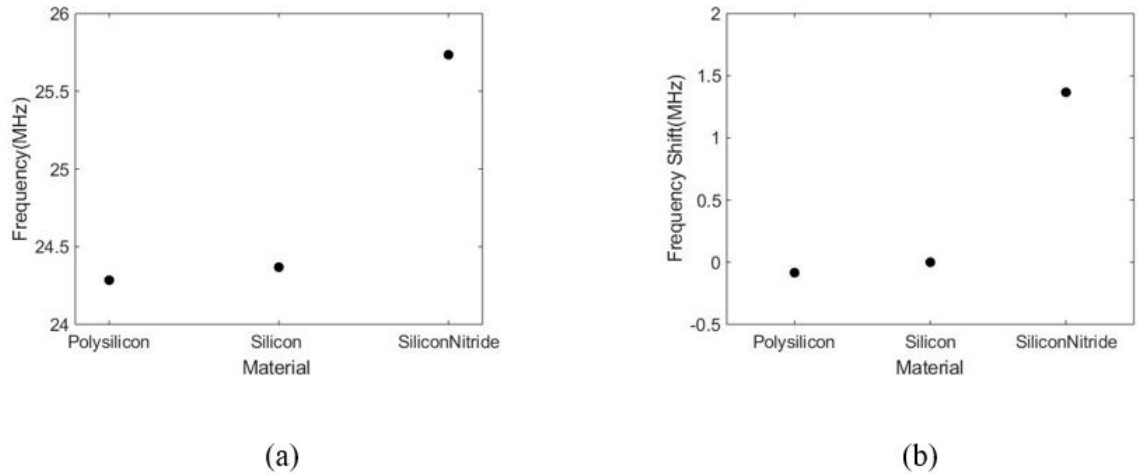


Figure 5.24: (a) Resonant frequency (MHz) vs. material and (b) frequency shift (MHz) vs. material where polysilicon is considered as the reference material for the frequency shift. FEA simulations are conducted for $500nm$ membranes, functionalized by $200nm$ PIB, $9\mu m$ radius and $140nm$ cavity height, while biased with $46V$ DC.

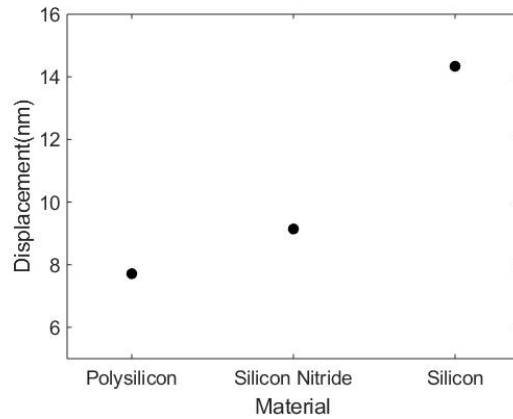


Figure 5.25: Displacement (nm) vs. material for a $500nm$ silicon membrane with $9\mu m$ radius, which is functionalized by $200nm$ PIB and $140nm$ cavity height while biased by $46V$ DC.

To investigate displacement of device, a stationary study has been conducted using COMSOL Multiphysics. Based on the conducted FEA simulations, a displacement profile is shown in Figure 5.26 for a $500nm$ silicon membrane with $9\mu m$ radius, $140nm$ cavity height while the membrane is functionalized by $200nm$ PIB and it is biased with $46V$ DC. The simulated total displacement of the device's membrane with aforementioned properties

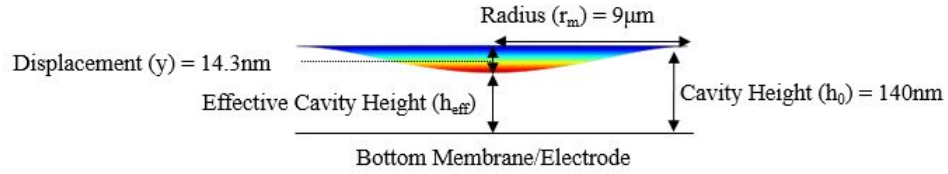


Figure 5.26: Displacement (nm) vs. material for a $500nm$ silicon membrane with $9\mu m$ radius, which is functionalized by $200nm$ PIB and $140nm$ cavity height while biased by $46V$ DC.

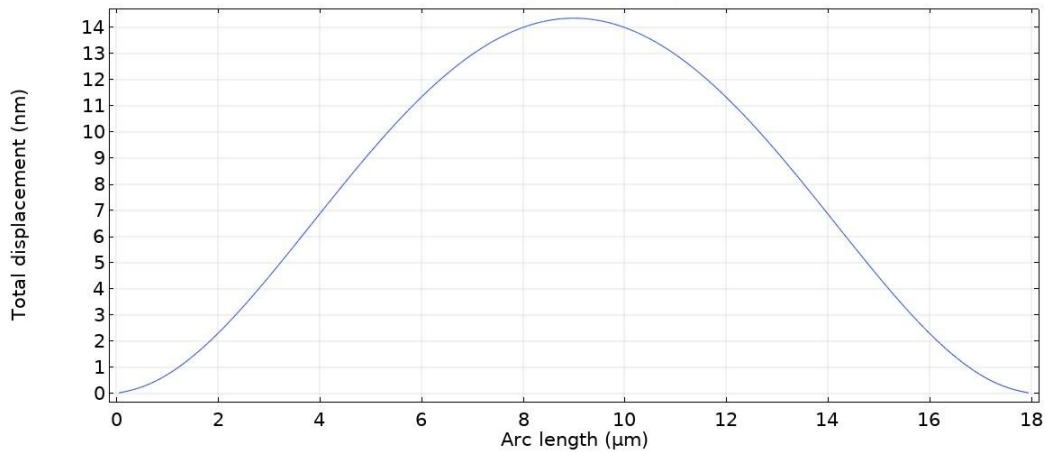


Figure 5.27: Total displacement for a bilayer circular CMUT-based gas sensor with $500nm$ functionalized silicon membrane with $200nm$ PIB, when the cavity is $140nm$ and $46V$ is applied as the bias voltage.

is shown in Figure 5.27.

According to the conducted FEA simulations in this chapter and the proposed analytical model in Chapter 4, the material properties of the top membrane including Young's modulus (E), Poisson's ratio (ν), relative permittivity (ϵ) and density (ρ) are all affecting the center resonant frequency of device. Stiffer structural materials including silicon nitride contribute to a higher resonant frequency whereas softer materials including polysilicon provide a lower center resonant frequency. In this thesis, the target frequency range is considered $5MHz$ to $25MHz$ as a sample range. Therefore, mainly silicon and polysilicon are chosen since they stay in the desired frequency range.

5.3.5 Influence of the Sensing Material Properties

In a circular bilayer CMUT-based gas sensor, the sensing material properties including mass and thickness changes in response to the target gas adsorption. This results in a shift in the center resonant frequency of the device. Therefore, an investigation on mass and thickness of the sensing material and their effects on the center resonant frequency is critical. Furthermore, it provides more information to evaluate the proposed analytical mode in Chapter 4 for a bilayer circular CMUT-based gas sensor. In this thesis, PIB is used as an example of the sensing material to conduct FEA simulations and evaluate the proposed analytical model. All the material properties of PIB are considered in the proposed model presented in Chapter 4 and conducted FEA simulations, including Young's modulus, Poisson's ratio, relative permittivity and density. Therefore, it can be replaced by a variety of sensing materials while the proposed model and method for conducting FEA simulations still stays valid.

5.3.5.1 Investigation on Sensing Material Mass Change

In the above sections, critical geometrical parameters are investigated for a circular bilayer CMUT-based gas sensor. However, in this section, change in mass of the sensing material is evaluated, since effective mass of the sensor changes due to exposure to the target gas. Change in the mass affects the center resonant frequency as shown in Equation 4.17, which can be correlated to the target gas adsorption. Density of the sensing material is investigated as the representative for mass of the sensing layer, while conducting FEA simulations using COMSOL Multiphysics. Sensing material mass affects the center resonant frequency of the device as shown in Equation 4.17. This means by increasing the mass of the sensing material, center resonant frequency of circular bilayer CMUT-based gas sensor decreases. In this section, change in density of device is investigated for silicon and polysil-

icon membranes with $9\mu\text{m}$ radius, while functionalized with different thicknesses of PIB as an example of the sensing material. The PIB density varies between 920 Kg/m^3 , which is the original density to 1840 Kg/m^3 . The geometrical properties of simulated devices in this section, are shown in Table 5.7.

In this thesis, the first six modes of the frequency are studied by conducting FEA simulations on bilayer circular CMUT-based gas sensors. The simulated profiles are shown in Figure 5.28 for a circular bilayer CMUT-based gas sensor with a $9\mu\text{m}$ radius, a 500nm functionalized silicon membrane with 50nm PIB while the cavity is 140nm and the membrane is biased with 46V DC. As illustrated in Figure 5.28, adding the sensing material to CMUT structure while its mass is changing does not affect shape of the vibration modes.

Table 5.7: Structural properties of the simulated devices to evaluate the sensing material mass change.

Radius (μm)	Top Membrane Thickness (nm)	PIB Thickness (nm)	Cavity (nm)	Structural Material	DC Bias Voltage (V)	PIB Density (Kg/m^3)
9	500	50	140	Silicon,	46	920, 1150, 1380
		100		Polysilicon		1610, 1840

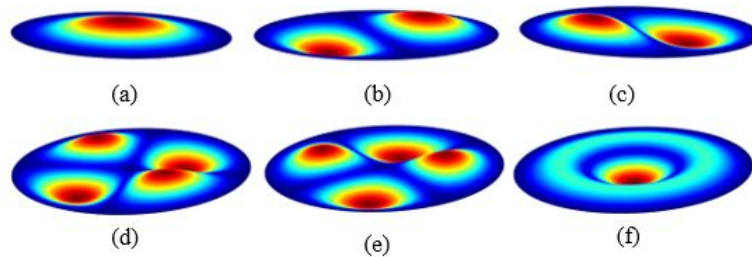


Figure 5.28: (a) First, (b) second, (c) third, (d) fourth, (e) fifth and (f) sixth modes of frequency for a bilayer circular CMUT-based gas sensor with $9\mu\text{m}$ radius, 500nm silicon membrane, which is functionalized by 50nm PIB, while cavity height is 140nm and biased with 46V DC.

From the simulations and as shown in Figure 5.29, by increasing sensing material's mass that represents gas molecule absorption phenomena, frequency of device reduces while frequency shift increases. Decline in the frequency versus sensing material density is due to higher effective mass of the device as shown in Equation 4.17. Additionally, the functionalized silicon membrane with a 50nm PIB, provides a higher frequency than the coated silicon membrane with a 100nm PIB. However, the functionalized polysilicon membrane with a 100nm PIB presents a lower frequency than the silicon membrane, which can be linked to the material properties. Based on the conducted FEA simulations, behavior of the frequency for functionalized silicon and polysilicon membranes with a 100nm PIB are parallel and very close, as shown in Figure 5.29 (a). Therefore, the frequency shift of the devices corresponds to each other as shown in Figure 5.29 (b). As a result, functionalizing either silicon or polysilicon with a 100nm PIB thickness have the same frequency shift due to their close material properties, which can result in close sensitivity.

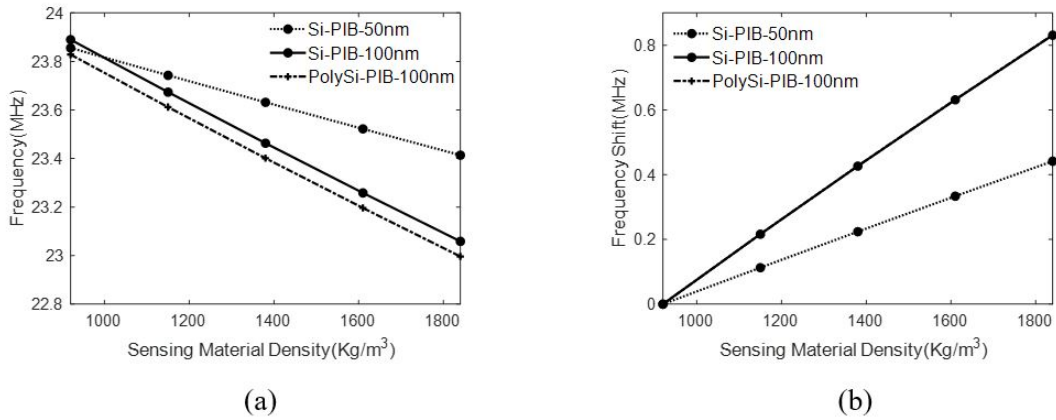


Figure 5.29: Frequency (MHz) vs. sensing material density (Kg/m³) (a) and frequency shift (MHz) (b) vs. sensing material density (Kg/m³) when the reference frequency belongs to sensing material with original density (920Kg/m³). FEA simulations are conducted for bilayer circular CMUT-based gas sensors with 9μm radius, 500nm thickness of the silicon and polysilicon membranes, coated by 50nm and 100nm PIB, 140nm cavity height while biased with 46V DC.

In addition to the center resonant frequency and the frequency shift of the device, displacement of the membrane is investigated in this section, in order to avoid device collapse. Conducted FEA simulations in this thesis present displacement for a functionalized $500nm$ silicon and a polysilicon membranes with $50nm$ and a $100nm$ PIB while the cavity height is $140nm$ and the top membrane is biased with $46V$ DC, as shown in Figure 5.30. Therefore, as illustrated in Equation 4.6, displacement of the top membrane does not change for different densities. However, FEA simulation results shown in Figure 5.30 present that the membrane's material properties and its thickness affect membrane displacement. Moreover, by comparing the achieved results for functionalized silicon and polysilicon with a $100nm$ PIB, the silicon provides higher displacement which is due to its material properties. Additionally, decreasing the PIB thickness for the device shown in Figure 5.30, with silicon membrane results in a higher displacement while the device is still stable and does not collapse. FEA simulations are conducted in this section to investigate the membrane displacement amplitude for silicon and polysilicon. It is shown that while the device is functionalized by different PIB thicknesses, displacement does not exceed one third of the initial cavity and consequently the device does not collapse.

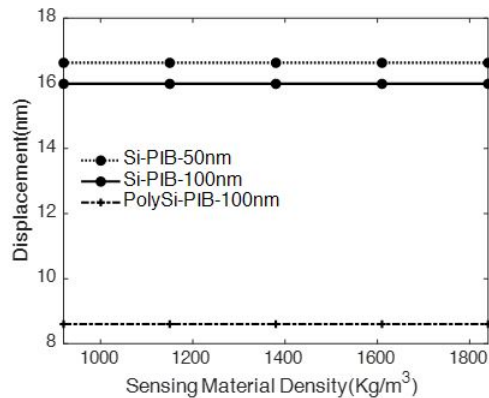


Figure 5.30: Displacement of the $500nm$ silicon and polysilicon membranes, which are functionalized by $50nm$ and $100nm$ while the cavity height is $140nm$ and the membrane is biased with $46V$ DC.

In Figure 5.31, displacement profile of one of the simulated devices in COMSOL Multiphysics is shown. The bilayer circular CMUT-based gas sensor has 500nm silicon membrane, which is functionalized by 50nm PIB while the radius and the cavity height are 9μm and 140nm respectively. The device is biased with a 46V DC. Total displacement of the device is also shown in the Figure 5.32.

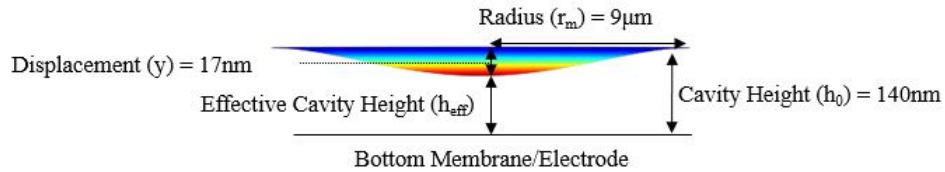


Figure 5.31: The displacement profile of 500nm silicon membrane for a simulated circular CMUT-based gas sensor with 9μm radius, 140nm cavity height while biased with 46V DC.

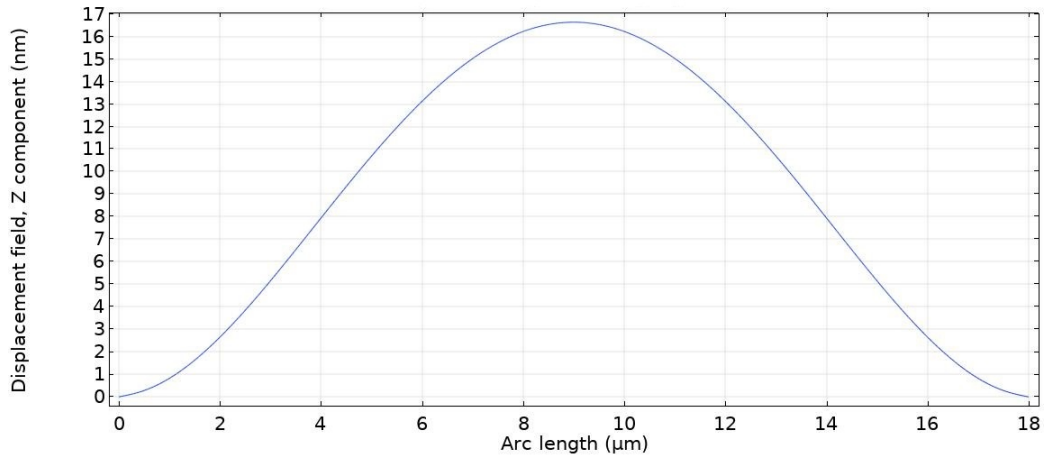


Figure 5.32: Total displacement of 500nm silicon membrane for a simulated circular CMUT-based gas sensor with 9μm radius, 140nm cavity height, biased with 46V DC.

5.3.5.2 Investigation on Sensing Material Thickness Change

In a circular bilayer CMUT-based gas sensor, by exposing the sensing material to the target gas, the properties of sensing material change in response to the target gas adsorption. One

of the critical parameters which can be affected is the sensing material thickness. Adsorbing the target gas can cause swelling in the sensing material depending on its properties. Based on conducted FEA simulations and the proposed analytical model in this thesis, changes in mass and thickness of the sensing material have similar effects on the resonant frequency of the device. As a result, the thickness of the material does not counteract the effect of the mass change and instead they both act together to strengthen the resonant frequency. In this section, FEA simulations results are presented for devices mentioned in Table 5.8.

First six modes of resonant frequency are studied and shown in Figure 5.33. The vibration modes are not changed while thickness of the sensing layer altered due to the gas adsorption. Increasing the sensing material thickness increases the effective flexural rigidity, D_{eff} , of the device as shown in Equations 4.21 through 4.24.

Table 5.8: Structural properties of the simulated devices to evaluate sensing material thickness change.

Radius (μm)	Top Membrane Thickness (nm)	PIB Thickness (nm)	Cavity (nm)	Structural Material	DC Bias Voltage (V)	PIB Density (Kg/m^3)
9	500	100, 120, 140 160, 180, 200	140	Silicon, Polysilicon	46	920

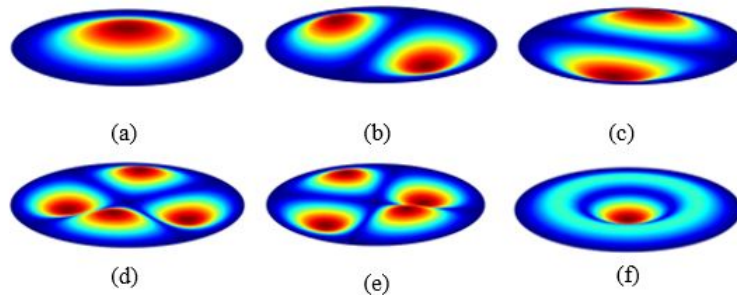


Figure 5.33: (a) first, (b) second, (c) third, (d) fourth, (e) fifth and (f) sixth modes of frequency, simulated in COMSOL for a 500nm silicon membrane with radius 9 μm and cavity height 140nm. The membrane is functionalized by 100nm PIB while 46V DC is applied.

Additionally, a thicker sensing material contributes in stiffening the membrane as shown in term 3 of Equation 4.25, stiffening effect due to the residual stress. Consequently, if the sensing material swells in response to target gas adsorption, the center resonant frequency increases, as shown in Figure 5.34 (a), based on the FEA simulations. The results in Figure 5.34 are shown for 500nm silicon and polysilicon membranes, which are functionalized by 100nm PIB, with 9 μ m radius while the cavity is defined 140nm and 46V DC is applied. Frequency shift of the circular bilayer CMUT-based gas sensor also increases for higher sensing material thicknesses as shown in Figure 5.34 (b).

Displacement of the aforementioned device in Table 5.8 is also measured by stationary simulations in COMSOL Multiphysics to stay below one third of cavity height, in order to avoid device collapse. As shown in Figure 5.35, the displacement for a silicon membrane is higher than the polysilicon membrane, which is due to their different material properties, based on Equation 4.6. Considering the proposed results in Figure 5.35, the membrane deflection is lower than one third of the initial cavity height.

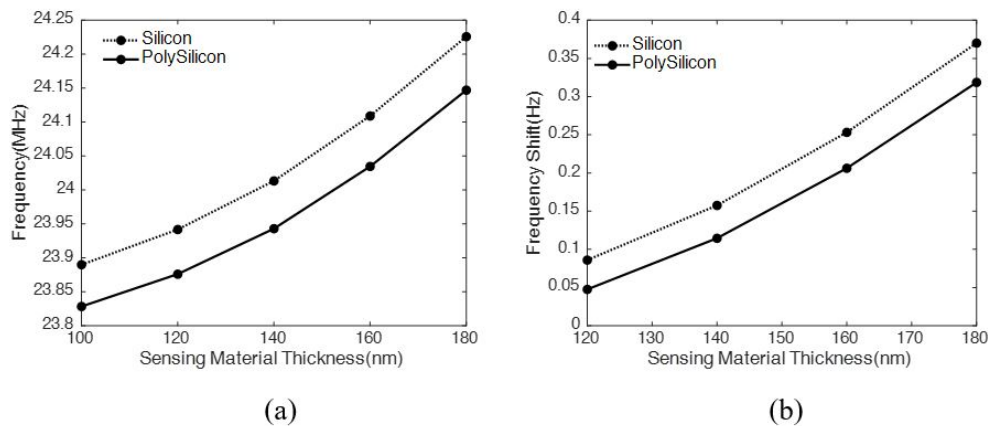


Figure 5.34: Frequency (MHz) vs. sensing material thickness(nm), (a) and frequency shift (MHz) (b) vs. sensing material thickness(nm) where the structure with 120nm is considered for the reference frequency. FEA simulations are conducted in COMSOL for 500nm silicon and polysilicon membranes with radius 9 μ m and cavity height 140nm. The membrane is functionalized by 100nm PIB while 46V DC is applied.

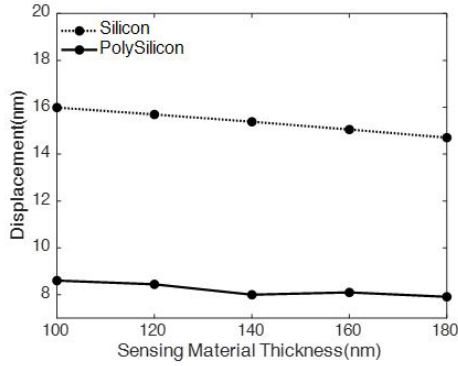


Figure 5.35: Displacement (*nm*) vs. sensing material thickness, simulated in COMSOL for a 500*nm* silicon and polysilicon membranes with radius 9 μm and cavity height 140*nm*. The membrane is functionalized by 100*nm* PIB while 46*V* DC is applied.

Therefore, the device does not collapse while sensing material’s thickness is changing due to the swelling after target gas adsorption.

A simulated displacement profile of the device with 500*nm* silicon and polysilicon membranes is shown in Figure 5.36. Displacement simulations are conducted using COMSOL Multiphysics for functionalized membranes with 100*nm* PIB while it is biased with 46*V* DC and the cavity is defined at 140*nm*. By conducting FEA simulations, as shown in Figure 5.36 that the maximum displacement occurs at the center of the membrane, which is 16*nm*. Total displacement of the silicon membrane is also shown in Figure 5.37, which confirms that the membrane deflects less than one third of the cavity, therefore, it does not collapse.

As a result, and based on the conducted FEA simulations in this section as well as

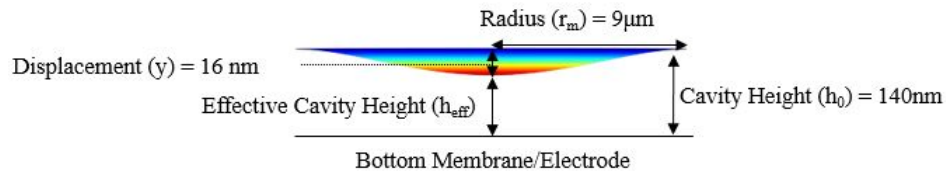


Figure 5.36: The displacement profile of a 500*nm* silicon membrane with radius 9 μm and cavity height 140*nm*. The membrane is functionalized by 100*nm* PIB while 46*V* DC is applied.

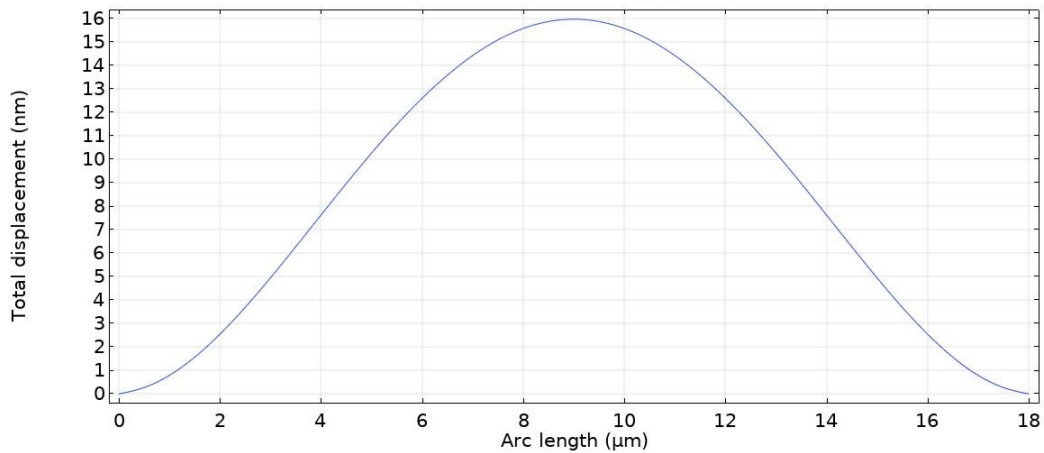


Figure 5.37: Total displacement of a 500nm silicon membrane with radius $9\mu\text{m}$ and cavity height 140nm . The membrane is functionalized by 100nm PIB while 46V DC is applied.

the proposed model in Chapter 4, the change in thickness of the sensing material affects the resonant frequency of device. A silicon membrane provides a slightly higher resonant frequency than that of a polysilicon membrane, which is due to its different material properties. Furthermore, a higher frequency shift belongs to silicon membrane, which can affect the sensitivity of the circular bilayer CMUT-based gas sensor as will be discussed in Section 5.5.

5.4 Comparison Between the Proposed Analytical Model and Conducted FEA Simulations

The proposed analytical model presented in Chapter 4, has been developed by employing critical design parameters including structural and sensing material properties, radius, membrane thickness, cavity height as well as residual stresses of deflectable membrane and sensing layer. The aforementioned parameters affect spring constant and consequently, center resonant frequency of circular bilayer CMUT-based gas sensor. Therefore, the proposed comprehensive model is developed for the first time, to provide information about

frequency based on different critical parameters. FEA simulations are further conducted as shown in section 5.3 to enhance the sensitivity of circular bilayer CMUT-based gas sensor. In this section, effect of the critical parameters on center resonant frequency of device is compared for conducted FEA simulations and the proposed analytical model in Chapter 4. In Figure 5.38, the graph of frequency versus radius is shown for a device with 500nm polysilicon membrane, which is functionalized by a 300nm PIB with 500nm cavity height where a 30V DC is applied ©2019 IEEE. The achieved results by the proposed comprehensive analytical model, in addition to the conducted FEA simulation results are shown in Figure 5.38 for radii ranging 5μm to 30μm. By comparing the results, the average variation between the proposed model and the conducted FEA simulations is less than 3%.

In Figure 5.39, the graph of frequency versus membrane thickness is shown for 9μm radius polysilicon membrane. The membrane is functionalized by a 200nm PIB while cavity is defined at 150nm and the membrane is excited with 46V DC. The results for the proposed analytical model are compared with conducted FEA simulations in Figure 5.39, which shows less than 1% average variation.

The proposed analytical model and the conducted FEA simulations are compared in

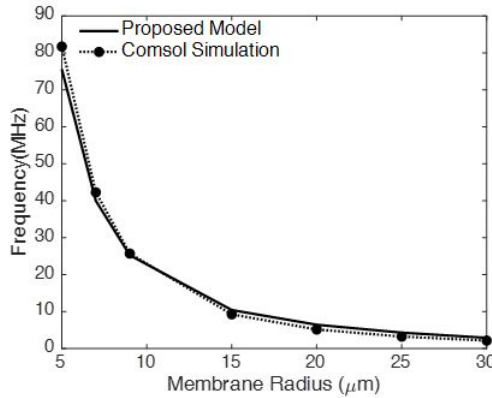


Figure 5.38: Resonant frequency vs. membrane radius for a structure with 500nm polysilicon top membrane and cavity height, which is functionalized by 300nm PIB while 30V DC is applied.

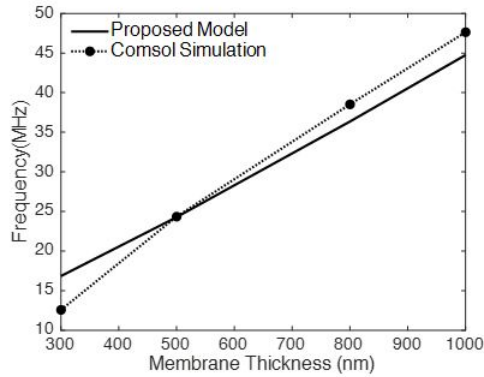


Figure 5.39: Resonant frequency vs. membrane thickness for a structure with $9\mu\text{m}$ radius, polysilicon membrane and 200nm PIB thickness as well as 150nm cavity height, which is excited by 46V as the applied DC bias voltage.

Figure 5.40 where they predict center resonant frequency of device versus different cavity heights. The comparison shown in Figure 5.40 is conducted for a device with a 500nm polysilicon membrane and $9\mu\text{m}$ radius, while a 30V DC is applied to the membrane©2019 IEEE. Based on Equation 4.9, the model needs to incorporate cavity height, which creates a capacitor between the top and the bottom electrode, in order to accurately present the sensor sensitivity. Consequently, in the proposed model, the effective cavity height has also been employed to optimize the CMUT gas sensor sensitivity. The average variation between the presented FEA simulations and the proposed model in Figure 5.40 is less than 1%.

In Figure 5.41, the devices' frequencies using different structural materials have been shown in addition to the comparison with FEA simulation results. The results are shown for a device with a $9\mu\text{m}$ radius and a 500nm membrane, while the cavity is at 140nm and a 30V DC is applied. The device is functionalized with a 200nm PIB as the sensing material. Average variation between the proposed analytical model and the conducted FEA simulations in frequency prediction versus material is approximately 5%.

Since the mass of the sensing material in a CMUT sensor changes by exposing to target gas, the proposed model is employed to predict resonant frequency for mass changes in

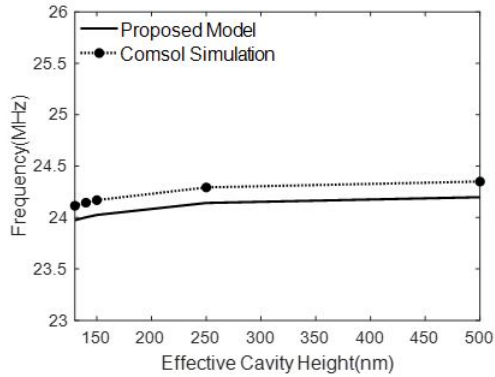


Figure 5.40: Resonant frequency vs. cavity height for a structure with $9\mu\text{m}$ radius, 500nm thickness polysilicon membrane and 30V applied DC voltage.

Figure 5.42 ©2019 IEEE. In addition, the conducted FEA simulation results are presented in Figure 5.42 to be compared with the proposed model. This comparison is shown in Figure 5.42 for a circular bilayer CMUT-based gas sensor with a $9\mu\text{m}$ radius and a 500nm polysilicon membrane, which is functionalized by a 100nm PIB, while the cavity height is set at 140nm and the membrane is biased by 30V DC. Average variation between the conducted FEA simulations and the proposed model in predicting resonant frequency versus sensing material mass change is less than 1%.

Frequency versus PIB thickness is shown in Figure 5.43 based on conducted FEA sim-

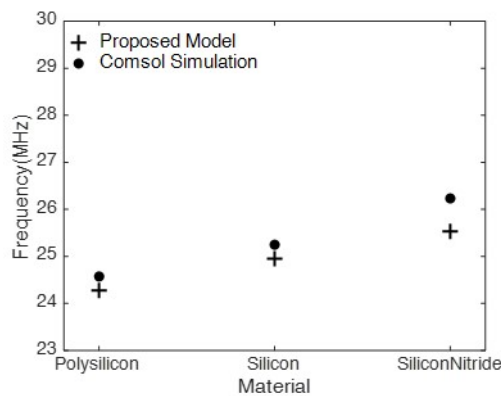


Figure 5.41: Resonant frequency vs. material for a structure with $9\mu\text{m}$ radius, 500nm top membrane thickness and 200nm PIB thickness as well as 140nm cavity height, which is excited by 30V as the applied DC bias voltage.

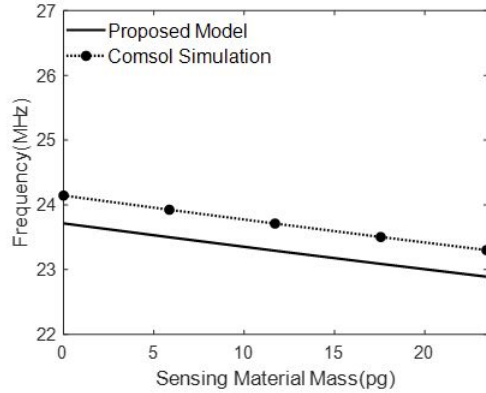


Figure 5.42: Resonant frequency prediction vs. sensing material mass for a structure with $9\mu\text{m}$ radius, 500nm polysilicon membrane, 140nm cavity height, which is functionalized by 100nm PIB and 30V as the applied DC bias voltage.

ulations for a circular bilayer CMUT-based gas sensor. The device has $9\mu\text{m}$ radius with 500nm silicon membrane while the cavity is 140nm and the device is biased with 46V DC. In Figure 5.43, the proposed analytical model is also shown to be compared to the conducted FEA simulations. Average variation between the conducted FEA simulations in this chapter and the propose analytical model in Chapter 4 is less than 1%.

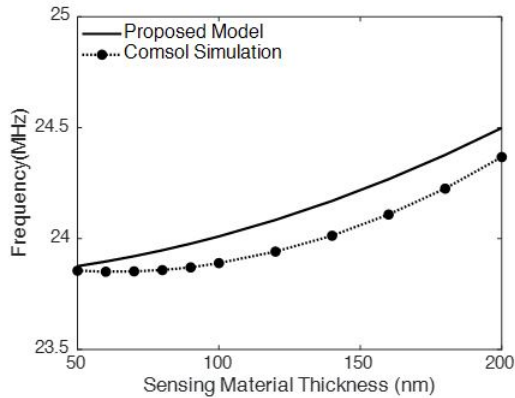


Figure 5.43: Resonant frequency prediction vs. sensing material thickness for a structure with $9\mu\text{m}$ radius, 500nm silicon membrane, 140nm cavity height, which is functionalized by PIB and biased with 46V DC.

5.5 Sensitivity Evaluation

In this thesis and in an unconventional approach, CMUT structure operates as a mass resonant sensor. Conventional CMUT structure is functionalized by a sensing material, which adsorbs target gas molecules when it is exposed to it. Change in effective mass of the device results in a shift in center resonant frequency. Since this application is new, there was no analytical model to predict center resonant frequency of device until the comprehensive analytical model is proposed in this thesis. FEA simulations were further conducted, which are presented in Section 5.3 and compared with the proposed analytical model, presented in Section 5.4. In this section, conducted FEA simulations for critical design parameters are used to optimize sensitivity of device for low gas concentration detection, which as shown in Equation 5.1, is defined as frequency shift per unit mass change. Therefore, FEA simulations are conducted to investigate effect of radius on sensitivity of device, as illustrated in Figure 5.44. The evaluation is done for devices with $500nm$ polysilicon membrane, functionalized by $300nm$ PIB as a sensing material for radii ranging between $7\mu m$ and $30\mu m$. The devices are biased with $30V$ DC when the cavity height is defined $500nm$. As shown in Figure 5.44, circular bilayer CMUT-based gas sensor with smaller radius has higher sensitivity to mass. Based on the conducted simulations maximum achieved sensitivity is $222Hz/zg$ for the device with $9\mu m$ radius in a sample frequency range between $5MHz$ and $25MHz$. This device consists of a $500nm$ polysilicon membrane, functionalized with a $300nm$ PIB when the cavity is at $500nm$.

Sensitivity versus membrane thickness is evaluated by conducting FEA simulations, as shown in Figure 5.45. It is illustrated that by increasing the membrane thickness, the sensitivity of the bilayer circular CMUT-based gas sensor is decreasing. Therefore, a thinner membrane which has a lower mass, provides higher sensitivity to mass in the gas sensing application.

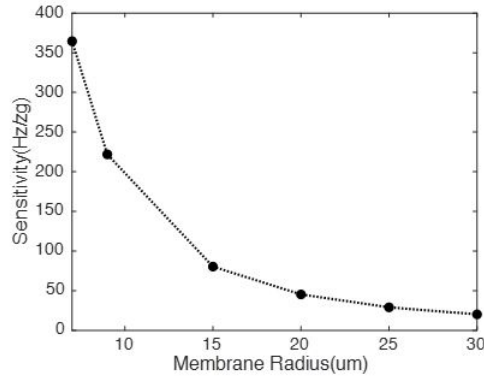


Figure 5.44: Sensitivity (Hz/zg) vs. membrane radius (μm) for a $500nm$ polysilicon membrane, which is functionalized by $300nm$ PIB while biased by $30V$ DC and the cavity is defined $500nm$.

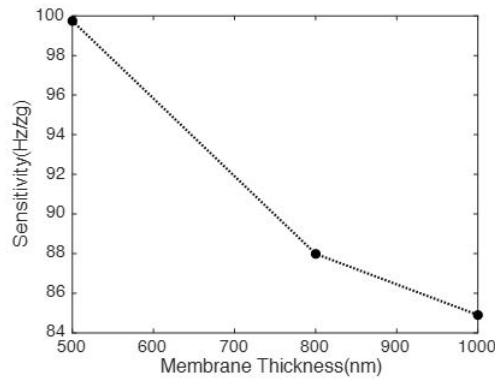


Figure 5.45: Sensitivity (Hz/zg) vs. membrane thickness (nm) for a polysilicon membrane with $9\mu m$ radius, which is functionalized by $200nm$ PIB, while biased by 46 DC voltage and the cavity is defined $150nm$.

In micro and nano fabrication technology, silicon is extensively used as wafer and also structural material. Therefore, in order to evaluate effect of structural material on sensitivity of a circular bilayer CMUT-based gas sensor, silicon is considered as the reference while polysilicon and silicon nitride are compared with it. FEA simulations are conducted for devices with $500nm$ membrane thickness, which are functionalized with $200nm$ PIB's while the radius and the cavity are set at $9\mu m$ and $140nm$ respectively. The devices are biased with a $46V$ DC. As illustrated in Figure 5.46, polysilicon provides higher sensitivity to mass in comparison to silicon nitride. This is correlated to its material properties and its lower

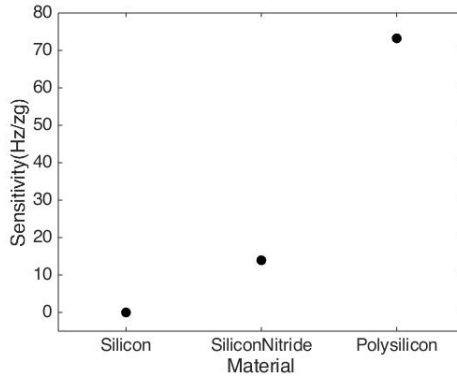


Figure 5.46: Sensitivity (Hz/zg) vs. material for a $500nm$ membrane, functionalized by $200nm$ PIB, $9\mu m$ radius and $140nm$ cavity height, while biased with $46V$ DC.

density.

As discussed in section 5.3.5.1, the sensing material properties can change while it is exposed to a target gas. The thickness and the mass of the sensing material are two of parameters which can be affected during sensing procedure. The change in the mass and the thickness of the sensing material does not counteract their effects on the center resonant frequency, but instead they strengthen each other. In Figure 5.47, sensitivity of the device is shown versus the sensing material density for a device with a $9\mu m$ radius, a $500nm$ membrane thickness, when cavity is defined at $140nm$. The device is functionalized by $50nm$ and $100nm$ PIB. As shown in Figure 5.47, when the sensing material's mass changes due to higher gas adsorption, sensitivity decreases, which is correlated to the higher mass of the membrane. It is also illustrated that the functionalized silicon membrane with a $50nm$ PIB as an example of the sensing material provides a higher sensitivity in comparison to a functionalized silicon membrane with $100nm$ PIB. In addition, the sensitivity of the functionalized silicon and polysilicon membranes with $100nm$ PIB, are almost equal. Therefore, a lighter sensing material, which results in a lower effective membrane's mass, associates with a higher sensitivity of device.

As a result, a smaller initial thickness of the sensing material provides a bilayer circular CMUT-based gas sensor with a higher sensitivity to the mass change. Moreover, the effect

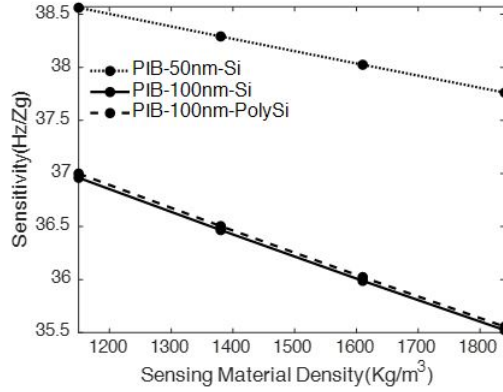


Figure 5.47: Sensitivity(Hz/zg) vs. sensing material density(Kg/m^3) for a bilayer circular CMUT-based gas sensor with $9\mu m$ radius, $500nm$ thickness of the silicon and polysilicon membranes, which are functionalized by $50nm$ and $100nm$ PIB, with $140nm$ cavity height while biased with $46V$ DC.

of sensing material's properties on the sensitivity of the device is dominated by its initial thickness. In addition to the sensing material's mass, effect of its thickness is also evaluated on the sensitivity of device, as shown in Figure 5.48. Simulations are conducted for a device with $500nm$ silicon and polysilicon membranes, functionalized with $100nm$ PIB, while the cavity is defined at $140nm$ and $46V$ DC is applied.

As illustrated in Figure 5.48, polysilicon membrane provides a higher sensitivity in

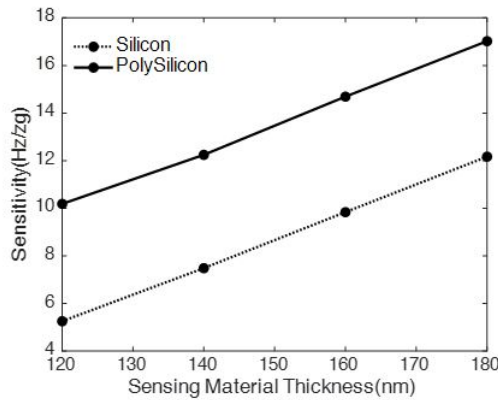


Figure 5.48: Sensitivity (MHz/zg) vs. sensing material thickness, simulated in COMSOL for a $500nm$ silicon and polysilicon membranes with radius $9\mu m$ and cavity height $140nm$. The membrane is functionalized by $100nm$ PIB while $46V$ DC is applied.

comparison to silicon, which is correlated to the lower material density. By combining the obtained results in evaluating the effect of radius, membrane thickness and material on the sensitivity of a bilayer circular CMUT-based gas sensor, a smaller radius and thickness for a polysilicon membrane provides higher sensitivity. In this thesis and by considering the sample frequency range between $5MHz$ and $25MHz$, the proposed bilayer circular CMUT-based gas sensor comprises $9\mu m$ radius, $500nm$ polysilicon membrane with a $500nm$ cavity height while biased with $46V$ DC.

5.6 Conclusions

In this chapter, critical design parameters of a circular bilayer CMUT-based gas sensor are investigated using COMSOL Multiphysics. Eigenfrequency Prestressed and Stationary studies are conducted to evaluate effects of critical parameters on center resonant frequency and deflection of the top membrane in order to avoid device collapse. These critical parameters include radius, membrane thickness, cavity height, structural material as well as thickness and mass of sensing layer. In this chapter, PIB is used as an example of the sensing material to conduct FEA simulations and analyze performance of the circular bilayer CMUT-based gas sensor. As a result, and based on the conducted FEA simulations in this chapter, smaller radii, thinner thickness of membrane and lighter structural material, effectively, contribute in providing a sensitive CMUT-based gas sensor. Moreover, the achieved results using the proposed analytical model is compared with the obtained results of conducted FEA simulations. Maximum average variation between the proposed comprehensive analytical model and conducted FEA simulations is 5% . According to the achieved results, maximum obtained sensitivity in this chapter for a sample frequency range between $5MHz$ and $25MHz$ is $222 Hz/zg$ for a device with $9\mu m$ radius, $500nm$ polysilicon membrane, which is functionalized by $300nm$ PIB. The device is biased with $30V$ DC while the

cavity height is defined $500nm$. In order to fabricate the proposed device, micro fabrication techniques should be employed which have better control on forming a thinner membrane while providing high performance and quality factor, as discussed in section 2.7. Therefore, details of the proposed fabrication process for the designed device using advanced micro and nano fabrication technology is presented in Chapter 6. These fabrication techniques are chosen in order to provide a device with enhanced sensitivity.

Chapter 6: Proposed Fabrication Steps for the CMUT-Based Gas Sensor with Enhanced Sensitivity

6.1 Introduction

In a CMUT-based gas sensor there are various critical parameters in micro and nano scale, which need to be considered in the design as well as fabrication processes and feasibility. These critical parameters are radius, membrane thickness, cavity height, structural and sensing material properties as well as residual stresses of the top membrane and sensing layer. The aforementioned parameters are effectively involved in sensor's performance and device's sensitivity, which also should be considered in the fabrication feasibility. As discussed in chapter 5, thinner and lighter membrane of a CMUT-based gas sensor as well as smaller radii contribute in more sensitive devices, due to the lower involved effective mass [68]. Therefore, appropriate micro fabrication techniques need to be employed to fabricate the proposed CMUT-based gas sensor in Chapter 5, which has relatively thin membrane and small dimensions. As discussed in Chapter 3, sacrificial technique is the conventional process for CMUT fabrication, An SEM image of the fabricated CMUT in this thesis using sacrificial technique is shown in Figure 6.1.

However, based on the review conducted in Chapter 3, wafer fusion bonding is preferred to fabricate CMUT-based gas sensors due to the more controllable processes and the absence of releasing holes on the top surface. In addition, efficiency of CMUT-based gas

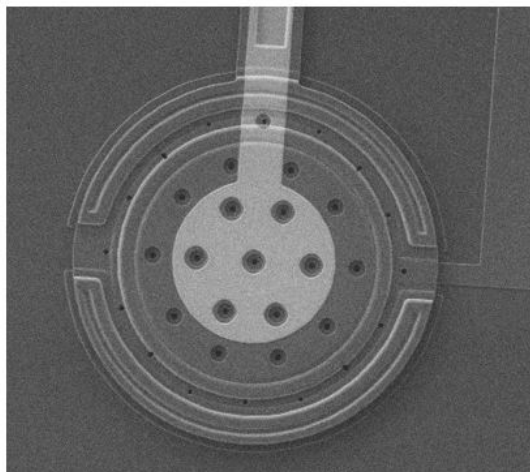


Figure 6.1: SEM image for a fabricated CMUT using sacrificial technique (POLY-MUMPs), chip IMUWR001.

sensors fabricated by wafer bonding technique has been reported higher than the devices fabricated by the sacrificial technique, as discussed in Chapter 3 [107]. This is due to optimization feasibility of top membrane and cavity using different substrates. Moreover, in the sacrificial fabrication process and at the stage of functionalizing the device with sensing material, coated polymer may reach bottom membrane through the releasing holes. This, consequently, damps the device deflection and decreases CMUT performance. Therefore, in this chapter wafer fusion bonding is employed to fabricate the proposed sensitive device in section 5.5 and details of fabrication steps are proposed. In addition to the sensitivity, selectivity is a critical component for sensory performances, which can be addressed by using advanced microfabrication technology, wherein, individual CMUT cells can be configured in an array format [108]. In this work and in order to use CMUT configuration as a gas sensor, the top membrane is functionalized by PIB using inkjet dispensing.

Table 6.1: Physical properties of the proposed CMUT for fabrication. Radius of the structure is $9\ \mu\text{m}$.

Layer	Material	Thickness (nm)
Substrate	Silicon	
Insulator	Si_3N_4	80 ± 8
Structural Material	Polysilicon	500 ± 10
Cavity	Vacuum	500 ± 5
Sensing Material	PIB	200 ± 10

6.2 Wafer Fusion Bonding Fabrication Steps for CMUT-Based Gas Sensor

Based on the review conducted in Chapter 3, following steps for CMUT-based gas sensor fabrication are proposed employing wafer fusion bonding process. This technique has capability to fabricate a wide range of cell dimension while providing uniformity, precision and simple fabrication steps [81]. In wafer fusion bonding technique, since cavity is patterned on a separate wafer, there is no need to create releasing holes on the membrane as surface micromachining process. Therefore, efficiency of the device increases due to the vacuum sealed cavity between the membrane and bottom electrode [81]. In this section, fabrication steps for a CMUT-based gas sensor are provided in details, using wafer fusion bonding and inkjet dispensing. All materials, fabrication techniques including etching, lithography and deposition processes as well as temperature of steps are presented. In addition, acceptable tolerance and device dimensions are shown in Table 6.1.

In this work, a highly doped silicon wafer is used as the bottom electrode [109]. Polysilicon on insulator (Poly SOI) wafer is used to create the top membrane. To start fabrication process, silicon wafer is cleaned by piranha solution, as shown in Figure 6.2 (a) [110]. A $2\ \mu\text{m}$ silicon dioxide layer is thermally grown by wet oxidation on the wafer in temperature 1050°C , as illustrated in Figure 6.2 (b). To pattern silicon dioxide, a positive photoresist is

spin coated to create $0.8\mu\text{m}$ thickness of photoresist, which is followed by soft baking to evaporate extra solvent of the photoresist, as shown in Figure 6.2 (c). To expose the photoresist to UV light, proper masks are used to create desirable pattern on silicon dioxide when molecule bonds of positive photoresist break and restructure, as illustrated in Figure 6.2 (d) [70]. To remove the restructured photoresist molecules, as shown in Figure 6.2 (e), a proper developer is used that is provided with the photoresist by the manufacturers. Since plasma etching does not have a good selectivity between silicon and silicon dioxide, a combination of plasma etching and wet etching are used. 80% of silicon dioxide is removed by plasma etching and the rest 20% is wet etched by 20:1 buffered oxide etch (BOE), as it is shown in Figure 6.2 (f) [109]. This combination of etching silicon dioxide provides surface smoothness, which is crucial for wafer bonding [109]. In Figure 6.2 (g), it is shown that another layer of silicon dioxide with $2\mu\text{m}$ thickness is grown on the previous layer, by wet oxidation in 1050°C . As shown in Figure 6.2 (h), by using BOE 6:1, all the grown silicon dioxide is removed while anchors and bottom electrodes are patterned. In Figure 6.2 (i, j), it is shown that 40nm of silicon dioxide is grown in temperature 1000°C using dry oxidation on the silicon wafer, which is followed by depositing 80nm of silicon nitride (Si_3N_4) using LPCVD method. Si_3N_4 is deposited to insulate the bottom electrode. SiO_2 is grown under Si_3N_4 to protect the wafer smoothness underneath against plasma etching while patterning Si_3N_4 . In addition, it acts as an etch stop layer while Si_3N_4 is being removed. As shown in Figure 6.2 (k), a positive photoresist is spin coated on the oxide-nitride, which is followed by a soft bake step to evaporate off extra solvent [70]. Employing proper mask and lithography process make the exposed photoresist soluble in the developer to pattern the photoresist, as shown in Figure 6.2 (l, m). By plasma etching, Si_3N_4 in the wells is removed, as shown in Figure 6.2 (n), while it remains on the plateau areas to insulate the bottom electrode. Extra photoresist is removed by acetone after patterning Si_3N_4 . SiO_2 layer is lithographically patterned by using a positive photoresist.

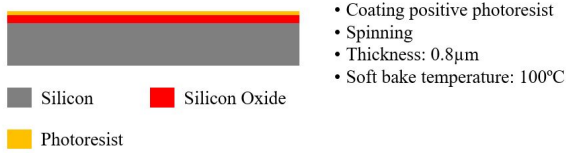
This step is followed by developing photoresist and wet etching SiO_2 using BOE 20:1, as shown in Figure 6.2 (o, p, q). By employing wet oxidation, $700nm$ SiO_2 layer is grown in temperature $1050^\circ C$ to create the anchors, as illustrated in Figure 6.2 (r) [109]. These raised areas act as self-alignments when the Poly SOI wafer is being bonded to the wafer. In order to have a uniform surface for the anchors, a polishing process is used. As can be seen in Figure 6.2 (s), Poly SOI wafer which contains a $500nm$ highly doped polysilicon layer, is bonded to the bottom wafer in a vacuum chamber [24]. To make the molecule bonds stronger between the Poly SOI wafer and the substrate which contains the cavity, an annealing process is needed in nitrogen (N_2) at $1050^\circ C$ [109]. In the next step, the top membrane is released by using Tetramethyl ammonium Hydroxide (TMAH) and 6:1 BOE to remove handle wafer and BOX layer, as illustrated in Figure 6.2 (t) [109]. It is shown in Figure 6.2 (u) that device is functionalized by PIB on the top membrane using inkjet printing [42]. In order to coat the top membrane with PIB, droplets of the sensing material are diluted and ejected on top of the device by inkjet dispensing system [42].



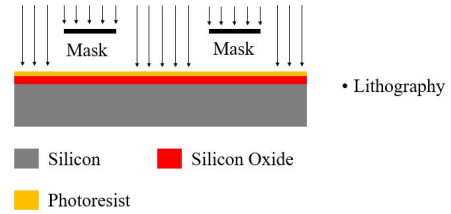
(a)



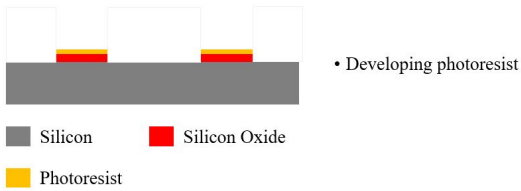
(b)



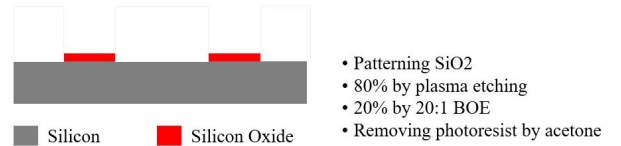
(c)



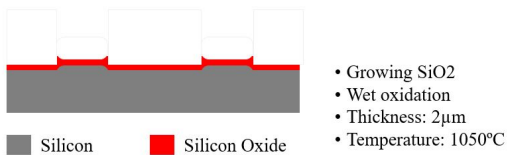
(d)



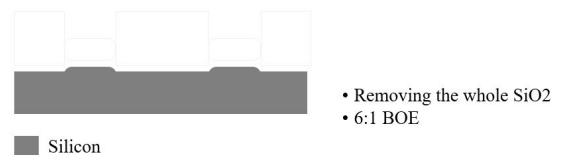
(e)



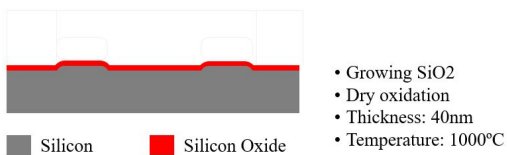
(f)



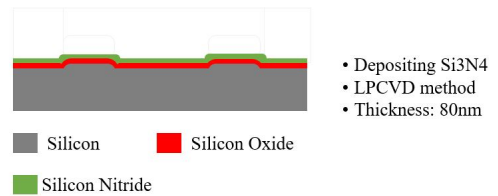
(g)



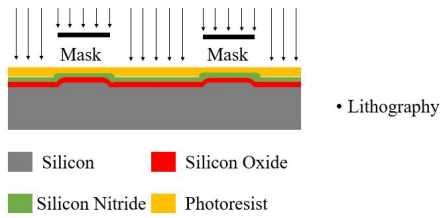
(h)



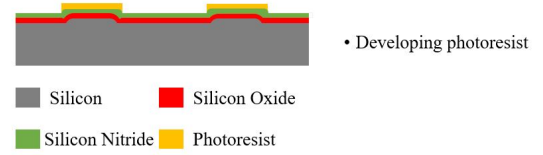
(i)



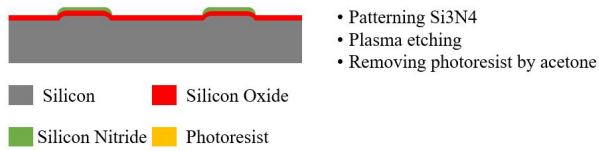
(j)



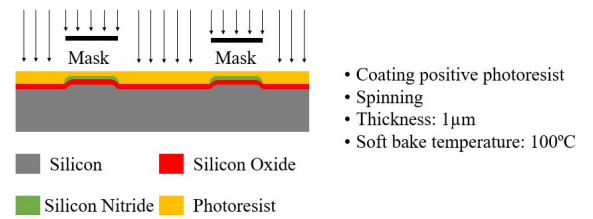
(k)



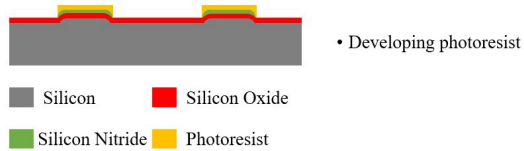
(l)



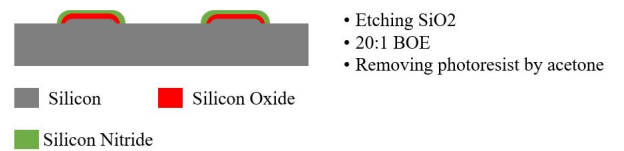
(m)



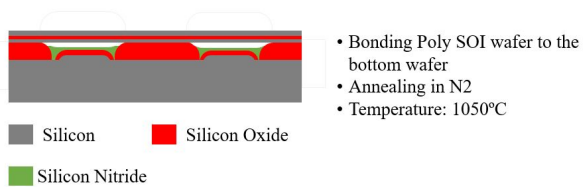
(n)



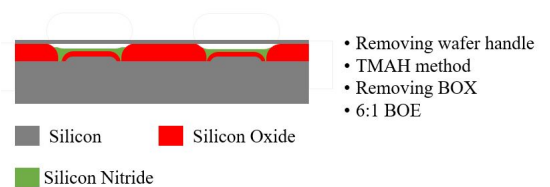
(o)



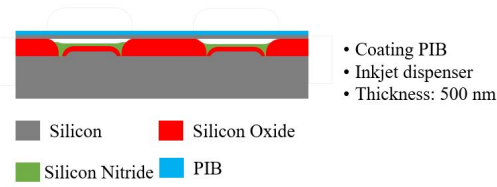
(p)



(q)



(r)



(s)

Figure 6.2: Schematic view of CMUT-based gas sensor fabrication steps using wafer fusion bonding and inkjet dispensing.

6.3 Conclusions

In this chapter, wafer fusion bonding is suggested to fabricate the proposed CMUT-based gas sensor in Chapter 5. This technique is used unlike the conventional process, sacrificial technique, since it has more controllable fabrication steps, which are necessary for a CMUT-based gas sensor to have a thin membrane. In addition, this technique does not create sacrificial holes on top membrane to release the membrane and create the cavity. This feature is important in CMUT-based gas sensor since gas molecules do not reach the cavity and affect sensor's performance. Moreover, existence of the sacrificial channels can damp operation of the device, since sensing polymer may reach the bottom electrode during coating step. Consequently, details of wafer fusion bonding technique to fabricate a CMUT-based gas sensor including lithography, LPCVD, wet and dry oxidations, plasma etching as well as inkjet dispensing are shown in this chapter. Fabrication steps are proposed for the CMUT- based gas sensor with $222Hz/zg$ sensitivity as discussed in Chapter 5. The proposed device has a $500nm$ polysilicon membrane, which is functionalized by $200nm$ PIB while the radius and cavity are $9\mu m$ and $500nm$, respectively. This proposed fabrication step can be utilized as a platform to develop optimized CMUT gas sensors in future. The process remains applicable for CMUT-base sensors utilizing any other sensing materials as well as operating at any desired given frequencies.

Chapter 7: Conclusions and Future Work

Micro and nano gas sensors have a wide range of applications in various fields. They are applicable in biomedical field, industrial manufacturing, air quality monitoring, environmental science, military and automotive industries. Benefiting from advanced micro and nano fabrication technology has led gas sensing advances to be miniaturized and implementable in wearable electronics and portable devices. Capacitive micromachined ultrasonic transducer (CMUT) is one of the configurations that is recently employed in gas sensing technology unlike its conventional approach as a transducer. This configuration has gained attraction due to its high sensitivity and quality factor, low LOD and relatively simple structure and vast range of applications while using MEMS platform. This structure can also benefit from low cost of fabrication due to its relatively simple structure. In a typical CMUT-based gas sensor, conventional CMUT is functionalized by a sensing material related to the target gas or volatile organic compound (VOC). These sensors can detect a wide range of gases while being selective in a complex environment when they are functionalized by various polymers. In order to design a CMUT-based gas sensor, there are different critical design parameters which need to be considered including radius, membrane thickness, residual stress and material properties of the membrane. In addition, influencing parameters of the sensing material on center resonant frequency of sensor including thickness and material properties, should be taken into consideration. Therefore, the objective of this thesis is proposing a comprehensive analytical model for a CMUT-based gas sensor, for the first time, which comprises all the critical design parameters. In addition, FEA simulations are conducted to enhance the sensitivity of device for low gas concentration while being compared with the analytical model.

7.1 Conclusions

In this thesis and for the first time, a new comprehensive analytical model is developed for a circular bilayer CMUT-based gas sensor. The proposed model includes all the critical design parameters of a CMUT-based gas sensor such as radius, thickness and material properties of membrane as well as effective cavity height. The proposed model also includes sensing material's mass, thickness and its material properties. In addition, membrane softening effect due to the applied DC bias voltage as well as residual stress of the membrane and sensing layer are considered in the proposed analytical model. FEA simulations are further conducted using COMSOL Multiphysics to enhance sensor sensitivity for low gas concentration detection for a frequency range between $5MHz$ and $25MHz$ as a sample of the frequency range.

The simulation results for radius of membrane shows that smaller radii contribute in higher frequency, frequency shift and consequently sensor's sensitivity. However, thicker membranes have higher frequency and frequency shift while provide a less sensitive CMUT-based gas sensor. Based on the conducted FEA simulations, silicon nitride membrane has higher frequency and frequency shift whilst polysilicon membrane contributes in a more sensitive device due to its lower density.

In addition, when sensing material exposes to a target gas it adsorbs the target gas molecules, which can increase mass and thickness of the sensing layer. Consequently, in this thesis, FEA simulations are also done to investigate effects of mass and thickness of the sensing material on center resonant frequency of the sensor. Results show that frequency shift of the sensor increases when the sensing material's mass and thickness are raised. Therefore, these two parameters do not neutralize each other and instead they enhance their effects on center resonant frequency of the sensor.

Based on the conducted FEA simulations in this thesis, a CMUT sensor is designed

where its maximum achieved sensitivity is shown to be $222 \text{ Hz}/z\text{g}$. This designed sensor uses a polysilicon membrane with radius and thickness of $9\mu\text{m}$ and 500nm , respectively. The sensor is then functionalized by 300nm PIB. The device is biased with 30V DC while the initial cavity height is 500nm . The frequency range in this thesis is selected between 5MHz and 25MHz as a sample. In addition, achieved results of the proposed analytical model are compared with the conducted FEA simulations. Calculated average variation based on the comparison shows less than 3% for the radius, less than 1% when membrane thickness and cavity height are evaluated and 5% for structural material, respectively. Frequency versus sensing material's mass and thickness also show less than 1% average variation.

7.2 Future Works

The proposed comprehensive analytical model in this thesis, is the first analytical model for a bilayer CMUT-based gas sensor with circular geometry. The CMUT-based gas sensors can be optimized using the developed model in this work for any gas sensing application with a target sensitivity and operating at a desired frequency. The sensor can be further fabricated using the proposed fabrication techniques in this work that uses wafer fusion bonding and inkjet dispensing, to conduct measurements in addition to comparison with the proposed analytical model and FEA simulations in this thesis. The proposed CMUT-sensor can be functionalized with different sensing materials to evaluate selectivity of the device in a complex environment.

References

- [1] C. Statistics, “Canadian cancer statistics 2017,” *Available at: cancer.ca/Canadian-CancerStatistics-2017-EN.pdf (Accessed December 9,2019).*
- [2] Z. Jia, H. Zhang, C. N. Ong, A. Patra, Y. Lu, C. T. Lim, and T. Venkatesan, “Detection of lung cancer: concomitant volatile organic compounds and metabolomic profiling of six cancer cell lines of different histological origins,” *ACS omega*, vol. 3, no. 5, pp. 5131–5140, 2018.
- [3] Y. Saalberg and M. Wolff, “Voc breath biomarkers in lung cancer,” *Clinica Chimica Acta*, vol. 459, pp. 5–9, 2016.
- [4] M. M. Teymoori and H. Asadollahi, “Mems based medical microsensors,” in *2009 Second International Conference on Computer and Electrical Engineering*, vol. 1. IEEE, 2009, pp. 158–162.
- [5] H. Liu, L. Zhang, K. H. H. Li, and O. K. Tan, “Microhotplates for metal oxide semiconductor gas sensor applications—towards the cmos-mems monolithic approach,” *Micromachines*, vol. 9, no. 11, p. 557, 2018.
- [6] S. E. Moon, N.-J. Choi, H.-K. Lee, J. Lee, and W. S. Yang, “Semiconductor-type mems gas sensor for real-time environmental monitoring applications,” *Etri Journal*, vol. 35, no. 4, pp. 617–624, 2013.
- [7] M. Blaschke, T. Tille, P. Robertson, S. Mair, U. Weimar, and H. Ulmer, “Mems gas-sensor array for monitoring the perceived car-cabin air quality,” *IEEE Sensors Journal*, vol. 6, no. 5, pp. 1298–1308, 2006.

- [8] H. Nazemi, A. Joseph, J. Park, and A. Emadi, “Advanced micro-and nano-gas sensor technology: A review,” *Sensors*, vol. 19, no. 6, p. 1285, 2019.
- [9] S. Fanget, S. Hentz, P. Puget, J. Arcamone, M. Matheron, E. Colinet, P. Andreucci, L. Duraffourg, E. Myers, and M. Roukes, “Gas sensors based on gravimetric detection—a review,” *Sensors and Actuators B: Chemical*, vol. 160, no. 1, pp. 804–821, 2011.
- [10] H. J. Lee, K. K. Park, M. Kupnik, N. A. Melosh, and B. T. Khuri-Yakub, “Mesoporous thin-film on highly-sensitive resonant chemical sensor for relative humidity and co₂ detection,” *Analytical chemistry*, vol. 84, no. 7, pp. 3063–3066, 2012.
- [11] B. W. Drinkwater and P. D. Wilcox, “Ultrasonic arrays for non-destructive evaluation: A review,” *NDT & e International*, vol. 39, no. 7, pp. 525–541, 2006.
- [12] M. I. Haller and B. T. Khuri-Yakub, “A surface micromachined electrostatic ultrasonic air transducer,” *IEEE transactions on ultrasonics, ferroelectrics, and frequency control*, vol. 43, no. 1, pp. 1–6, 1996.
- [13] J. Qu, Y. Chai, and S. Yang, “A real-time de-noising algorithm for e-noses in a wireless sensor network,” *Sensors*, vol. 9, no. 2, pp. 895–908, 2009.
- [14] T. F. Refaat, S. Ismail, G. J. Koch, M. Rubio, T. L. Mack, A. Notari, J. E. Collins, J. Lewis, R. De Young, Y. Choi *et al.*, “Backscatter 2 μ m lidar validation for atmospheric co₂ differential absorption lidar applications,” *IEEE Transactions on Geoscience and Remote Sensing*, vol. 49, no. 1, pp. 572–580, 2010.
- [15] A. Mujahid and F. L. Dickert, “Surface acoustic wave (saw) for chemical sensing applications of recognition layers,” *Sensors*, vol. 17, no. 12, p. 2716, 2017.

- [16] S. J. Martin, G. C. Frye, and S. D. Senturia, "Dynamics and response of polymer-coated surface acoustic wave devices: effect of viscoelastic properties and film resonance," *Analytical Chemistry*, vol. 66, no. 14, pp. 2201–2219, 1994.
- [17] P. Kakoty and M. Bhuyan, "Fabrication of micromachined SnO_2 based mos gas sensor with inbuilt microheater for detection of methanol," *Sens. Transducers*, vol. 204, pp. 58–67, 2016.
- [18] J. Jung, W. Lee, W. Kang, E. Shin, J. Ryu, and H. Choi, "Review of piezoelectric micromachined ultrasonic transducers and their applications," *Journal of Micromechanics and Microengineering*, vol. 27, no. 11, p. 113001, 2017.
- [19] M. Urbańczyk and T. Pustelny, "The application of surface acoustic waves in surface semiconductor investigations and gas sensors," in *Modeling and Measurement Methods for Acoustic Waves and for Acoustic Microdevices*. IntechOpen, 2013.
- [20] M. Donarelli and L. Ottaviano, "2d materials for gas sensing applications: A review on graphene oxide, MoS_2 , WS_2 and phosphorene," *Sensors*, vol. 18, no. 11, p. 3638, 2018.
- [21] C. Wang, L. Yin, L. Zhang, D. Xiang, and R. Gao, "Metal oxide gas sensors: sensitivity and influencing factors," *Sensors*, vol. 10, no. 3, pp. 2088–2106, 2010.
- [22] G. F. Fine, L. M. Cavanagh, A. Afonja, and R. Binions, "Metal oxide semi-conductor gas sensors in environmental monitoring," *sensors*, vol. 10, no. 6, pp. 5469–5502, 2010.
- [23] P. Shankar and J. B. B. Rayappan, "Gas sensing mechanism of metal oxides: The role of ambient atmosphere, type of semiconductor and gases-a review," *Sci. Lett. J*, vol. 4, no. 4, p. 126, 2015.

- [24] A. Dey, "Semiconductor metal oxide gas sensors: A review," *Materials Science and Engineering: B*, vol. 229, pp. 206–217, 2018.
- [25] H.-J. Kim and J.-H. Lee, "Highly sensitive and selective gas sensors using p-type oxide semiconductors: Overview," *Sensors and Actuators B: Chemical*, vol. 192, pp. 607–627, 2014.
- [26] V. Bochenkov and G. Sergeev, "Preparation and chemiresistive properties of nanostructured materials," *Advances in colloid and interface science*, vol. 116, no. 1-3, pp. 245–254, 2005.
- [27] X. Zhou, X. Cheng, Y. Zhu, A. A. Elzatahry, A. Alghamdi, Y. Deng, and D. Zhao, "Ordered porous metal oxide semiconductors for gas sensing," *Chinese Chemical Letters*, vol. 29, no. 3, pp. 405–416, 2018.
- [28] A. S. Ergun, X. Zhuang, Y. Huang, O. Oralkan, G. G. Yaralioglu, and B. T. Khuri-Yakub, "Capacitive micromachined ultrasonic transducer technology for medical ultrasound imaging," in *Medical Imaging 2005: Ultrasonic Imaging and Signal Processing*, vol. 5750. International Society for Optics and Photonics, 2005, pp. 58–68.
- [29] A. P. Lee and B. J. Reedy, "Temperature modulation in semiconductor gas sensing," *Sensors and Actuators B: Chemical*, vol. 60, no. 1, pp. 35–42, 1999.
- [30] G. Sauerbrey, "Use of quartz vibrator for weighting thin films on a microbalance," *Zeitschrift fur Physik*, vol. 155, pp. 206–212, 1959.
- [31] S. Arshad, M. M. Salleh, and M. Yahaya, "Quartz crystal microbalance gas sensor for detection of volatile organic compounds using titanium dioxide coated with dye-porphyrin," *Solid State Science and Technology*, vol. 16, no. 1, pp. 75–84, 2008.

- [32] D. Ballantine Jr, R. M. White, S. J. Martin, A. J. Ricco, E. Zellers, G. Frye, and H. Wohltjen, *Acoustic wave sensors: theory, design and physico-chemical applications*. Elsevier, 1996.
- [33] Y.-T. Hsueh, R. Smith, and M. Northrup, “A microfabricated, electrochemiluminescence cell for the detection of amplified dna,” *Sensors and Actuators B: Chemical*, vol. 33, no. 1-3, pp. 110–114, 1996.
- [34] F. Temel and M. Tabakci, “Calix [4] arene coated qcm sensors for detection of voc emissions: Methylene chloride sensing studies,” *Talanta*, vol. 153, pp. 221–227, 2016.
- [35] M. R. Eslami and N. Alizadeh, “Ultrasensitive and selective qcm sensor for detection of trace amounts of nitroexplosive vapors in ambient air based on polypyrrole—bromophenol blue nanostructure,” *Sensors and Actuators B: Chemical*, vol. 278, pp. 55–63, 2019.
- [36] A. G. MacDiarmid, ““synthetic metals”: A novel role for organic polymers (nobel lecture),” *Angewandte Chemie International Edition*, vol. 40, no. 14, pp. 2581–2590, 2001.
- [37] A. Logan and J. T. Yeow, “Fabricating capacitive micromachined ultrasonic transducers with a novel silicon-nitride-based wafer bonding process,” *IEEE transactions on ultrasonics, ferroelectrics, and frequency control*, vol. 56, no. 5, pp. 1074–1084, 2009.
- [38] H. Bai and G. Shi, “Gas sensors based on conducting polymers,” *Sensors*, vol. 7, no. 3, pp. 267–307, 2007.
- [39] X. Liu, S. Cheng, H. Liu, S. Hu, D. Zhang, and H. Ning, “A survey on gas sensing technology,” *Sensors*, vol. 12, no. 7, pp. 9635–9665, 2012.

- [40] T. A. Emadi, C. Shafai, D. J. Thomson, M. S. Freund, N. D. White, and D. S. Jayas, "Polymer-based chemicapacitor sensor for 1-octanol and relative humidity detections at different temperatures and frequencies," *IEEE Sensors Journal*, vol. 13, no. 2, pp. 519–527, 2012.
- [41] A. Ghoorchian and N. Alizadeh, "Chemiresistor gas sensor based on sulfonated dyedoped modified conducting polypyrrole film for high sensitive detection of 2, 4, 6-trinitrotoluene in air," *Sensors and Actuators B: Chemical*, vol. 255, pp. 826–835, 2018.
- [42] K. K. Park, H. J. Lee, M. Kupnik, O. Oralkan, and B. T. Khuri-Yakub, "Capacitive micromachined ultrasonic transducer as a chemical sensor," in *SENSORS, 2008 IEEE*. IEEE, 2008, pp. 5–8.
- [43] Y. Cui, "A feasibility study of micromachined ultrasonic transducers functionalized for ethanol detection," Master's thesis, University of Waterloo, 2017.
- [44] C. Sun, Q. Shi, M. Yazici, C. Lee, and Y. Liu, "Development of a highly sensitive humidity sensor based on a piezoelectric micromachined ultrasonic transducer array functionalized with graphene oxide thin film," *Sensors*, vol. 18, no. 12, p. 4352, 2018.
- [45] B. W. Drinkwater and P. D. Wilcox, "Ultrasonic arrays for non-destructive evaluation: A review," *NDT & e International*, vol. 39, no. 7, pp. 525–541, 2006.
- [46] C.-B. Eom and S. Trolier-McKinstry, "Thin-film piezoelectric mems," *Mrs Bulletin*, vol. 37, no. 11, pp. 1007–1017, 2012.
- [47] G. Perçin, A. Atalar, F. Levent Degertekin, and B. T. Khuri-Yakub, "Micromachined two-dimensional array piezoelectrically actuated transducers," *Applied physics letters*, vol. 72, no. 11, pp. 1397–1399, 1998.

- [48] L. Filipovic and A. Lahlalia, "System-on-chip smo gas sensor integration in advanced cmos technology," *Journal of The Electrochemical Society*, vol. 165, no. 16, pp. B862–B879, 2018.
- [49] N. Watanabe, T. Miyazaki, M. Aoyagi, and K. Yoshikawa, "Silicon wafer thinning and backside via exposure by wet etching," in *2012 IEEE 14th Electronics Packaging Technology Conference (EPTC)*. IEEE, 2012, pp. 355–359.
- [50] J. Baborowski, N. Ledermann, and P. Muralt, "Piezoelectric micromachined transducers (pmut's) based on pzt thin films," in *2002 IEEE Ultrasonics Symposium, 2002. Proceedings.*, vol. 2. Ieee, 2002, pp. 1051–1054.
- [51] S. Tadigadapa and K. Mateti, "Piezoelectric mems sensors: state-of-the-art and perspectives," *Measurement Science and technology*, vol. 20, no. 9, p. 092001, 2009.
- [52] M. S. Salim, M. A. Malek, R. Heng, K. Juni, and N. Sabri, "Capacitive micromachined ultrasonic transducers: Technology and application," *Journal of Medical Ultrasound*, vol. 20, no. 1, pp. 8–31, 2012.
- [53] H. Lee, K. K. Park, M. Kupnik, Ö. Oralkan, and B. Khuri-Yakub, "Highly sensitive detection of dmmp using a cmut-based chemical sensor," in *SENSORS, 2010 IEEE*. IEEE, 2010, pp. 2122–2126.
- [54] K. K. Park, H. Lee, M. Kupnik, and B. T. Khuri-Yakub, "Fabrication of capacitive micromachined ultrasonic transducers via local oxidation and direct wafer bonding," *Journal of microelectromechanical Systems*, vol. 20, no. 1, pp. 95–103, 2011.
- [55] A. S. Logan, L. L. Wong, and J. T. Yeow, "A 1-d capacitive micromachined ultrasonic transducer imaging array fabricated with a silicon-nitride-based fusion process," *IEEE/ASME Transactions on Mechatronics*, vol. 16, no. 5, pp. 861–865, 2011.

- [56] T. A. Emadi and D. A. Buchanan, "Capacitive micromachined ultrasonic transducer with multiple deflectable membranes," 2014.
- [57] C. D. Gerardo, E. Cretu, and R. Rohling, "Fabrication and testing of polymer-based capacitive micromachined ultrasound transducers for medical imaging," *Microsystems & nanoengineering*, vol. 4, no. 1, p. 19, 2018.
- [58] H. J. Lee, K. K. Park, M. Kupnik, and B. T. Khuri-Yakub, "Functionalization layers for co₂ sensing using capacitive micromachined ultrasonic transducers," *Sensors and Actuators B: Chemical*, vol. 174, pp. 87–93, 2012.
- [59] H. J. Lee, K. K. Park, M. Kupnik, O. Oralkan, and B. T. Khuri-Yakub, "Chemical vapor detection using a capacitive micromachined ultrasonic transducer," *Analytical chemistry*, vol. 83, no. 24, pp. 9314–9320, 2011.
- [60] H. Lee, K. K. Park, M. Kupnik, Ö. Oralkan, and B. Khuri-Yakub, "Highly sensitive detection of dmmp using a cmut-based chemical sensor," in *SENSORS, 2010 IEEE*. IEEE, 2010, pp. 2122–2126.
- [61] K. Brenner, A. S. Ergun, K. Firouzi, M. F. Rasmussen, Q. Stedman, and B. P. Khuri-Yakub, "Advances in capacitive micromachined ultrasonic transducers," *Micromachines*, vol. 10, no. 2, p. 152, 2019.
- [62] G. G. Yaralioglu, B. Bayram, A. Nikoozadeh, and B. T. Khuri-Yakub, "Finite element modeling of capacitive micromachined ultrasonic transducers," in *Medical Imaging 2005: Ultrasonic Imaging and Signal Processing*, vol. 5750. International Society for Optics and Photonics, 2005, pp. 77–86.
- [63] I. Yoon, G. Eom, S. Lee, B. K. Kim, S. K. Kim, and H. J. Lee, "A capacitive micromachined ultrasonic transducer-based resonant sensor array for portable volatile

- organic compound detection with wireless systems,” *Sensors*, vol. 19, no. 6, p. 1401, 2019.
- [64] A. S. Ergun, G. G. Yaralioglu, and B. T. Khuri-Yakub, “Capacitive micromachined ultrasonic transducers: Theory and technology,” *Journal of aerospace engineering*, vol. 16, no. 2, pp. 76–84, 2003.
- [65] W. You, “Exploring multiple-mode vibrations of capacitive micromachined ultrasonic transducers (cmuts),” Ph.D. dissertation, University of British Columbia, 2013.
- [66] T. A. Emadi and D. A. Buchanan, “Design and fabrication of a novel mems capacitive transducer with multiple moving membrane, m3cmut,” *IEEE Transactions on Electron Devices*, vol. 61, no. 3, pp. 890–896, 2014.
- [67] K. K. Park, H. Lee, M. Kupnik, Ö. Oralkan, J.-P. Ramseyer, H. P. Lang, M. Hegner, C. Gerber, and B. T. Khuri-Yakub, “Capacitive micromachined ultrasonic transducer (cmut) as a chemical sensor for dmmp detection,” *Sensors and Actuators B: Chemical*, vol. 160, no. 1, pp. 1120–1127, 2011.
- [68] D.-C. Pang and C.-M. Chang, “Development of a novel transparent flexible capacitive micromachined ultrasonic transducer,” *Sensors*, vol. 17, no. 6, p. 1443, 2017.
- [69] D. Barauskas, D. Pelenis, G. Vanagas, D. Viržonis, and J. Baltrušaitis, “Methylated poly (ethylene) imine modified capacitive micromachined ultrasonic transducer for measurements of co2 and so2 in their mixtures,” *Sensors*, vol. 19, no. 14, p. 3236, 2019.
- [70] Y. Huang, A. S. Ergun, E. Haeggstrom, M. H. Badi, and B. T. Khuri-Yakub, “Fabricating capacitive micromachined ultrasonic transducers with wafer-bonding technology,” *Journal of microelectromechanical systems*, vol. 12, no. 2, pp. 128–137, 2003.

- [71] H. J. Lee, K. K. Park, O. Oralkan, M. Kupnik, and B. T. Khuri-Yakub, "Cmut as a chemical sensor for dmmp detection," in *2008 IEEE international frequency control symposium*. IEEE, 2008, pp. 434–439.
- [72] H. Nazemi and A. Emadi, "A new advanced analytical model for bi-layer circular cmut-based gas sensors," in *SENSORS, 2019 IEEE*. IEEE, 2019–Accepted.
- [73] J. Wang, S. H. Pun, P. U. Mak, C.-H. Cheng, Y. Yu, P.-I. Mak, and M. I. Vai, "Improved analytical modeling of membrane large deflection with lateral force for the underwater cmut based on von kármán equations," *IEEE Sensors Journal*, vol. 16, no. 17, pp. 6633–6640, 2016.
- [74] H. J. Lee, K. K. Park, M. Kupnik, O. Oralkan, and B. T. Khuri-Yakub, "Chemical vapor detection using a capacitive micromachined ultrasonic transducer," *Analytical chemistry*, vol. 83, no. 24, pp. 9314–9320, 2011.
- [75] X. Jin, I. Ladabaum, F. L. Degertekin, S. Calmes, and B. T. Khuri-Yakub, "Fabrication and characterization of surface micromachined capacitive ultrasonic immersion transducers," *Journal of Microelectromechanical systems*, vol. 8, no. 1, pp. 100–114, 1999.
- [76] K. K. Park, H. Lee, M. Kupnik, O. Oralkan, and B. Khuri-Yakub, "Fabricating capacitive micromachined ultrasonic transducers with direct wafer-bonding and locos technology," in *2008 IEEE 21st International Conference on Micro Electro Mechanical Systems*. IEEE, 2008, pp. 339–342.
- [77] R. B. Roy, A. Bozkurt, O. Farhanieh, and A. S. Ergun, "Embedded sacrificial layers for cmut fabrication," in *2015 IEEE SENSORS*. IEEE, 2015, pp. 1–4.

- [78] C. D. Gerardo, E. Cretu, and R. Rohling, "Fabrication and testing of polymer-based capacitive micromachined ultrasound transducers for medical imaging," *Microsystems and nanoengineering*, vol. 4, no. 1, p. 19, 2018.
- [79] N. Miki and S. Spearing, "Effect of nanoscale surface roughness on the bonding energy of direct-bonded silicon wafers," *Journal of Applied Physics*, vol. 94, no. 10, pp. 6800–6806, 2003.
- [80] M. J. Mølgaard, J. M. Hansen, M. H. Jakobsen, and E. V. Thomsen, "Sensitivity optimization of wafer bonded gravimetric cmut sensors," *Journal of Microelectromechanical Systems*, vol. 27, no. 6, pp. 1089–1096, 2018.
- [81] K. K. Park, H. Lee, M. Kupnik, and B. T. Khuri-Yakub, "Fabrication of capacitive micromachined ultrasonic transducers via local oxidation and direct wafer bonding," *Journal of microelectromechanical Systems*, vol. 20, no. 1, pp. 95–103, 2011.
- [82] W. Y. Choi, Y. S. Kwak, and K. K. Park, "Fingerprint imaging system based on capacitive micromachined ultrasonic transducer by using impediography method including direct touch and waveguide methods," *IEEE transactions on ultrasonics, ferroelectrics, and frequency control*, vol. 66, no. 2, pp. 402–411, 2018.
- [83] F. Y. Yamaner, X. Zhang, and Ö. Oralkan, "Fabrication of anodically bonded capacitive micromachined ultrasonic transducers with vacuum-sealed cavities," in *2014 IEEE International Ultrasonics Symposium*. IEEE, 2014, pp. 604–607.
- [84] M. Bellaredj, G. Bourbon, V. Walter, P. Le Moal, and M. Berthillier, "Anodic bonding using soi wafer for fabrication of capacitive micromachined ultrasonic transducers," *Journal of Micromechanics and Microengineering*, vol. 24, no. 2, p. 025009, 2014.

- [85] X. Zhang, O. Adelegan, F. Y. Yamaner, and O. Oralkan, "Cmuts on glass with its bottom electrodes for improved transparency," in *2016 IEEE International Ultrasonics Symposium (IUS)*. IEEE, 2016, pp. 1–4.
- [86] X. Zhuang, D.-S. Lin, Ö. Oralkan, and B. T. Khuri-Yakub, "Fabrication of flexible transducer arrays with through-wafer electrical interconnects based on trench refilling with pdms," *Journal of Microelectromechanical Systems*, vol. 17, no. 2, pp. 446–452, 2008.
- [87] J. Song, C. Xue, C. He, R. Zhang, L. Mu, J. Cui, J. Miao, Y. Liu, and W. Zhang, "Capacitive micromachined ultrasonic transducers (cmuts) for underwater imaging applications," *Sensors*, vol. 15, no. 9, pp. 23 205–23 217, 2015.
- [88] A. Caronti, G. Caliano, A. Iula, and M. Pappalardo, "An accurate model for capacitive micromachined ultrasonic transducers," *IEEE transactions on ultrasonics, ferroelectrics, and frequency control*, vol. 49, no. 2, pp. 159–168, 2002.
- [89] M. Cai, "A polymumps capacitive micromachined ultrasonic transducer," Ph.D. dissertation, University of British Columbia, 2011.
- [90] I. O. Wygant, M. Kupnik, and B. T. Khuri-Yakub, "Analytically calculating membrane displacement and the equivalent circuit model of a circular cmut cell," in *2008 IEEE Ultrasonics Symposium*. IEEE, 2008, pp. 2111–2114.
- [91] S. Satir, "Modeling and optimization of capacitive micromachined ultrasonic transducers," Ph.D. dissertation, Georgia Institute of Technology, 2014.
- [92] V. Forsmo, "Capacitive micromachined ultrasonic transducers," Master's thesis, 2007.

- [93] I. Ladabaum, X. Jin, H. T. Soh, A. Atalar, and B. Khuri-Yakub, "Surface micromachined capacitive ultrasonic transducers," *IEEE transactions on ultrasonics, ferroelectrics, and frequency control*, vol. 45, no. 3, pp. 678–690, 1998.
- [94] J. W. Hutchinson, "Stresses and failure modes in thin films and multilayers," *Notes for a Dcamm Course. Technical University of Denmark, Lyngby*, vol. 1, 1996.
- [95] T. A. Osswald, "Polymer processing fundamentals. hanser," 1998.
- [96] K. Pister and S. Dong, "Elastic bending of layered plates," *Journal of the Engineering Mechanics Division*, vol. 85, no. 4, pp. 1–10, 1959.
- [97] J. Wang, Y. Yu, S. H. Pun, P. U. Mak, U. K. Che, C.-H. Cheng, and M. I. Vai, "Analytical model with lateral force for conventional cmut membranes under large deflection using von karman equations," in *2016 IEEE International Ultrasonics Symposium (IUS)*. IEEE, 2016, pp. 1–4.
- [98] E. Ventsel, "Krauthammer and t," *Thin plates and shells: theory and analysis and applications*, 2001.
- [99] N. Sharma, M. Hooda, and S. Sharma, "Synthesis and characterization of lpcvd polysilicon and silicon nitride thin films for mems applications," *Journal of Materials*, vol. 2014, 2014.
- [100] I. O. Wygant, M. Kupnik, and B. T. Khuri-Yakub, "An analytical model for capacitive pressure transducers with circular geometry," *Journal of Microelectromechanical Systems*, vol. 27, no. 3, pp. 448–456, 2018.
- [101] A. Lohfink and P.-C. Eccardt, "Linear and nonlinear equivalent circuit modeling of cmuts," *IEEE transactions on ultrasonics, ferroelectrics, and frequency control*, vol. 52, no. 12, pp. 2163–2172, 2005.

- [102] Y.-J. Lee, J.-G. Kim, J.-H. Kim, J. Yun, and W. J. Jang, “Detection of dimethyl methylphosphonate (dmmp) using polyhedral oligomeric silsesquioxane (poss),” *Journal of nanoscience and nanotechnology*, vol. 18, no. 9, pp. 6565–6569, 2018.
- [103] A. K. Johar, R. Patel, C. Periasamy, A. Agarwal, and D. Boolchandani, “Fem modeling and simulation of smfbar sensor with pib as sensing layer for tetrachloroethane (pce) gas detection,” *Materials Research Express*, vol. 6, no. 1, p. 015033, 2018.
- [104] M. T. Ahmadi, R. Ismail, and S. Anwar, *Handbook of Research on Nanoelectronic Sensor Modeling and Applications*. IGI Global, 2016.
- [105] W. Moebs, J. Ling, S, and J. Sanny, *University Physics Volume 1*. OpenStax, 2016.
- [106] J. Hageman, R. J. Meier, M. Heinemann, and R. De Groot, “Young modulus of crystalline polyethylene from ab initio molecular dynamics,” *Macromolecules*, vol. 30, no. 19, pp. 5953–5957, 1997.
- [107] A. Erguri, Y. Huang, X. Zhuang, O. Oralkan, G. G. Yarahoglu, and B. T. Khuri-Yakub, “Capacitive micromachined ultrasonic transducers: Fabrication technology,” *IEEE transactions on ultrasonics, ferroelectrics, and frequency control*, vol. 52, no. 12, pp. 2242–2258, 2005.
- [108] S. Park, I. Yoon, S. Lee, H. Kim, J.-W. Seo, Y. Chung, A. Unger, M. Kupnik, and H. J. Lee, “Cmut-based resonant gas sensor array for voc detection with low operating voltage,” *Sensors and Actuators B: Chemical*, vol. 273, pp. 1556–1563, 2018.
- [109] Z. Li, L. L. Wong, A. I. Chen, S. Na, J. Sun, and J. T. Yeow, “Fabrication of capacitive micromachined ultrasonic transducers based on adhesive wafer bonding technique,” *Journal of Micromechanics and Microengineering*, vol. 26, no. 11, p. 115019, 2016.

[110] K. R. Williams and R. S. Muller, "Etch rates for micromachining processing," *Journal of Microelectromechanical systems*, vol. 5, no. 4, pp. 256–269, 1996.

Appendices

IEEE Permission to Reprint

In reference to IEEE copyrighted material which is used with permission in this thesis, the IEEE does not endorse any of [university/educational entity's name goes here]'s products or services. Internal or personal use of this material is permitted. If interested in

reprinting/republishing IEEE copyrighted material for advertising or promotional purposes or for creating new collective works for resale or redistribution, please go to

[http : //www.ieee.org/publications_standards/publications/rights/rightslink.html](http://www.ieee.org/publications_standards/publications/rights/rightslink.html)

to learn how to obtain a License from RightsLink.

Vita Auctoris

NAME	Haleh Nazemi
PLACE OF BIRTH	Esfahan, Esfahan, Iran
YEAR OF BIRTH	1985
EDUCATION	M.A.Sc. Electrical Engineering University of Windsor, Ontario, Canada 2019 B.Sc. Physics Islamic Azad University, Esfahan, Iran 2009

ACADEMIC EMPLOYMENT

Research Assistant	Jan. 2018 - Dec. 2019
Electrical Micro & Nano Devices, and Sensors Research Centre University of Windsor, Ontario, Canada	
Graduate Teaching Assistant	Jan. 2018 - Dec. 2019
Electrical and Computer Engineering Department University of Windsor, Ontario, Canada	